AN ABSTRACT OF THE THESIS OF

Matthew Chin for the degree of Master of Science in
Electrical and Computer Engineering presented on March 15, 2010.

Title:
Magnetically Programmable Surface Acoustic Wave Devices for RFID Applications

Abstract approved: ______________________________
Pallavi Dhagat

Magnetically programmable surface acoustic wave (MP SAW) devices were designed, fabricated and characterized in this thesis using integrated giant magnetoresistive (GMR) bits with interdigital reflectors. This provides a proof of concept of a novel storage element on radio frequency identification tags. Interdigital transducers (IDTs) on a piezoelectric substrate are used to transmit and receive signals to and from the reflector, where the magnitude of the signal reflected back is dependent on the resistance state of the GMR bit. Two MP SAW device designs were considered and fabricated. Theoretical calculations were performed to determine the impedance of the IDTs and reflector, and to determine what the effects of a varying impedance load on the reflector would have on the reflection response of the MP SAW device. Programmable switching of one GMR bit has been demonstrated using an applied magnetic field strength

of 10 Oe to 15 Oe. Scattering parameter measurements have been taken to determine the magnitude of the reflection response off the reflector, and a difference of 0.9% has been detected between the high and low resistance states of the GMR bit. A change in reflection response has been consistently shown in all MP SAW devices, demonstrating the feasibility of integrated magnetic elements in SAW devices as memory elements in RFID tags.

Magnetically Programmable Surface Acoustic Wave Devices for RFID Applications

by

Matthew Chin

A THESIS

submitted to

Oregon State University

in partial fulfillment of
the requirements for the
degree of

Master of Science

Presented March 15, 2010
Commencement June 2010

Master of Science thesis of Matthew Chin presented on March 15, 2010.

APPROVED:

Major Professor, representing Electrical and Computer Engineering

Director of the School of Electric Engineering and Computer Science

Dean of the Graduate School

I understand that my thesis will become part of the permanent collection of Oregon State University libraries. My signature below authorizes release of my thesis to any reader upon request.

Matthew Chin, Author

ACKNOWLEDGEMENTS

I would like to thank my family for their unwavering support and encouragement throughout my education and life. I would also like to thank and express my sincere appreciation to my mentors who have given me insight and support throughout this entire process. Dr. Pallavi Dhagat has provided both direction and support as an advisor. Dr. Albrecht Jander, Chris Tasker and Dr. Thomas Plant have given me much advice and guidance that have shaped my educational experience. Finally, I cannot thank my colleagues and teammates enough for all of their support and help. Special acknowledgements go to Simon Ghionea, Linda Engelbrecht, Na An, Tim Marr, Ben Buford, Ira Jewell, Weiyang Li, Jonah Gross, and Han Song for being great friends and collaborators in research and in life.

TABLE OF CONTENTS

Page

1 Introduction 1

2 Literature Review 3
- 2.1 Radio Frequency Identification (RFID) 3
  - 2.1.1 Description and Overview 3
  - 2.1.2 Passive RFID Tags 5
  - 2.1.3 Passive RFID Applications 8
- 2.2 Surface Acoustic Wave Devices 9
  - 2.2.1 Surface Acoustic Wave Device Components 10
  - 2.2.2 Surface Acoustic Wave Device Operations 21
- 2.3 Giant Magnetoresistance 24
  - 2.3.1 Giant Magnetoresistance Description 25
  - 2.3.2 Giant Magnetoresistive Film Stack Types 28

3 SAW Device Design 31
- 3.1 Piezoelectric Substrate Selection 31
- 3.2 Interdigital Transducer Design 32
  - 3.2.1 Interdigital Transducer Impedance 34
  - 3.2.2 Interdigital Transducer Modeling 38
  - 3.2.3 Reflector Structures 45
- 3.3 Giant Magnetoresistive Bits 51

4 Fabrication and Measurement Techniques 64
- 4.1 Fabrication Processes 64
  - 4.1.1 Material Deposition Techniques 64
  - 4.1.2 Photolithography Techniques 67
  - 4.1.3 Etching Techniques 69
  - 4.1.4 Lift-Off Techniques 71
- 4.2 SAW Device Process Flows 72
  - 4.2.1 Oregon State University Process Flow 73
  - 4.2.2 US Army Research Laboratories Process Flow 76
- 4.3 Measurement Techniques and Characterization 80
  - 4.3.1 Experimental Setup 80
  - 4.3.2 Measurements 81

TABLE OF CONTENTS (Continued)

Page

5 Results and Discussion 90

5.1 SAW Device Response with respect to Reflector Design 90

5.2 SAW Device Response with respect to Discrete Resistances 96

5.3 MP SAW Device Response as a function of Applied Magnetic Fields 101

5.4 MP SAW Device Response with respect to GMR Bit Orientation . 108

6 Conclusions 112

6.1 Summary 112

6.2 Recommendations for Future Work 115

6.2.1 Improving Reflection Response 115

6.2.2 Adding more Memory Elements 116

6.2.3 Antenna Development 116

Bibliography 117

Appendices 124

A OSU Fabrication Process Details 125

B ARL Fabrication Process Details 129

C LabVIEW Block Diagrams 134

D Network Analyzer Settings 138

LIST OF FIGURES

Figure Page

2.1 A depiction of a passive RFID tag and associated reader is shown. The reader sends out an interrogation signal, which is then read by the tag, and an encoded identification signal is then transmitted back to the reader. 4

2.2 A block diagram of a typical IC-based passive RFID tag is shown. RF signal lines are represented in blue and DC power lines are represented in green. 7

2.3 A surface acoustic wave is shown propagating across a piezoelectric material. Compression waves cause deformation and particle displacement along the x-axis, and shear waves cause deformation and particle displacement along the y-axis. The displacement is limited to roughly one wavelength into the depth of the piezoelectric material. 13

2.4 A depiction of a single-electrode interdigital transducer. The single-electrode design is composed of alternating electrode bars with a thickness, a, of the same dimension as the spacing between alternating electrodes. The mechanical period, p, is the distance between the front edge of one metal electrode to the front edge of the neighboring electrode. The electrical period, d, is the distance between the front edge of an electrode to the front edge of the next electrode at the same potential. The aperture width, L, is the width of the electrode overlap between the two bus bars. Finally, N is the number of electrodes present in the IDT. To get the number of periods, the number of electrodes is divided by the number of electrodes in one electrical period. 16

2.5 Various IDT designs are presented in schematic form: (a) Single-electrode IDT with the charge polarities alternating every electrode. (b) Double-electrode IDT with the charge polarities alternating every other electrode. (c) IDT with apodized electrodes (d) Multi-frequency IDT with varying electrode widths 20

2.6 Depiction of a SAW delay line. 21

2.7 Depiction of a SAW RFID tag. 24

2.8 A multilayer, GMR thin film stack is portrayed, composed of 6 layers. 25

Figure Page

2.9 Giant magnetoresistance equivalent resistor network for the anti-parallel and parallel alignment of magnetic layers. In this example, $R_1 < R_2$ in terms of resistance. The anti-parallel state will have a larger equivalent resistance compared to the parallel state. 27

2.10 Cross-sections of the four different types of GMR films stacks are presented: (a) Magnetic multilayer, (b) spin valve, (c) pseudo-spin valve, and (d) granular thin film. The layers with arrows in the opposite directions represent layers that can their magnetization reoriented in the direction of an applied magnetic field. 28

3.1 The equivalent circuit representation of an interdigital transducer. $Y(f)$ is the admittance of the IDT, $G_a(f)$ represents the radiation conductance, $B_a(f)$ represents the acoustic susceptance, and C_T represents the static capacitance. 34

3.2 Illustration of a SAW generating IDT. An applied voltage is placed across the IDT terminals to generate SAWs between the oppositely polarized electrodes represented by the line sources centered in between the electrodes. The polarity of the electrodes is described by term C_m. The distance between the line sources generating the SAWs is given as p. There are M line sources. 40

3.3 The shape of the frequency response for a single-electrode IDT is dictated by the array factor calculated with equation 3.2.9. Launched SAWs have a frequency response indicated in blue above. For SAWs reflected back, the frequency response at the IDT is the square of the array factor magnitude. 43

3.4 An illustration of a double-electrode IDT is shown. For the surface wave amplitude and frequency response calculations, the D-E IDT can be modeled as two S-E IDTs offset by p/2. The surface wave amplitude as a function of frequency is the summed results of the two S-E IDTs. With this method, the same analysis performed for the S-E IDT can be used to solve for the D-E IDT case. 55

LIST OF FIGURES (Continued)

Figure Page

3.5 The array factor magnitudes for the S-E IDT design (blue) and the D-E IDT design (green) are plotted against frequency normalized to the center frequency (72.67 MHz). The array factor magnitude of the D-E IDT design was calculated by dividing the D-E IDT into two S-E IDTs with a positional offset of $p/2$ and then summing their wave amplitude contributions. The S-E array factor magnitude was multiplied by the D-E window function (red) to achieve the D-E array factor magnitude. 56

3.6 The shape of the frequency response for a double-electrode IDT is dictated by the array factor calculated with equation 3.2.12. Launched SAWs have a frequency response indicated in blue above. The frequency response at the receiving IDT after reflected waves return is the square of the array factor magnitude indicated in red. Note that the frequencies are normalized to the center frequency of the modeled IDT (72.67 MHz). 57

3.7 Illustration of SAW reflections from mechanical and electrical loading on a S-E reflector design and a D-E reflector design. For the S-E reflector, constructive interference of the reflected waves occur due to the 1/2 wavelength spacing of the electrodes. For the D-E reflector, destructive interference of the reflected waves occur due to the 1/4 wavelength spacing of the electrodes. 58

3.8 Illustration of generated SAWs in the direction of the incident waves (reflections) from regenerated waves due to strong electromechanical coupling. The S-E and D-E reflector designs both regenerate waves when there is an infinite impedance across the electrode terminals (open-circuited) due to the potential and subsequent transduction of SAWs generated from the incident surface wave. 59

3.9 Illustration of shorted interdigital reflector structures. Surface waves are not regenerated due to the fact that no potential can be developed between the electrodes. 60

3.10 Equivalent circuit of the IDT impedance with a GMR bit resistive element. The GMR bit acts as a variable resistor load across the terminals of the IDT. 60

LIST OF FIGURES (Continued)

Figure Page

3.11 Schematic representation of the 3-port, P-matrix. Port 1 and port 2 are acoustical ports, and port 3 is the electrical port. The load impedance is placed across the terminals of port 3. The interactions between the ports are described by 9 matrix elements, which are listed in Table 3.6. 61

3.12 Simulated plots of the normalized S_{11} response $((S_{11} - S_{11min})/S_{11min})$ as a function of resistive load across the interdigital reflector. . . . 61

3.13 GMR thin film stack composition used for the development of MP SAW devices in this thesis. 62

3.14 Magneto-Optical Kerr Effect (MOKE) plot characterizing the GMR thin film stack used for developing MP SAW devices. 62

3.15 Percent change of resistance over the minimum resistance $(\Delta R/R_{min})$ with respect to applied magnetic field for the GMR thin film stack used for the development of the MP SAW devices. A 4% change of resistance was observed between the high and low resistance state of the GMR film. 63

3.16 A 10x microscope images show the dimensions and location of an integrated GMR bit between the terminals of an interdigital reflector. 63

4.1 An illustration of the thermal evaporation process is shown in (a), and an illustration of the electron-beam evaporation process is shown in (b). In both cases, a source material (typically with a melting point of less than 1200°C) is heated to the point of evaporation. A substrate is placed some distance above the source and the material condenses on the substrate, depositing a thin film. 66

4.2 Photolithographic patterning of two types of photoresist using UV light source and a contact mask. Positive photoresist and negative photoresist create inverse patterns when the same mask is used. . . 68

4.3 Typical process flow for an etching process. 70

4.4 Typical process flow for lift-off. 72

4.5 Process flow diagram used to fabricated MP SAW devices at Oregon State University. 84

Figure Page

4.6 A fabricated GMR bit aligned between the two terminals of an interdigital reflector on a MP SAW device is shown at 5x magnification on an optical microscope. 85

4.7 Image of two SAW devices on one substrate (reference SAW delay line on top, and an MP SAW device on the bottom) glued into a PCB fixture, with the terminals of the IDTs wirebonded to SMA connectors. 85

4.8 (a) GMR bit on a single-electrode MP SAW device fabricated with the ARL process (5x magnification). (b) GMR bit on a double-electrode MP SAW device fabricated owiththe ARL process (5x magnification). 86

4.9 Illustration of the process flow used to fabricate MP SAW devices at the U.S. Army Research Laboratories. * GMR Film Deposition was performed by sputter deposition at the National Institute of Standards and Technology, Boulder, CO. 87

4.10 An example of an ARL-fabricated MP SAW device that has been wirebonded into a dual-inline package. 88

4.11 Block diagram of the experimental setup used to measure reflection S-parameters. The setup allows a varying magnetic field to be affected across the MP SAW device under test, and the entire system is controlled via a LabVIEW program on a GPIB-connected computer system. The field is controlled by changing the current in the solenoid. 88

4.12 Graphical user interface for the LabVIEW program that automates measurements. 89

5.1 Illustrations of the four reflector device designs are shown, including (a) a single-electrode open reflector, (b) a single-electrode shorted reflector (c) a double-electrode open reflector, and (d) a double-electrode shorted reflector. The reflector structure is centered between two IDTs, allowing for both reflection and transmission measurements to be taken. 91

Figure Page

5.2 The S_{11} linear magnitude is plotted over a 7 MHz frequency range around the calculated center frequency of all measured devices. . . 95

5.3 Illustration of SAW device configurations used in this set of experiments. (a) represents an open single-electrode reflector SAW device with a potentiometer between the terminals of the interdigital reflector. (b) represents the double-electrode equivalent to (a). The network analyzer port definitions are provided as well. 97

5.4 Images of the fixture used to take S-parameter measurements with a potentiometer between the reflector terminals. The reflector terminals were wirebonded to package pins, which could be accessed through the use of a DIP socket. The left picture presents the topside of the fixture while the picture on the right shows the backside of the fixture. 99

5.5 The S_{11} linear magnitude was taken at the center frequency for 21 resistances using a potentiometer. The plot normalizes the S_{11} linear magnitude to the center frequency response at 50Ω. Measurements were taken on a single-electrode SAW device (Device 24 SE) and a double-electrode SAW device (Device 35 DE). 100

5.6 Illustration of SAW device configurations used in this set of experiments. (a) represents a single-electrode MP SAW device with an integrated GMR bit between the terminals of the interdigital reflector. (b) represents the double-electrode equivalent to (a). 102

5.7 $\Delta S_{11}/S_{11}min$ as a function of applied magnetic field for a 8 MP SAW devices and 2 control SAW devices (open reflector SAW devices without GMR bits). 5 S-E and 3 D-E MP SAW devices were measured along with 1 S-E and 1 D-E control device used to confirm that the resistance change of the GMR bits was causing the change in signal response. 105

5.8 Illustration of the two magnetic field orientations applied to the two SAW devices. (a) shows the applied magnetic field parallel to the easy axis of the GMR bit while (b) shows the applied magnetic field perpendicular to the easy axis (parallel to the hard axis of the GMR bit). A S-E MP SAW device and a D-E MP SAW device were measured in this experiment. 109

LIST OF FIGURES (Continued)

Figure Page

5.9 Plot of the normalized S_{11} response ($\Delta S_{11}/S_{11}min$) as a function of applied magnetic field when the MP SAW devices are oriented in the applied magnetic field parallel to the easy axis and parallel to the hard axis of the GMR bit. 2 MP SAW devices (DEV24, S-E and DEV35, D-E) were measured. 111

LIST OF TABLES

Table | Page

2.1 Common piezoelectric substrate materials and their properties, including SAW velocity (v_{saw}), electro-mechanical coupling coefficient (K^2), SAW propagation temperature coefficient of delay (TCD), relative velocity change ($\frac{\Delta v}{v}$), and relative dielectric permittivity constant ($\frac{\varepsilon_p}{\varepsilon_0}$) where ε_0 is the permittivity of free space and ε_p is the permittivity of the material. 15

3.1 Table of definitions for variables associated with the radiation conductance, reactive admittance, and static capacitance as described by Engan [1]. 36

3.2 List of material properties for Y-Z lithium niobate that are important for calculating the resonant frequency and impedance of an IDT fabricated on top of the piezoelectric substrate. 37

3.3 List of independent design parameters for the four IDT designs: (OSU SE) = OSU-fabricated single-electrode design, (OSU DE) = OSU-fabricated double-electrode design, (ARL SE) = ARL-fabricated single-electrode design, and (ARL DE) = ARL-fabricated double-electrode design. A physical representation associated with each of the listed parameters can be found in Figure 2.4. 38

3.4 List of design dependent parameters used for the impedance calculations. Values are dependent on the electrode polarity configuration. * S-E = single-electrode design, D-E = double-electrode design . . . 38

3.5 Calculated properties of the four IDT designs: (OSU SE) = OSU-fabricated single-electrode design, (OSU DE) = OSU-fabricated double-electrode design, (ARL SE) = ARL-fabricated single-electrode design, and (ARL DE) = ARL-fabricated double-electrode design. . . 39

3.6 Description of the 9 matrix elements associated with the P-matrix that fully describes an interdigital transducer. *The acoustic scattering parameters are defined for the short-circuited IDT (no voltage drop across port 3). 49

5.1 Network analyzer settings used for measuring the devices illustrated in Figure 5.1. Screen captures and the locations of these settings on the Agilent E5071C network analyzer can be found in Appendix D. 92

LIST OF TABLES (Continued)

Table Page

5.2 Device measurements including the measured center frequency of each device, and the S_{11} magnitude at the center frequency. * Design Legend: SE Open = Single-Electrode Open Reflector Device; SE Short = Single-Electrode Shorted Reflector Device; DE Open = Double-Electrode Open Reflector Device; DE Short = Double-Electrode Shorted Reflector Device 93

5.3 Averaged center frequency and S_{11} magnitude data for each of the four reflector designs. Data was averaged for devices with the same design at each data point collected along the frequency range detailed in Table 5.1. It should be noted that f_c variation and S_{11} variation refers to the difference between the highest and lowest values in the sample set. * Refer to Table 5.2 for the Design Legend. 94

5.4 Measured GMR resistance results from 3 single-electrode MP SAW devices. Additional wirebonds were added to provide access to the GMR bits. The calculated resistances of the GMR bit based on the measurement data provided by the GMR thin film stack manufacturer (NIST) is also provided. Contact pad and wirebond resistances could potentially account for the differences along with variations in fabrication. 98

5.5 Linear and logarithmic curve fitting was performed on the results from Device 24 (S-E) and Device 35 (D-E). The equations of those lines of best fit are presented along with the equations associated with the simulations performed for the S-E and D-E reflector SAW devices. 101

5.6 Network analyzer settings and magnetic field settings for MP SAW device and control SAW device measurements. 104

LIST OF TABLES (Continued)

Table Page

5.7 Compiled results from MP SAW device measurements, which includes % S_{11} change($\Delta S_{11}/S_{11}min$) normalized to the relative minimum response for the device being measured, the midpoints of the applied magnetic field strength range required to switch the resistance state of the GMR bit (first value for first sweep (+ → -), and second value for return sweep (- → +)), and hysteresis range about the midpoints of the magnetic field strength required to flip the GMR bit. * Design Legend: SE GMR = Single-Electrode MP SAW Device; DE GMR = Double-Electrode MP SAW Device; SE Open = Single-Electrode Open Reflector Device; DE Open = Double-Electrode Open Reflector Device 106

5.8 The averages, standard deviations, and variation range are provided for the % S_{11} change, midpoints of the required switching field strength for the (1) [+ to -] and (2) [- to +] field sweeps (i.e. the field strength value that is required to change the GMR bit resistance to halfway in between the low and high resistance state), and the hysteresis of the S-E and D-E GMR MP SAW devices. Variation refers to the difference between the highest and lowest values in the sample set. * Refer to Table 5.7 for the Design Legend. . . . 107

5.9 Network analyzer settings and magnetic field settings for MP SAW device measurements with varying GMR bit orientations with respect to the applied magnetic field. 110

Chapter 1 – Introduction

Radio frequency identification (RFID) has become an increasingly important tool in a wide array of applications. Radio frequency identification involves the use of interrogators (also called readers) and transponders (also called tags) to wirelessly query, transmit, and capture data through radio waves. A reader requests and collects information from the tags, which can then be used for a variety of purposes. RFID systems have been put to use in electronic toll collection [2, 3, 4, 5, 6], building and parking lot access [2, 3, 4, 5, 6, 7, 8], library book tracking [3, 5, 9, 10], supply chain management [3, 4, 5, 6, 11, 12, 13], anti-theft [3, 4, 5, 13, 14], personnel identification [3, 4, 5, 13], marathon participant monitoring [13], and even animal tracking on farms [3, 5, 4, 13]. RFID tags are classified as active, semi-active, or passive depending on the components and properties of the tags. Passive RFID tags based on surface acoustic wave (SAW) devices possess properties that inherently address the flaws of IC-based equivalents, but current SAW-based RFID tags lack field programmability (the ability to program the information on the tag).

The research performed in this thesis investigates the possibility of creating a magnetically-programmable surface acoustic wave (MP SAW) device for use in RFID applications. A one-bit proof-of-concept device is designed and characterized in this work with the purpose of creating a SAW-based RFID tag that can be programmed in the field. Reindl and Ruile fabricated a SAW RFID tag that could be programmed, but it required wirebonding to change each bit, which is not feasible to do in the field [15]. Fu et al. discovered a method to program a single bit of data for a SAW-based RFID tag using a physical resistive switch [16, 17]. The research performed in this thesis attempts to further advance this work by integrating the switching element directly into the SAW device using a thin film stack that has a variable resistance depending on the magnetic field applied to it. Based on a single-port surface acoustic wave device, MP SAW devices were developed with the purpose of showing that an integrated giant magnetoresistive (GMR) element could be used in place of a discrete resistive switch as a data storage element for SAW-based RFID tags.

This thesis is organized into 6 chapters. Chapter 1 provides an introduction and motivation to the research being performed. Chapter 2 describes the concepts of RFID, SAW devices, GMR elements, and their pertinence to the research performed for this thesis. Chapter 3 discusses the design theory and considerations taken for the MP SAW devices fabricated. Chapter 4 presents the fabrication processes and techniques used to create the prototype MP SAW devices, as well as a detailed description of the experimental setup and measurements. Chapter 5 presents the measurement results and data with a discussion of the implications of the experiments. Chapter 6 gives conclusions and provides recommendations for future work.

Chapter 2 – Literature Review

Chapter 2 provides a literature review of radio frequency identification technologies, the principles behind their operations, and a summary of important applications. A discussion of concepts important to the operations of MP SAW devices is also provided, including surface acoustic waves, interdigital transducers, piezoelectric substrates, and giant magnetoresistance.

2.1 Radio Frequency Identification (RFID)

Radio frequency identification (RFID) technologies have gained increasing importance in today's world. Since the introduction of RFID during World War II as a means of tracking friendly aircraft with radar [3, 4, 5, 12], RFID technologies have since branched out to numerous other applications. The list of applications is continually growing as the technologies are being modified and applied to new niches.

2.1.1 Description and Overview

RFID technologies encompass a range of devices and systems used to wirelessly transmit data through radio waves. An RFID system consists of a reader and a tag, as depicted in Figure 2.1. An RFID reader transmits a modulated radio wave, receives an encoded response from the RFID tag, and decodes the response. An RFID tag is typically a device that stores and transmits data to a reader. There are three classifications of RFID tags: active, semi-active, and passive.

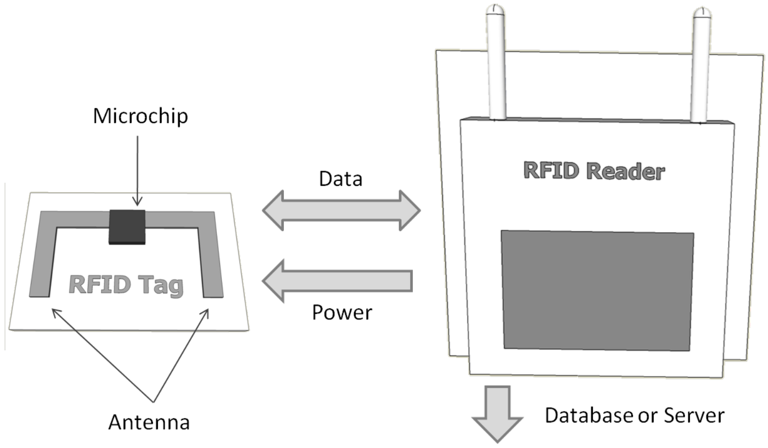

Figure 2.1: A depiction of a passive RFID tag and associated reader is shown. The reader sends out an interrogation signal, which is then read by the tag, and an encoded identification signal is then transmitted back to the reader.

Active tags have an onboard power source and do not require power transmitted from the reader to operate. Typically, active tags contain digital circuits and/or microprocessors. Active tags are capable of transmitting data without the presence of a reader and can broadcast data at relatively long ranges compared to the other types of tags.

Semi-active tags, also called battery-assisted tags, have an onboard power source as well, but require the reader's emitted power to transmit the stored data. Compared to passive tags, semi-active tags can transmit at longer ranges in less time when interrogated by a reader, and consume less power than active tags. Unlike active tags, the semi-active tag must first acknowledge the interrogation signal sent from the reader in order to send a transmission signal.

Passive RFID tags are of particular interest due to the fact that they do not require an onboard power supply. They are small compared to active and semi-active RFID tags, and they can be made at relatively low cost. Passive tags rely on the power emitted from the reader to power the tag, access the data stored on it, and transmit the stored data as a reply to the reader. This lack of an onboard power supply inherently gives passive tags the advantage of having a longer life.

2.1.2 Passive RFID Tags

The rest of the RFID review will discuss passive RFID technologies due to the fact that the MP SAW device being developed has similar properties and competes in the same application space. Passive RFID tags have become predominant due to the large number of applications in which they can be used. One of the most rapidly expanding applications for passive RFID tags is asset and product tracking in supply chains. Both Walmart and the US Department of Defense recently mandated the use of passive tags in logistics and asset management [3, 12]. The reasons for the move from bar code and optical-based identification to passive RFID includes increased automation in distribution, improved product tracking, and real-time awareness of available stocks and supplies. Passive RFID tags used in industry can be broken into two classes: tags based on integrated circuits (ICs) and tags based on SAW devices.

Passive RFID devices based on integrated circuits (ICs) have become the most popular implementation of RFID due to their compatibility with modern electronic designs and fabrication techniques. A typical passive RFID tag based on integrated circuits is composed of a microchip and an antenna (or coupling element). The microchip is typically composed of five components: An antenna impedance matching circuit, a power rectifier, a modulator/demodulator, a digital logic block, and a memory block. A typical block diagram of a passive RFID tag based on ICs is shown in Figure 2.2. The antenna impedance matching circuit is necessary to minimize reflections caused by impedance discontinuities between the antenna and the microchip. Since the RFID tag is exclusively powered by the incident interrogation signal from the reader, it is critical that the antenna can transfer as much of the reader's signal to the microchip. A power rectifier converts the interrogation signal from the reader into DC power to energize the rest of the microchip.

A modulator/demodulator unit decodes the commands from the reader's interrogation signal (demodulator) and encodes the data transmitted back to the reader (modulator). Typical modulation schemes used include amplitude-shift keying (ASK), frequency-shift keying (FSK), and backscatter modulation [6]. Backscatter modulation is the most predominant scheme for passive RFID tags. In backscatter modulation, the tag uses the incident power from the reader and remodulates the

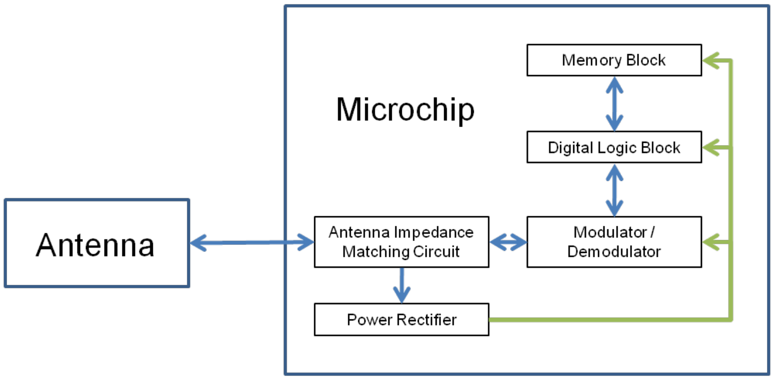

Figure 2.2: A block diagram of a typical IC-based passive RFID tag is shown. RF signal lines are represented in blue and DC power lines are represented in green.

received signal for the transmission sent back to the reader.

A logic block translates decoded commands from the reader, accesses the appropriate data from memory, and implements the communication protocol between the tag and the reader. For systems where readers simultaneously handle more than one tag, anti-collision protocols are also implemented in the digial logic block so that concurrent signals that arrive at the reader from multiple tags can be independently recognized. Memory blocks store data that is read and translated by the logic block, modulated by the modulator, and then transmitted as radio waves back to the reader.

SAW-based, passive RFID tags are used less extensively than IC-based passive tags, but have properties that make them better suited for certain niche applications. An in-depth review of SAW devices is provided in the second section of the literature review.

2.1.3 Passive RFID Applications

Passive RFID tags are currently used in a variety of applications. Five application categories are discussed — each taking advantage of the benefits of mobility and wireless data transfer. The key applications include: anti-theft, security and building access, electronic payment, asset tracking and monitoring, and supply chain management.

In the late 1960's and early 1970's, passive RFID technologies were found suitable for anti-theft applications. Companies such as Sensormatic and Checkpoint developed tags that could be attached to retail items [5]. In 2009, the Nottingham Centre for Retail Research surveyed 41 countries and found retail losses due to crime and waste were in excess of US$114.8 billion. Shoplifting in the United States and Canada accounted for US$48.9 billion of that loss [18]. RFID tags have been effective theft deterrent devices due to their ability to wirelessly monitor inventory at entry and exit points in retail stores.

Building and facility electronic access controls have been around for a long time, but it wasn't until the 1990's that wireless methods became widespread. Passive RFID technologies employed for access control use tags with unique identities and readers attached to control points. The readers scan the unique identification of the tag and compare it to a database which contains the identities that are authorized to access the control point.

Electronic payment that uses systems based on passive RFID tags has the advantages of speed and convenience for consumers. Removing the need to handle checks, cash, and giving change means reduced time in line for consumers. Although in its infancy, RFID-based payment systems have many benefits for retailers as well. Faster transaction times result in higher customer throughput, higher customer satisfaction and stronger loyalty. Additionally, data can be collected on customer purchasing habits.

Asset tracking and monitoring using passive RFID tags have been employed in libraries for book and media management, as well as in airports for luggage management. Such a system increases automation, reduces potential human error, and provides superior tracking compared to traditional barcode-based systems. Passive RFID tags have been implemented for races when manually timing each individual participant becomes impractical.

Supply chain management involves the control and management of information and supplies in the logistics process ranging from acquisition of source materials to the distribution to customers. RFID implementation in supply chain management provides the ability to track pallets and containers without the need for labor-intensive line-of-sight scanning associated with bar codes [19]. With the increased automation remote readers at warehouse entry/exit points can provide, labor costs can be substantially reduced.

2.2 Surface Acoustic Wave Devices

Surface acoustic waves are mechanical waves that travel along the surface of an elastic material. First described by Lord Rayleigh in 1885, surface acoustic waves have been employed as the primary operating mechanism in many electronic devices including filters and sensors. Surface acoustic wave (SAW) devices are typically composed of electro-mechanical transducer structures built on a piezoelectric substrate. The transducer structures convert an applied electrical signal into mechanical surface waves and vice versa. The amplitude of the wave diminishes exponentially with depth into the bulk of the material.

In 1965, R. M. White and F. W. Voltmer published the first experimental results from what could be considered the first modern SAW device and developed the interdigital transducer (IDT) structure. The IDT has since become the predominant transducer structure for SAW devices. Since 1965, SAW device development continued with their first applications as pulse compression filters and band pass filters in radar systems, funded by the United States military. In the 1980's and 1990's, SAW devices found a niche as oscillators, low pass filters, band pass filters, convolvers, and resonators for microelectronic devices or electronic appliances. SAW device development has continued into the 21st century with a renewed focus on wireless sensors and identification systems [20, 21, 22, 23, 24].

2.2.1 Surface Acoustic Wave Device Components

SAW devices consist of two important components: a piezoelectric substrate and a transducer structure. Each component plays an important role in the generation of surface waves.

2.2.1.1 Piezoelectricity and Piezoelectric Substrate

SAW devices exploit the piezoelectric effect to create surface acoustic waves from the electric field generated by the transducers. Piezoelectricity describes the ability of some materials to generate an electric potential when a mechanical stress is applied to them. Materials that exhibit the piezoelectric effect also exhibit the inverse piezoelectric effect where an applied electric field generates a mechanical stress in the material. The extent to which a material exhibits the piezoelectric effect and inverse piezoelectric effect is dependent on its crystalline anisotropy and center of inversion. When a mechanical stress is applied to a crystalline material that lacks a center of inversion, the net distribution of charge on the atoms and bonds in the crystal lattice changes measurably.

Mathematically, piezoelectricity can be described by the coupling of the elastic constitutive relation and the electromagnetic constitutive relation. The strain field and electric field equations are given by equations 2.2.1 and 2.2.2.

$$T = c - e_{Ij}E \tag{2.2.1}$$

$$D = \epsilon + e_{iJ}S \tag{2.2.2}$$

where T represents the stress vector components, c is the elastic stiffness constant matrix, e_{Ij} and e_{iJ} are piezoelectric stress matrices (subscripts describe that the two matrices are inverses of each other), E is the electric field components, D

is the electrical displacement vector components, ϵ is the permittivity constant matrix, and S is the strain vector components. Equations 2.2.1 and 2.2.2 completely describe the interactions between stress, strain, and electric field in a piezoelectric material.

Surface acoustic waves propagating on piezoelectric materials are composed of a compressional wave and a shear wave coupled together, along with an electrostatic wave. Generated surface acoustic waves create a wave front perpendicular to the direction of the wave propagation as depicted in Figure 2.3. The displacement of particles in the piezoelectric substrate is dependent on the lattice structure of the material and the applied potential across the material. The energy associated with surface waves is confined to the surface of the piezoelectric substrate. The SAW displacement decays exponentially into the depth of the piezoelectric material by a factor of $e^{-\frac{2\pi y}{\lambda}}$ where y is the depth of the surface wave and λ is the wavelength of the SAW [25]. For a SAW wavelength of 48 µm, 90% of the energy associated with the SAW will be present within 17.6 µm of the surface. The shear wave component is an elastic deformation perpendicular to the direction of wave motion, and is also called a transverse wave. The compressional wave component is a compression of the medium parallel to the direction of the wave motion and is also called a longitudinal wave. The combination of the coupled compressional and shear wave causes particles within the piezoelectric material to displace in a periodic, elliptical motion with respect to time.

The displacement of a surface acoustic wave propagating in the x-direction can be described mathematically by equation 2.2.3 [25, 26].

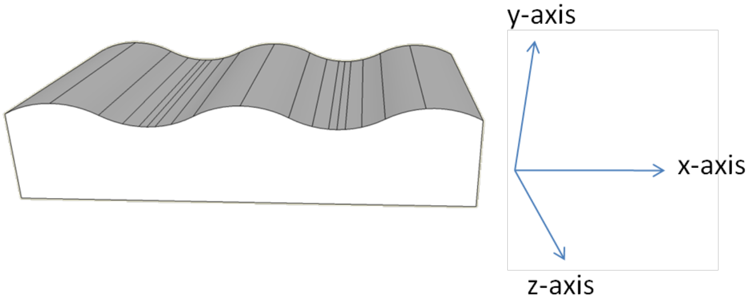

Figure 2.3: A surface acoustic wave is shown propagating across a piezoelectric material. Compression waves cause deformation and particle displacement along the x-axis, and shear waves cause deformation and particle displacement along the y-axis. The displacement is limited to roughly one wavelength into the depth of the piezoelectric material.

$$u\left(x,y,z,t\right)=\left(u_xe^{j\phi_1}\widehat{x}+u_ye^{j\phi_2}\widehat{y}+u_ze^{j\phi_3}\widehat{z}\right)\left(e^{j\omega t-\gamma_x}\right) \tag{2.2.3}$$

where u_x, u_y, and u_z are displacement constants in their respective directions with units of m. ϕ_1, ϕ_2, and ϕ_3 are the phases of the components referenced to u_x and have units of degrees. ω is the angular frequency with units of rad/s. t is the time variable with units of s. Finally, γ_x is the complex propagation factor.

The electrostatic wave in a piezoelectric substrate describes the periodic generation of an electric potential amplitude dependent upon the mechanical deformation of the piezoelectric substrate at a given point and time. The electric potential induced on the surface of the piezoelectric substrate can be described similar to a traveling wave as [26, 27, 28]:

$$\Phi\left(x,y,t\right)=\Phi_0e^{[j(\omega t-kx)]}e^{[-k(|y|)]} \tag{2.2.4}$$

where Φ is the electrical potential in units of V (with respect to position and time). Φ_0 is the time/position independent constant in units of V. ω is the angular frequency of the wave generation in units of rad/s. t is the time in units of s. k is the wave vector in units of m^{-1}. x is the position along the direction of propagation in units of m, and y is the position along the direction normal to the substrate surface in units of m. From Equation 2.2.4, the electric fields produced in each direction can be described by equations 2.2.5, 2.2.6, and 2.2.7:

$$E_x = -\frac{\delta\Phi}{\delta x} \tag{2.2.5}$$

$$E_y = -\frac{\delta\Phi}{\delta y} \tag{2.2.6}$$

$$E_z = 0 \tag{2.2.7}$$

where E_x, E_y, and E_z are electric field components in their respective directions with units of V/m, Φ is the electrical potential as defined in equation 2.2.4 with units of V, x is the position of interest along the direction of wave propagation with units of m, and y is the position of interest along the direction normal to the unperturbed piezoelectric substrate surface with units of m. Using the coordinate system specified in Figure 2.3, spatial variations of the electric potential in the x-direction is caused by the compressional wave displacement, while the spatial variations of the electric potential in the y-direction is caused by the shear wave displacement. No change occurs in the z-direction due to the uniformity of the wave in that direction.

Common piezoelectric substrates used in SAW devices include lithium niobate, lithium tantalate, and quartz. Lithium niobate and lithium tantalate are widely used due to their high mechanical/electrical coupling properties, which allows for the maximum interaction between stress and electric field. Table 2.1 [25, 27, 26, 29] provides properties of common piezoelectric materials used for fabricating SAW devices.

Material	**Orientation** [cut-direction]	v_{saw} [m/s]	K^2 [%]	TCD [ppm/°C]	$\frac{\Delta v}{v}$ [%]	$\frac{\varepsilon_p}{\varepsilon_0}$ [N/A]
$LiNbO_3$	Y-Z	3488	4.5-4.6	94	2.41	50.2
$LiNbO_3$	128° rot.	3992	5.3-5.6	75	2.72	-
Quartz	Y-X	3159	0.18	-24	0.09	4.52
Quartz	ST-X	3158	0.11	0	0.06	4.55
$LiTaO_3$	Y-Z	3230	0.72	35	0.33	47.9
$LiTaO_3$	167° rot.	3394	1.5	64	0.75	47.9
$Bi_{12}GeO_{20}$	001-110	1681	1.4	120	0.68	43.6
$Bi_{12}GeO_{20}$	40.04° rot	1830	0.62	-	0.31	43.6
$Li_2B_4O_7$	X-Z	3542	1.0	0	0.51	-
$GaAs$	001-110	2868	0.07	52	0.04	-

Table 2.1: Common piezoelectric substrate materials and their properties, including SAW velocity (v_{saw}), electro-mechanical coupling coefficient (K^2), SAW propagation temperature coefficient of delay (TCD), relative velocity change ($\frac{\Delta v}{v}$), and relative dielectric permittivity constant ($\frac{\varepsilon_p}{\varepsilon_0}$) where ε_0 is the permittivity of free space and ε_p is the permittivity of the material.

2.2.1.2 Interdigital Transducers

Surface acoustic waves are generated by a transducer structure on the surface of a piezoelectric material that converts an applied electrical signal into a mechanical wave. Interdigital transducers (IDTs), consisting of interleaved metal electrodes alternately connected to two different bus bars, are two-terminal, planar transducer structures for creating surface acoustic waves on piezoelectric substrates.

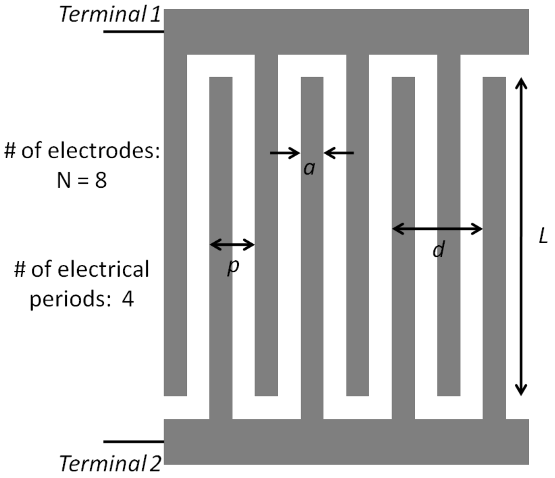

Figure 2.4: A depiction of a single-electrode interdigital transducer. The single-electrode design is composed of alternating electrode bars with a thickness, a, of the same dimension as the spacing between alternating electrodes. The mechanical period, p, is the distance between the front edge of one metal electrode to the front edge of the neighboring electrode. The electrical period, d, is the distance between the front edge of an electrode to the front edge of the next electrode at the same potential. The aperture width, L, is the width of the electrode overlap between the two bus bars. Finally, N is the number of electrodes present in the IDT. To get the number of periods, the number of electrodes is divided by the number of electrodes in one electrical period.

When a voltage is applied between the two terminals (buses) of the IDT, electric fields are generated within the piezoelectric substrate, which creates a periodically alternating stress pattern on the substrate. These stresses in the piezoelectric substrate give rise to traveling surface waves, which have an optimal wavelength, λ, equal to the electrical period, d, of the IDT as represented in Figure 2.4. The IDT generates SAWs with a wavelength equivalent to the electrical period of the IDT, operating with a center frequency defined by equation 2.2.8:

$$f_0 = \frac{v_0}{d} \tag{2.2.8}$$

where v_0 is the SAW velocity on the piezoelectric substrate, and d is the electrical period as shown in Figure 2.4.

Due to the symmetry of the transducer, SAWs are generated and launched along the x-direction defined in Figure 2.4, resulting in only half of the power radiating in a direction. Typically, acoustic absorbers are placed on the edges of the piezoelectric substrates to dampen or eliminate wave reflections caused by the mechanical discontinuity. Since its first implementation in 1965 by White and Voltmer [30, 31], IDTs have yet to be supplanted as the dominant transducer structure for SAW devices. This can be attributed to the IDT's high transduction efficiency, ease of fabrication using lithographic techniques already well-developed for the semiconductor industry, and relatively simple design.

Parameters that are of importance for IDT design include the electrode width, a, mechanical period, p, electrical period, d, aperture width, L, number of electrodes, N, and the order of electrode polarities. Figure 2.4 provides a schematic reference for the parameters listed above. The electrode width, mechanical period and the electrical period determine the impedance and static capacitance of the IDT. The calculations for the impedance and static capacitance will be demonstrated in Chapter 3. The electrical period also determines the wavelength of the surface waves produced across the piezoelectric substrate. The aperture width is taken into consideration to reduce SAW attenuation that could occur due to diffraction. The number of electrodes is important for determining the impedance of the transducer structure, and also for determining the bandwidth of SAW devices used as filters. The ordering of electrode polarities in an IDT determines the electrical period, and consequently, the wavelength of the SAW. SAW reflections and potential sources of wave interference, such as constructive interference between mechanical and electrical reflections, can be enhanced or eliminated depending on the ordering of the electrode polarities.

When the mechanical period is half the electrical period, surface waves generated by the IDT mechanically reflect off of incident electrodes constructively, resulting in significant surface wave reflections that could degrade the IDT performance and the associated SAW device. When the electrical period is doubled by ordering the electrode polarities from a "+ - + - ..." configuration to a "+ + - - + + - - ..." configuration, the mechanical period becomes a fourth of the electrical period, resulting in the mechanical reflections being minimized due to destructive interference. This is discussed more explicitly in Chapter 3.

Various IDT designs and configurations exist for different applications. Different electrode polarity configurations have different reflected wave patterns due to the discrepancies between the mechanical and electrical periods [32, 1, 33]. An example of an IDT with a single-electrode design and a double-electrode design are shown in Figure 2.5 (a) and (b) respectively. The use of apodized electrodes is also common, in which the electrodes of the IDT overlap at different positions and with different lengths along the IDT. The pattern of the apodized electrodes determines response of the IDT [28, 26, 34]. An example of an apodized IDT is shown in Figure 2.5 (c). Varying electrode widths in the same IDT has been found to be beneficial in SAW sensor applications, due to the fact that it allows for multiple operating frequencies to be generated or monitored at the same time. This is crucial when there is frequency-dependent interference present in the system being measured [35]. Figure 2.5 (d) provides an example schematic of a multi-frequency IDT design.

Contrary to the IDT's physical layout, the behavior and interactions of the IDT with the piezoelectric substrate are quite complex. Multiple models have been developed to describe and predict the behavior and properties of IDTs. The earliest models were developed by Coquin and Tiersten [36], Joshi and White [37], and Skeie [38], and while they provided insight into IDT behavior, they were not as useful for device analysis due to the complexity and model limitations [31]. Equivalent network models, developed by Smith et al [34], were able to more fully describe IDTs. The models simulated the IDT as an array of bulk wave transducers and assumed that the electric field generated between the electrodes of the IDT were either vertical, in the case of the crossed-field model, or horizontal, in the case of the in-line model [39].

A simpler approach was developed by Tancrell and Holland [40, 41], which described the generation of the waves as a line source at the edge of each electrode. This model, more commonly referred to as the delta function model, is able to provide information about the general shape of the frequency response of the IDT, but lacks the ability to determine the transducer impedance, insertion loss, and the distortions associated with the terminating impedances. IDT modeling and design used for the research will be discussed in Chapter 3.

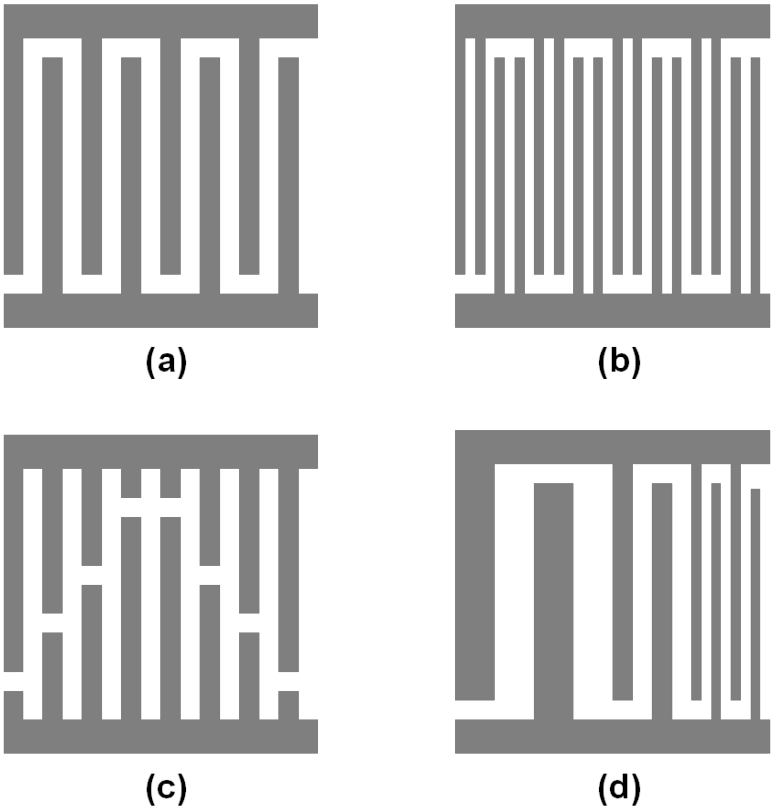

Figure 2.5: Various IDT designs are presented in schematic form: (a) Single-electrode IDT with the charge polarities alternating every electrode. (b) Double-electrode IDT with the charge polarities alternating every other electrode. (c) IDT with apodized electrodes (d) Multi-frequency IDT with varying electrode widths

2.2.2 Surface Acoustic Wave Device Operations

The operations section will describe how two important SAW devices operate: SAW delay lines and SAW transponders.

2.2.2.1 Surface Acoustic Wave Delay Lines

A SAW delay line consists of two transducers, typically IDTs, on a piezoelectric substrate. The transducers are spaced some distance from each other, with the apertures of the two transducers in line with each other as shown in Figure 2.6. The input signal is applied to one of the transducers (known as the transmitting transducer), which converts the electrical signal into a potential that generates surface waves on the piezoelectric substrate. The surface waves propagate across the substrate to reach the other transducer (known as the receiving transducer) where the surface waves produce a periodic deformation on the surface of the substrate, resulting in a potential between the alternately polarized transducer electrodes. This potential is read as an electric signal by the metal transducer structure, which can then be outputted.

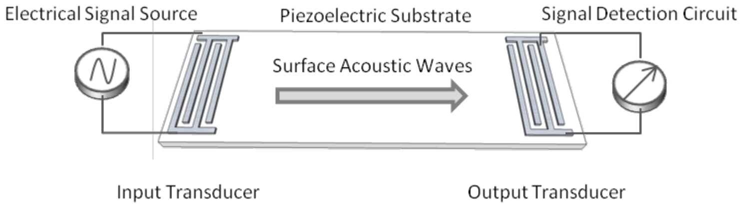

Figure 2.6: Depiction of a SAW delay line.

SAW delay lines are typically used in electronic filters and sensors. For a typical SAW delay line, the overall transfer function is typically given as the product of the transmitting and receiving IDT frequency-domain responses multiplied by a phase delay term, assuming that amplitude decay during propagation is negligible. SAW sensors have been shown to quantitatively detect temperature, force, torque, pressure, acceleration, and gas concentration. Gases and vapors including CO, HCl, H_2, H_2S, NH_3, NO_2, SO_2, and hydrocarbons have been detected and measured via mass loading and/or the functionalization of the piezoelectric surface [42]. In the presence of a measurand, typically a strain or a damping force is placed on the piezoelectric substrate, which in turn, changes the phase and the SAW velocity through the substrate surface.

2.2.2.2 Surface Acoustic Wave Transponder

A typical SAW device used as a wireless identification tag (also called a SAW transponder) operates based on transduction and surface wave reflection principles. A high-frequency electromagnetic wave is launched from an interrogation unit and then received by an antenna structure. The antenna structure is connected to an interdigital transducer to allow for RF-to-SAW transduction. Reflectors similar in design as the interdigital transducer are placed in the acoustic path of the surface waves at varying intervals. The reflectors partially reflect the surface waves back towards the interdigital transducers connected to the antenna. The reflected surface waves are converted back into electromagnetic waves due to the piezoelectric effect as the surface waves encounter the interdigital transducer. The electromagnetic waves are then transmitted via the connected antenna, which are then detected by the interrogation unit. Depending on the spacing of the reflector structures on the piezoelectric substrate, a unique electromagnetic signal is produced. A depiction of a SAW RFID tag is shown in Figure 2.7.

Surface acoustic wave devices used for sensor and identification systems have several key benefits. SAW devices can be wirelessly interrogated from up to several meters away, do not require a direct line of sight to query, and do not require an onboard power supply since the interrogation unit provides all the necessary energy in the form of electromagnetic waves. SAW devices are typically fabricated on single crystal substrates, providing the benefits of long, maintenance-free operation, and the ability to deploy in hazardous environments with minimal operational impact. Devices have been shown to operate in extreme heat beyond 200°C, extreme cold below -195°C, strong radiation, high vacuum conditions, high voltage environments, high chemical contamination environments, and shock-prone conditions [43, 44]. Wireless operation, fast measurement, and fast read-out capabilities of the technology have attributed to the use of SAW devices in identification (ID) and sensor applications that require monitoring moving or rotating structures [45] . The devices can be made relatively small, on the order of a few millimeters across, and are relatively easy to manufacture since the fabrication processes required are routinely used to make silicon-based microelectronics, and have been well-characterized.

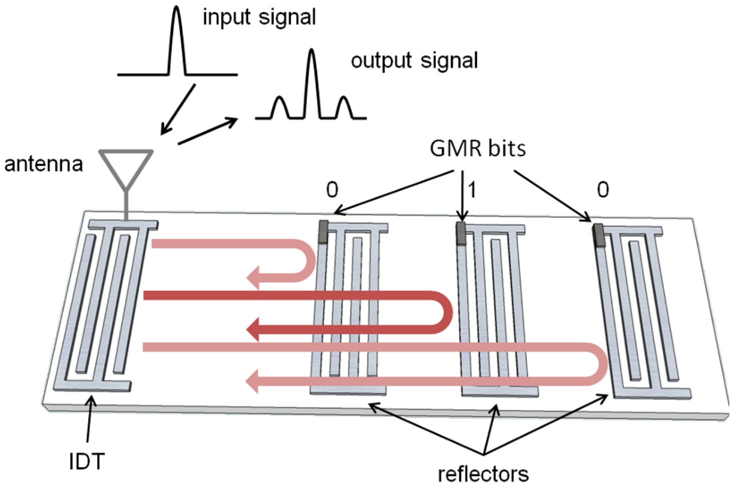

Figure 2.7: Depiction of a SAW RFID tag.

2.3 Giant Magnetoresistance

The principles of magnetoresistance are exploited in this research as a data storage element. A magnetoresistive element is used in conjunction with IDT structures to act as tunable reflectors. Magnetoresistance is the change of electrical resistance in a material due to an applied magnetic field. In the case of giant magnetoresistance or GMR, the change of the electrical resistance is due to an applied magnetic field changing the electron scattering properties of a magnetic layer or set of magnetic layers in an ordered thin film stack. GMR was first discovered in alternating Fe/Cr mulitlayer stacks by two groups headed by Fert [46, 47, 48] and Grünberg [48, 49] respectively in 1988. The electrical resistance was shown to decrease by up to 50% when a relatively large magnetic field was applied [46, 50]. The thin film stack is typically composed of alternate layers of magnetic metal separated by layers of a non-magnetic metal as shown in Figure 2.8. GMR materials have seen wide commercial success with its use in hard disk read heads. Two conditions must be met for giant magnetoresistance to occur. First, the relative orientations of the magnetization of adjacent magnetic metal layers must be able to change. Second, the thickness of the non-magnetic magnetic layers must be a fraction of the mean free path of an electron in the thin film stack [50].

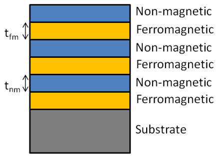

Figure 2.8: A multilayer, GMR thin film stack is portrayed, composed of 6 layers.

2.3.1 Giant Magnetoresistance Description

A GMR thin film can be modeled as material layers containing two types of electrons: electrons with a "spin up" state and electrons with a "spin down" state. The alternating magnetic metal layers will each have a magnetization that is associated with the "spin up" state or the "spin down" state of the electrons. Scattering processes, such as interfacial scattering, increase collision rates between electrons with the spin state not favored by the magnetization of the magnetic metal layer, decreasing the mean free path of those electrons and effectively driving up the electrical resistance. For electrons with the spin state favored by the magnetization of the magnetic metal layer, scattering is reduced, increasing the mean free path of the electrons, and consequently lowering the electrical resistance. Ideally, the direction of the magnetization of the magnetic metal layers will be such that only the “spin up” or “spin down” electron state is exclusively favored.

Looking at an example GMR thin film stack with just two magnetic metal layers separated by a non-magnetic metal layer, there are two configurations: a high resistance configuration and a low resistance configuration. If the two magnetic metal layers have parallel magnetizations that favor the “spin up” electrons, then “spin up” electrons can traverse freely through the GMR material stack, while the “spin down” electrons are scattered. This principle can be shown by representing the magnetic metal layers as a resistor network as shown in Figure 2.9. The two magnetic layers are modeled as resistors in series, and the electron spin states are modeled as parallel branches (one branch representing “spin up” electrons and the other branch representing “spin down” electrons). R_1 represents the electrical resistance of an electron that is favored by the magnetic layer’s magnetization. R_2 represents the electrical resistance of an electron that is scattered due to its spin state being unfavored by the magnetization of the magnetic layer. R_2 has a larger resistance compared to R_1. In the example, when the two magnetic layers are anti-parallel, the resistance of the GMR stack is defined as $R_{AP} = \frac{R_1+R_2}{2}$. When the two magnetic layers are parallel, the resistance of the GMR stack is less than that of the anti-parallel state, and is given by $R_P = \frac{2R_1R_2}{R_1+R_2}$. Mathematically, it can be shown that the anti-parallel resistance, R_{AP}, is going to be larger than the parallel resistance, R_P, assuming that the the electrical resistance of the favored electrons, R_1, is different than the resistance of the unfavored electrons, R_2, with the following:

$R_{AP} > R_P$ assuming $R_1 \neq R_2$

$\frac{R_1+R_2}{2} > \frac{2R_1R_2}{R_1+R_2}$

$(R_1 + R_2)^2 > 4R_1R_2$

$(R_1 + R_2)^2 - 4R_1R_2 > 0$

$(R_1 - R_2)^2 > 0$

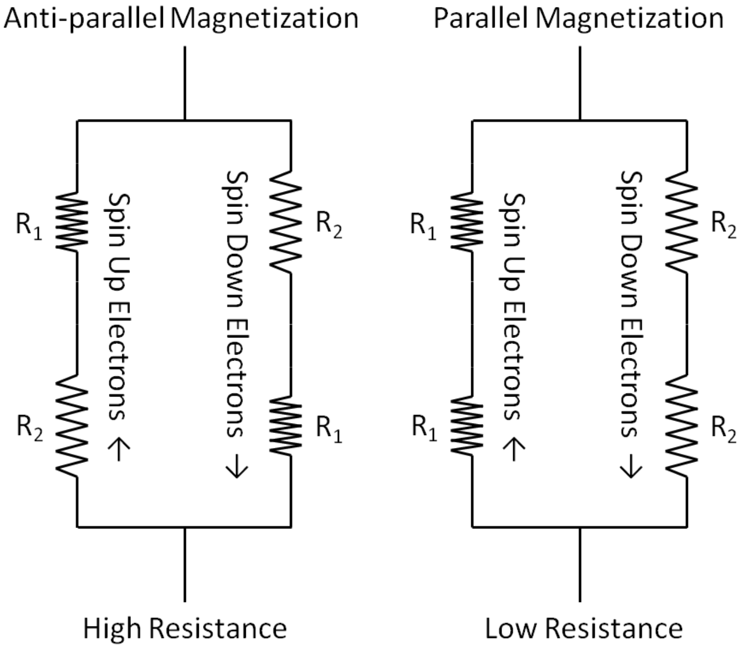

Figure 2.9: Giant magnetoresistance equivalent resistor network for the anti-parallel and parallel alignment of magnetic layers. In this example, $R_1 < R_2$ in terms of resistance. The anti-parallel state will have a larger equivalent resistance compared to the parallel state.

2.3.2 Giant Magnetoresistive Film Stack Types

GMR thin films are found in a variety of configurations, each with their advantages and disadvantages. There are four primary classifications of GMR thin film stacks: multilayer GMR, spin valve GMR, pseudo-spin valve GMR, and granular GMR [51]. Figure 2.10 provides a cross-section representation of each GMR film stack type.

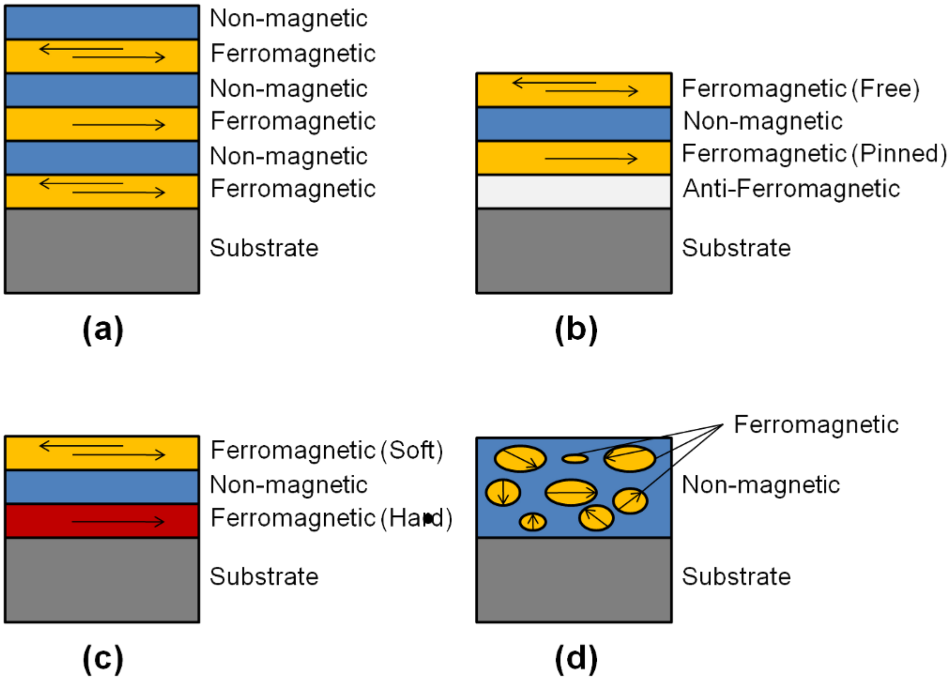

Figure 2.10: Cross-sections of the four different types of GMR films stacks are presented: (a) Magnetic multilayer, (b) spin valve, (c) pseudo-spin valve, and (d) granular thin film. The layers with arrows in the opposite directions represent layers that can their magnetization reoriented in the direction of an applied magnetic field.

Multilayer GMR thin films are made up of multiple ferromagnetic layers separated by extremely thin non-ferromagnetic layers. The coupling between adjacent ferromagnetic layers is antiferromagnetic (anti-parallel magnetization) due to Ruderman-Kittel-Kasuya-Yosida (RKKY) interactions [52, 53, 54]. The exchange coupling between adjacent ferromagnetic layers is dependent upon the thickness of the non-magnetic spacer layer, oscillating between ferromagnetic and antiferromagnetic coupling.

Spin valve GMR thin films make use of only two ferromagnetic layers with a thin, non-magnetic spacer layer between them. For spin valve GMR films, the magnetization of one of the ferromagnetic layers is pinned in one direction by an adjacent antiferromagnetic layer due to the exchange coupling. The pinned ferromagnetic layer effectively has a different coercive field than the unpinned (free) ferromagnetic layer, allowing for the magnetization of the two layers to change independently, determined by the strength of the applied magnetic field. The unpinned ferromagnetic layer is free to rotate in the applied magnetic field. Although spin valves require more than two types of materials (typically more than four materials are used), smaller applied magnetic fields are required to change the resistance of the thin film stack.

Pseudo-spin valve GMR thin films are similar in composition and design to spin valve GMR thin films, but instead of using two ferromagnetic layers with the same coercivity and one of them pinned by an antiferromagnetic layer, pseudo-spin valves have two dissimilar ferromagnetic layers, with one being composed of a soft ferromagnetic material and the other being composed of a hard ferromagnetic material. Pseudo-spin valve GMR films use the differences in the coercive fields between the two ferromagnetic layers to reorient the magnetization of the two layers at different applied magnetic fields. Typically the thickness of the non-magnetic layer between the two ferromagnetic layers is thicker than in spin valve and multilayer GMR thin films to keep exchange coupling to a minimum.

Granular GMR films involve the use of ferromagnetic precipitates or granules suspended in a non-magnetic material. The magnetic moments of the ferromagnetic granules are aligned by an applied magnetic field that lowers the resistance of the film. An example of a granular GMR thin film matrix is cobalt granules in a copper film, which can be created through rapidly cooling a molten mixture of copper and cobalt [55].

For this research, spin valve GMR thin films were used. The exact specifications and properties of the spin valve GMR thin film are provided in Chapter 3. This type of GMR film was chosen due to the fact that it is relatively easy to manufacture using a sputter system, and it requires relatively low fields to change resistance states.

Chapter 3 – SAW Device Design

Chapter 3 discusses the theory and design of the SAW devices developed for this thesis. Two designs were fabricated: a single-electrode and a double-electrode IDT configuration, commonly used in SAW devices. Piezoelectric substrate selection, IDT impedance calculations, delta-function modeling of SAW device, and qualitative IDT reflector analysis will be addressed in this chapter.

3.1 Piezoelectric Substrate Selection

Y-cut, Z-propagating (Y-Z) lithium niobate was selected as the piezoelectric substrate for fabricating MP SAW devices. This cut of lithium niobate has an electromechanical coupling coefficient of 4.5% (K^2 as shown in Table 2.1), which is needed for strong signal transduction. The SAW propagation velocity is dependent on the crystal lattice of the piezoelectric substrate which is important for determining the resonant/center frequency and the time delay. For Y-Z lithium niobate, the SAW propagation velocity along the Z-axis has been experimentally determined to be 3,488 m/s [26, 28, 41, 56].

One potential drawback of the substrate is its relatively high temperature coefficient of delay, 94 ppm/$°C$ (as listed in Table 2.1). This implies that room temperature fluctuations will cause changes in SAW velocity, which will affect the center frequency of a SAW device. Lithium niobate is also known to be a brittle, pyroelectric material that is prone to shattering. Thermal shock from high-temperature fabrication processes can be avoided by decreasing the temperature ramp rate or by eliminating such steps altogether. Strong electro-mechanical coupling exhibited in lithium niobate makes modeling SAW devices based on this substrate more complex since second order effects such as electrical loading and wave regeneration are not negligible [32, 38, 57].

A 100 mm diameter Y-Z lithium niobate wafer with a blanket GMR thin film stack, deposited by NVE Corporation, was diced into 25.4 mm x 25.4 mm squares to fabricate devices at Oregon State University (OSU). Three 76 mm diameter Y-Z lithium niobate wafers were used to fabricate devices at the U.S. Army Research Laboratories, with each wafer being diced into 9 mm x 9 mm squares.

3.2 Interdigital Transducer Design

The IDT provides the means for signal reception, processing, and transmission for the MP SAW devices fabricated in this research. For an IDT, the electrode length and width, the number of electrodes, the electrode polarity pattern, and the spacing of the electrodes are important, independent design parameters that affect SAW device performance. These variables control the IDT impedance, surface wave interactions, center/resonant frequency and bandwidth, which in turn determine the signal response. Two IDT designs predominantly described in the literature were selected for this research; the single-electrode (abbreviated to S-E) IDT and the double-electrode (also called split-finger and abbreviated as D-E) IDT are shown in Figure 2.5 (a) and (b) respectively. The electrode polarity alternates every other electrode in the single-electrode design while the electrode polarity alternates every two electrodes in the double-electrode design.

Impedance calculations were performed to determine the dimensions and number of the electrodes for the IDTs. It is ideal to design the IDT structures to match the impedance of the other components in the system. In the case of this research, a network analyzer with a 50 Ω input impedance is connected to the IDT to measure S-parameters of the device. The delta-function model was used to provide insight on the frequency response of the IDT designs. While not capable of addressing all the second-order effects, it is still possible to acquire important information from the results of the model. Finally, a qualitative analysis of an IDT with varying resistance between the two terminals was explored to determine the effects on the reflection response as a function of the resistance.

To design a SAW device with a center frequency (also called the resonant frequency), f_0, the electrical period, d, of the IDT must be equal to the wavelength, λ, of the desired SAW to be generated. The relationship between the center frequency and the SAW wavelength is given by Equation 2.2.8 in Chapter 2.

An electrical period of 48 µm was used for the SAW devices fabricated at the U.S. Army Research Laboratories (ARL). This electrical period was chosen due to photolithographic limitations of the fabrication process, which could produce device features down to 5 µm. The electrode widths of the IDTs were 12 µm and 6 µm for SAW devices based on the S-E design and D-E design respectively. An electrical period of 144 µm was used for the SAW devices fabricated at Oregon State University. Photolithographic limitations with mylar masks restricted the smallest feature size to be greater than 10 µm, The electrode widths of the IDTs for Oregon State devices were 18 µm for the S-E designs and 36 µm for the D-E designs.

3.2.1 Interdigital Transducer Impedance

Impedance matching of the IDTs is important for minimizing signal attenuation and reflections at the interfaces between SAW devices and the measurement equipment. Nearly all independent parameters of the IDT affect its complex impedance. Engan [1] and Morgan [26] have analytically described the complex impedance by calculating the complex admittance. The equivalent circuit for an IDT is given in Figure 3.1. The components of the equivalent circuit include the radiation conductance, $G_a(f)$, the acoustic susceptance, $B_a(f)$, and the static capacitance, C_T.

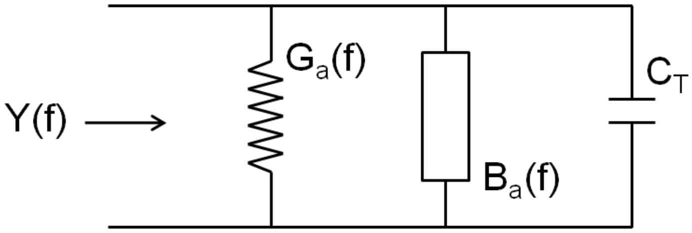

Figure 3.1: The equivalent circuit representation of an interdigital transducer. $Y(f)$ is the admittance of the IDT, $G_a(f)$ represents the radiation conductance, $B_a(f)$ represents the acoustic susceptance, and C_T represents the static capacitance.

Equation 3.2.1 describes the total complex admittance:

$$Y\left(f\right) = G_a\left(f\right) + j\omega B_a\left(f\right) + j\omega C_T \tag{3.2.1}$$

where all components of the admittance equation are dependent on the frequency of the IDT. The impedance, $Z\left(f\right)$, is defined as the inverse of the admittance, $Y\left(f\right)$: $Z\left(f\right) = \frac{1}{Y(f)}$.

From Engan's analysis [1], the radiation conductance at the resonance frequency is defined by Equation 3.2.2 below:

$$G_a\left(f_0\right) = 2\pi f_0 L\left(\varepsilon_0 + \varepsilon_p\right) K^2 \left(\frac{sin\left(\pi s\right)}{P_{-s}\left(-cos\Delta\right)}\right)^2 R_t \left(1 + \delta\left(s, \frac{1}{2}\right)\right) \tag{3.2.2}$$

where each variable is described in Table 3.1. The derivation of the radiation conductance determined by Morgan [26] is in agreement with Equation 3.2.2, although the approach was somewhat different.

The acoustic susceptance (also called the reactive admittance), $B_a\left(f\right)$, is defined by Morgan [26] as

$$B_a(f) \approx G_a\left(f_0\right)\frac{sin\left(2X\right) - 2X}{2X^2} \tag{3.2.3}$$

where $X = \frac{\pi N_p(2\pi f - 2\pi f_0)}{2\pi f_0}$ and all other variables are described in Table 3.1. At the center frequency though, the acoustic susceptance goes to zero: $B_a\left(f_0\right) = 0$.

The final component of the admittance and equivalent circuit of the IDT is the

Variable	Units	Definition
f_0	MHz	resonance/center frequency
L	mm	aperture width of the IDT
ε_0	F/m	permittivity of free space
ε_p	F/m	permittivity of piezoelectric substrate
K^2	$none$	electro-mechanical coupling coefficient
S_e	$none$	number of electrodes per electrical period
s	$none$	${}^1\!/\!_{S_e}$
Δ	$none$	$\frac{\pi a}{p}$ = geometric factor
a	μm	electrode width
p	μm	mechanical period (electrode + spacing)
$P_{-s}\left(x\right)$	$none$	Legendre function of the first kind
R_t	$none$	factor for electrode polarity pattern
$\delta\left(s, \frac{1}{2}\right)$	$none$	$\begin{cases} 1, \ s = 1/2 \quad 0, \ s \neq 1/2 \end{cases}$
N_p	$none$	number of electrical periods in an IDT

Table 3.1: Table of definitions for variables associated with the radiation conductance, reactive admittance, and static capacitance as described by Engan [1].

static capacitance. C_T, is given by Equation 3.2.4:

$$C_T = 2L\left(\varepsilon_0 + \varepsilon_p\right) sin\left(\pi s\right) \frac{P_{-s}\left(cos\Delta\right)}{P_{-s}\left(-cos\Delta\right)} R_t N \tag{3.2.4}$$

Solving at the resonant frequency, f_0, the admittance of the IDT can be simplified to $Y\left(f_0\right) = G_a\left(f_0\right) + j\left(2\pi f_0\right) C_T$. The impedance of the IDT at the resonant frequency can then be described as

$$Z\left(f_0\right) = \frac{1}{Y\left(f_0\right)} = \frac{1}{G_a\left(f_0\right) + j\left(2\pi f_0\right) C_T} \tag{3.2.5}$$

.

The electrode width, a, mechanical period, p, and electrical period, d, as shown in Figure 2.4, were determined based on the minimum feature size that could be produced at the two respective facilities devices were fabrication. Table 3.2 provides a list of important material properties of the substrate used for calculating the impedance of the IDT. Table 3.3 provides a listing of the independent design parameters used for each of the four IDT designs created. These design parameters were selected while considering the 50 Ω impedance of the measurement equipment and the photolithographic feature size limitations in the cleanrooms. Table 3.4 provides a listing of parameters dependent on the polarity pattern of the electrodes and the independent IDT parameters needed for calculating the admittance and impedance of the IDT designs.

Parameter	Description	Value
K^2	elctromechanical coupling	0.046
ε_p	permittivity of $LiNbO_3$	442.71x10$^{-12}F/m$
$\varepsilon_p/\varepsilon_0$	normalized $LiNbO_3$ permittivity ratio	50
v_0	SAW velocity in Z-dir of $LiNbO_3$	3488m/s

Table 3.2: List of material properties for Y-Z lithium niobate that are important for calculating the resonant frequency and impedance of an IDT fabricated on top of the piezoelectric substrate.

From Tables 3.2, 3.3, and 3.4, and the equations detailed earlier in this chapter, important IDT properties are calculated and compiled in Table 3.5. During the design phase of the IDTs, it should be noted that Legendre polynomial estimates were used instead of the more precise Legendre functions to calculate the impedance. Calculations provided in Table 3.5 below make use of the more accurate Legendre functions as better calculations tools became available. This explains why the impedance values of the IDTs displayed in Table 3.5 are not 50 Ω.

Parameter	Description	OSU SE	OSU DE	ARL SE	ARL DE
a	electrode width	$36\mu m$	$18\mu m$	$12\mu m$	$6\mu m$
p	mechanical period	$72\mu m$	$36\mu m$	$24\mu m$	$12\mu m$
d	electrical period	$144\mu m$	$144\mu m$	$48\mu m$	$48\mu m$
N	number of electrodes	48	84	30	48
L	IDT aperture width	$10mm$	$10mm$	$5mm$	$5mm$

Table 3.3: List of independent design parameters for the four IDT designs: (OSU SE) = OSU-fabricated single-electrode design, (OSU DE) = OSU-fabricated double-electrode design, (ARL SE) = ARL-fabricated single-electrode design, and (ARL DE) = ARL-fabricated double-electrode design. A physical representation associated with each of the listed parameters can be found in Figure 2.4.

Parameter	Description	S-E*	D-E*
S_e	# of electrodes per electrical period	2	4
s	$1/S_e$	1/2	1/4
R_t	electrode polarity factor	1/4	1/4
$\delta\left(s, {}^{1}\!/_{2}\right)$	single electrode correction factor	1	0
$\Delta = \pi a/p$	geometric factor	$\pi/2$	$\pi/2$

Table 3.4: List of design dependent parameters used for the impedance calculations. Values are dependent on the electrode polarity configuration. * S-E = single-electrode design, D-E = double-electrode design

3.2.2 Interdigital Transducer Modeling

The delta function model, was used to determine the qualitative frequency response differences between the S-E and D-E electrode designs fabricated for this research.

3.2.2.1 Single-Electrode IDT Frequency Response

For a uniform, single-electrode IDT design, all electrodes are of identical length and width as shown in Figure 2.5 (a). When a potential is applied across the terminals

Property	OSU SE	OSU DE	ARL SE	ARL DE	Equation
f_0	24.2 MHz	24.2 MHz	72.7 MHz	72.7 MHz	2.2.8
$G_a\left(f_0\right)$	0.0236 S	0.0391 S	0.0138 S	0.0192 S	3.2.2
$jB_a\left(f_0\right)$	0 S	0 S	0 S	0 S	3.2.3
C_T	$9.99x10^{-11}$F	$1.75x10^{-10}$F	$3.12x10^{-11}$F	$4.99x10^{-11}$F	3.2.4
$Y\left(f_0\right)$	0.0280 S	0.0473 S	0.0198 S	0.0298 S	3.2.1
$Z\left(f_0\right)$	35.7 Ω	21.1 Ω	50.4 Ω	33.6 Ω	3.2.5

Table 3.5: Calculated properties of the four IDT designs: (OSU SE) = OSU-fabricated single-electrode design, (OSU DE) = OSU-fabricated double-electrode design, (ARL SE) = ARL-fabricated single-electrode design, and (ARL DE) = ARL-fabricated double-electrode design.

of an IDT, an electric field is generated in the gap between the alternately polarized electrodes, generating surface waves on the piezoelectric substrate. The location where the surface waves are generated is defined as in the center of the gap between the electrodes as illustrated in Figure 3.2.

The amplitude of the surface waves generated are directly proportional to the potential difference between neighboring electrodes. Surface waves are generated in the positive and negative directions normal to the aperture width of the electrodes, resulting in 50% of the energy from the transduction being unavailable in the direction of interest. The wave amplitude of a SAW launched from one of the line sources is given by:

$$\psi_s\left(x,t\right) = EV_te^{j\omega t}C_me^{jk_0(x-x_m)} \tag{3.2.6}$$

where V_t is the applied potential across the IDT terminals, E is the element factor, ω is the frequency in rad/s, t is time, C_m is the term that describes the

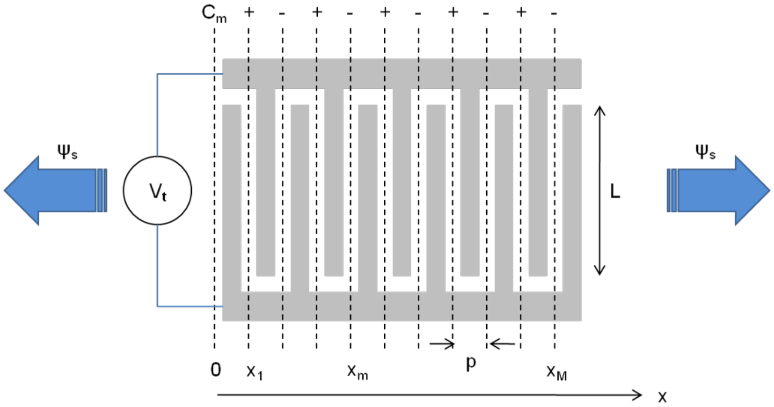

Figure 3.2: Illustration of a SAW generating IDT. An applied voltage is placed across the IDT terminals to generate SAWs between the oppositely polarized electrodes represented by the line sources centered in between the electrodes. The polarity of the electrodes is described by term C_m. The distance between the line sources generating the SAWs is given as p. There are M line sources.

line source polarity (+ or -), k_0 is the wave number defined as $k_0 = \frac{\omega}{v_0}$, v_0 being the propagation velocity of the SAW, and x_m is the location of the m-th line source. The element factor, E, describes the metallization ratio of the electrodes in the IDT, as well as electrode neighbor interactions. The element factor can be approximated as a constant for a given design, and the frequency dependence can be neglected.

The total amplitude of the wave amplitude generated by the IDT is the sum of all the line source contributions and can be described as:

$$\psi_{sT}\left(x,t\right) = EV_t e^{j\omega t} e^{jk_0 x} \sum_{m=1}^{M} C_m e^{-jk_0 x_m} \tag{3.2.7}$$

where the M is the total number of line sources in the IDT. The element factor, applied potential, the temporal phase term, and the positional phase term are considered constant at some specified point and time. The summation term, $A(\omega)$ is the array factor, which provides information about the shape of the frequency response based on the number of electrodes, the positions of the electrodes, and their polarities. For this analysis, the magnitude of the array factor provides all the information necessary to ascertain the shape of the frequency response.

For the single-electrode IDT design, C_m can be substituted with $e^{j\pi m}$ (which alternates polarities for every line source, m), and x_m can be substituted with mp, where p is the distance between line sources of the S-E IDT as portrayed in Figure 3.2. Using the geometric series partial sum definition, $A(\omega)$ can be described as a sinc function:

$$A(\omega) = \sum_{m=1}^{M} e^{j\pi m} e^{-jk_0 mp} = \frac{1 - e^{j(\pi - k_0 p)M}}{1 - e^{j(\pi - k_0 p)}} = \frac{\sin([k_0 p - \pi] M/2)}{\sin([k_0 p - \pi]/2)} e^{j(k_0 p - \pi)\frac{(1-M)}{2}} \tag{3.2.8}$$

Taking the magntiude of the array factor and substituting $2\pi f/v_0$ for k_0:

$$|A(\omega)| = \left| \frac{\sin\left(\left[\frac{2\pi f}{v_0 p} - \pi\right] M/2\right)}{\sin\left(\left[\frac{2\pi f}{v_0 p} - \pi\right]/2\right)} \right| \tag{3.2.9}$$

Equation 3.2.9 provides the frequency response for the SAWs launched from the IDT. For the SAW devices and the reflection measurements that were performed in this research, the frequency response of the reflected waves can be qualitatively described by this equation. SAWs were generated from an IDT, propagated through the piezoelectric substrate until encountering a reflector. The SAWs were reflected back to the IDT, where the SAWs are transduced back into a signal. Since the receiving IDT is the same IDT used to generate the SAWs, from reciprocity, the same frequency response is expected. Assuming that the frequency response of the SAW amplitude is not modified by the reflector structure, the outputted frequency response is given as $|A(\omega)|^2$. Based on the S-E design parameters used for the ARL-fabricated devices specified in Table 3.3 the frequency response for the ARL S-E IDT design is plotted in Figure 3.3. A SAW velocity of 3488 m/s in lithium niobate was used for v_0. The peak amplitude is at the center frequency (72.67 MHz for the ARL SE design) with an equally high amplitude peak at the 3rd harmonic of the center frequency (frequencies in the plot are normalized to the center frequency).

3.2.2.2 Double-Electrode IDT Frequency Response

Double-electrode IDTs, shown in Figure 2.5 (b), follow the same theory as the S-E IDT designs, but instead of having oppositely polarized electrodes, the electrode periodicity of D-E IDTs is composed of two electrodes with the same polarity equally spaced apart from each other followed by two electrodes with matching polarity opposite of the first pair, spaced evenly apart. From a delta-function analysis standpoint, when considering the locations of the SAW line sources, the D-E IDT can be thought of as two S-E IDTs that are offset from each other by $p/2$ where p is the distance between the line sources in the S-E design. This is shown

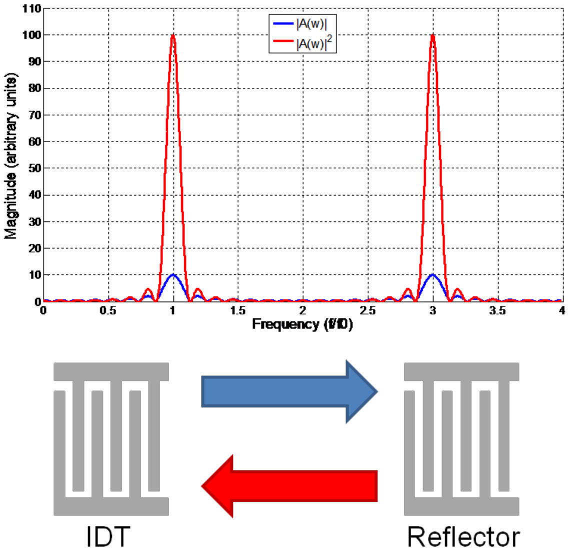

Figure 3.3: The shape of the frequency response for a single-electrode IDT is dictated by the array factor calculated with equation 3.2.9. Launched SAWs have a frequency response indicated in blue above. For SAWs reflected back, the frequency response at the IDT is the square of the array factor magnitude.

in Figure 3.4 allows for the use of the same analysis performed for the S-E IDT frequency response.

For the wave amplitudes at individual line sources in between the oppositely polarized electrodes, equation 3.2.6 is still valid. The total amplitude of the surface wave generated by the D-E IDT is the sum of all the line source contributions for the two S-E IDTs:

$$\psi_s\left(x,t\right) = EV_t e^{j\omega t} e^{jk_0 x} \left[\sum_{m=1}^{M} C_m e^{-jk_0 x_m} + \sum_{n=1}^{N} C_n e^{-jk_0 x_n} \right] \tag{3.2.10}$$

where the M is the total number of line sources from one of the S-E IDTs representing the D-E IDT, and N is the total number of line sources for the other

S-E IDT. The element factor, applied potential, the temporal phase term, and the positional phase term are the same and constant for both S-E IDT representations. Substitutions can be made for the two summations, with $C_m = e^{j\pi m}$, $C_n = -e^{j\pi m}$, $x_m = mp$, and $x_n = \left(m + \frac{1}{2}\right) p$ where the extra 1/2 in x_n represents the positional offset of the SAW sources. Applying the geometric series partial sum definition as before, $A(\omega)$ is:

$$A(\omega) = \frac{\sin\left(\left[k_0 p - \pi\right] M/2\right)}{\sin\left(\left[k_0 p - \pi\right]/2\right)} \left(e^{j(k_0 p - \pi)\frac{(1-M)}{2}} + e^{j(k_0 p - \pi)\frac{(1-M)}{2}} e^{-j(k_0 p/2)}\right) \tag{3.2.11}$$

The magnitude of the array factor for the D-E IDT is:

$$|A(\omega)| = \left|\frac{\sin\left(\left[k_0 p - \pi\right] M/2\right)}{\sin\left(\left[k_0 p - \pi\right]/2\right)}\right| \left(\sqrt{2}\sqrt{\cos\left(\frac{k_0 p}{2}\right) + 1}\right) \tag{3.2.12}$$

The array factor magnitude of the D-E IDT is similar to the S-E IDT with an additional factor that suppresses the frequency response about the 2nd harmonic and amplifies the frequency response about the 1st and 3rd harmonics of the center frequency as shown in Figure 3.5. Parameter values of the ARL devices were taken from Table 3.3. As with the S-E SAW devices, to determine the frequency response of the reflected waves, the frequency response of the launched SAWs is multiplied with the frequency response (transfer function) of the receiving transducer structure. In this case, the same D-E IDT that launched the SAWs is also used to receive. By reciprocity, the frequency response should be $|A(\omega)|^2$ with $|A(\omega)|$ defined by equation 3.2.12. The frequency responses after launch of the surface waves and after reception at the D-E IDT are presented in Figure 3.6.

3.2.3 Reflector Structures

An interdigital reflector structure is an IDT that is used to reflect acoustic waves in this research, reflector structures were integrated into both S-E and D-E designs as shown in Figure 2.5 (a) and (b) respectively. The reflection coefficient associated with the interdigital reflector changes as a function of load impedance across the terminals of the reflector. In this research, a GMR bit is used as a programmable resistive load to change the reflection coefficient of the reflector. By changing the resistive load with the use of an applied magnetic field, the magnitude of the reflections can be changed and detected. The generation of SAW reflections from IDT structures can be contributed to mechanical and electrical loading (MEL) and regenerated waves [26, 32, 27, 28, 56, 58, 59].

3.2.3.1 Reflections from Mechanical and Electrical Loading

Mechanical loading generates reflections due to the presence of different wave impedances on the substrate surface at the interfaces between the metal electrodes of the IDT and the air gap/bare substrate regions in between the electrodes. Electrical loading generates reflections due to the presence of the metal electrodes shorting out electric fields on the surface of the piezoelectric substrate underneath the electrodes. Electrical loading can limit performance of the transducers when the piezoelectric substrate has a strong electro-mechanical coupling coefficient. The presence of the electrodes cause a velocity change in the SAWs, which can distort the center frequency and change the frequency response of the SAW device. Although the perturbations at each electrode is small, the reflected waves add coherently when the electrode spacing or mechanical period is half the electrical period or SAW wavelength.

The reflections from mechanical and electrical loading can be described qualitatively for a S-E reflector and a D-E reflector. For a propagating SAW with a wavelength λ that is equal to the electrical period d of the interdigital reflector, consider the acoustic reflections that occur at the interface between the edge of the metal electrode and the free substrate surface for a S-E reflector and a D-E reflector. For the S-E reflector with an electrode spacing of $\frac{\lambda}{2} = \frac{d}{2}$, reflected waves constructively interfere with each other, contributing to a larger reflected wave amplitude. For the D-E reflector with an electrode spacing of $\frac{\lambda}{4} = \frac{d}{4}$, the reflected waves destructively interfere with each other, effectively cancelling out the reflections. Figure 3.7 illustrates what effects the IDT design has on the generation of reflected waves. For the research being performed in this thesis, reflections from mechanical and electrical loading (MEL) are undesirable due to the fact that they cannot be easily controlled. Positionally spacing the electrodes so that the mechanical period is not equal to the half of the SAW wavelength (and half of the electrical period) will dramatically reduce MEL reflections.

3.2.3.2 Reflections from Regenerated Waves

In substrates with strong electro-mechanical coupling, “regenerated waves” are produced. Surface waves are “regenerated” in the interdigital reflector by the voltage induced from incident surface waves which strain the piezoelectric substrate about the metal electrodes. Incident waves on an interdigital reflector transduces a potential across the electrodes the interdigital reflector (inverse piezoelectric effect). Subsequently, the potential across the interdigital reflector, applies a mechanical stress to the piezoelectric substrate, which then transduces and launches surface waves in both directions normal to the reflector aperture (piezoelectric effect). The magnitude of the regenerative waves are very dependent upon the load impedance between the interdigital reflector’s two terminals and the strength of the electromechanical coupling of the piezoelectric substrate.

Unlike MEL-generated reflections, regenerated waves are transduced from a potential and are not true reflections at an impedance mismatch. Rather, new wave fronts are generated in the same fashion as described in the delta function model. Unlike the applied potential purposefully induced between the IDT terminals to generate SAWs, the voltage source that transduces regenerative waves comes from other incident SAWs on the interdigital reflector. Both S-E and D-E interdigital reflectors will have reflections from regenerated waves if the piezoelectric substrate has a strong electromechanical coupling coefficient. While the spatial placement of the electrodes does not affect the suppression or amplification of regenerative waves, regenerated waves are affected by the impedance loading between the two terminals of the interdigital reflector.

Consider the open-circuited case for both an S-E and D-E reflector. Applying an AC signal to the two sets of electrodes, an electric field is generated in between oppositely polarized electrodes, creating SAW generation sources. These sources launch SAWs in both directions, but only SAWs launched toward the incident wave source are considered as reflections. Figure 3.8 illustrates how the regenerated waves reflect and constructively interfere with each other for open-circuited S-E and D-E reflector designs. The open-circuited case represents an infinite impedance between the two sets of electrodes in an IDT. Now consider the short-circuited case, which represents zero impedance between the two sets of electrodes in an IDT. No wave regeneration can take place since all electrodes in the interdigital reflector are forced to the same potential. This means no electrical fields can be set up between electrodes with opposite polarities to strain the piezoelectric substrate and generate surface waves. Figure 3.9 provides an illustration of the short-circuited case. Since a potential cannot be formed between electrodes, no SAWs are generated.

These two cases illustrate the ideal impedance loading scenarios for interdigital reflectors, with the open-circuited scenario representing the generation of reflections at its maximum magnitude, and the short-circuited scenario representing the generation of no reflections. For the research being performed, reflections from regenerated waves will be controlled by using a GMR bit as a two-state impedance load across an interdigital reflector. The two resistive states of the GMR bit will not be near the ideal scenarios, and an analysis will be performed to determine how impedance loading affects the reflection response.

3.2.3.3 Modeling of S_{11} Response as a Function of Interdigital Reflector Load Impedance

In the previous section, the IDT was described by the delta function model to describe the frequency response. For describing reflections from IDT structures and changes in reflection coefficient due to a resistive load, it is more convenient to use the three-port, P-matrix model developed by Tobolka [60] and the crossed-field equivalent circuit representation developed by Smith et al. [34]. The P-matrix representation and the crossed-field equivalent circuit representation describe the IDT with three ports: 2 acoustic ports and 1 electrical port. Figure 3.10 provides an equivalent circuit of an IDT with a variable impedance load between its terminals, Figure 3.11 provides a schematic representation of the P-matrix, and Table 3.6 provides a description for each of the 9 matrix elements.

Element	Units	Description
P11	unitless	Reflection acoustic scattering parameter *
P12	unitless	Transmission acoustic scattering parameter *
P13	$\sqrt{A/V}$	Electromechanical coupling element
P21	unitless	Transmission acoustic scattering parameter *
P22	unitless	Reflection acoustic scattering parameter *
P23	$\sqrt{A/V}$	Voltage-to-SAW transfer function
P31	$\sqrt{A/V}$	SAW-to-short circuit current transfer function
P32	$\sqrt{A/V}$	SAW-to-short circuit current transfer function
P33	S	The admittance of the IDT when no incoming SAWs are present

Table 3.6: Description of the 9 matrix elements associated with the P-matrix that fully describes an interdigital transducer. *The acoustic scattering parameters are defined for the short-circuited IDT (no voltage drop across port 3).

From the P-matrix model, the total reflection coefficient is given as:

$$P_{11t} = P_{11sc} + \frac{4P_{13}^2}{P_{33} + Y_{Load}} \tag{3.2.13}$$

where P_{11sc} is the reflection coefficient when the interdigital reflector is short-circuited and Y_{Load} is the admittance of the impedance load between the terminals of the interdigital reflector and possesses units of S. P_{13} and P_{33} are described in Table 3.6. The short-circuited reflection coefficient P_{11sc}, represents all reflections off of the reflector not associated with the load impedance, which typically includes MEL reflections. Since the P_{11sc} term of the total reflection coefficient cannot be modulated or controlled, adding unwanted reflections, it is typically minimized. This has been done through the use of double-electrode reflector designs [15, 17] and specific film thickness-to-electrical period ratios in single-electrode reflector designs [16, 17]. The term $\frac{4P_{13}^2}{P_{33}+Y_{Load}}$ represents the reflections associated with the load impedance across the reflector terminals, and includes the regenerated wave reflections. In the open-circuited scenario, $Y_{Load} = 0$, which simplifies equation 3.2.13 to $P_{11t} = P_{11sc} + \frac{4P_{13}^2}{P_{33}}$. In the short-circuited scenario, $Y_{Load} = \infty$, simplifying equation 3.2.13 to $P_{11t} = P_{11sc}$. If P_{11sc} is small, then the a large change in amplitude modulation is possible. To quantify this, calculations based on the crossed-field equivalent circuit model were performed to simulate the change in reflection response (normalized to the minimum reflection response) as a function of load resistance between the reflector terminals [58].

The the reflection scattering parameter (S-parameter), S_{11}, is directly proportional to the P-matrix reflection coefficient, P_{11}. If the change in reflection response is taken, normalized to the reflection response of the smallest resistance measured ($\Delta S_{11}/S_{11min}$), then the percent change in reflection response be approximated for a given resistance value. The reflection S-parameter can be calculated with:

$$S_{11} = \sqrt{\frac{(\omega C_T R_L)^2}{(\omega^2 C_T^2 R_L/G_a)^2 + (\omega C_T R_L + \omega C_T/G_a)^2}} = \sqrt{\frac{G_a^2}{(\omega C_T)^2 + (G_a + 1/R_L)^2}} \tag{3.2.14}$$

where G_a is the radiation conductance of the IDT structure, C_T is the static capacitance of the IDT structure, ω is the operating frequency, and R_L is the load impedance across the IDT terminals. Using the calculated values from the ARL-fabricated S-E and D-E IDT designs listed in Table 3.5 a plot of $((S_{11} - S_{11min})/S_{11min})$ as a function of R_{Load} taken at the center frequency was simulated and is shown in Figure 3.12. From the plot, it appears that the reflection response changes logarithmically and that smaller resistive loads should be used to see the most reflection change per change in load resistance. Note that the resistance range was chosen based on the calculated and measured resistance values of the GMR bits available. This will be discussed in the next section.

3.3 Giant Magnetoresistive Bits

The GMR bit is used as a magnetically-controllable resistive load across an interdigital reflector. As shown earlier in this chapter, the reflection coefficient associated with the interdigital reflector in a SAW device is dependent on the resistive load between its terminals. A GMR bit has low and high resistance states, and transitions between the states when a critical switching field is applied along the magnetization direction of the pinned layer. The magnetization direction of the pinned layer is typically along the easy axis of the GMR bit. The easy axis is the line along the GMR bit in which spontaneous magnetization is energetically favored. The easy axis is typically influenced by the shape of the GMR bit (shape anisotropy), and the direction of the exchange anisotropy of the antiferromagnetic layer and the neighboring ferromagnetic layer (pinned layer).

The GMR material used in this research was provide by the National Institute of Standards and Technology (NIST). The GMR thin film stack was deposited on a 760 mm (3”) lithium niobate wafer. The fabrication process for producing the GMR bits is described in Chapter 4. A cross-section of the GMR thin film stack is given in Figure 3.13. The thin film stack is a spin valve type of GMR, using an IrMn antiferromagnetic pinning layer and a Cu spacer layer in between the free ferromagnetic layer and pinned ferromagnetic layer.

The sheet resistance of the entire GMR thin film stack was provided by NIST. Sheet resistance is defined as $R_s = \frac{\rho}{t}$ where ρ is the resistivity (given in Ω-m) and t is the thickness of the thin film (given in µm) It should be noted that this is only valid when current is flowing in the plane of the thin film and not perpendicular to it. The low resistance state sheet resistance or the GMR bit was measured to be 11.67 Ω/□ while the high resistance state sheet resistance of the GMR bit was measured to be 12.12 Ω/□. The resistance of the GMR bit is directly proportional to the geometry of the bit and can be related to sheet resistance with equation 3.3.1:

$$R = \frac{\rho L}{tW} = R_s \frac{L}{W} \tag{3.3.1}$$

The GMR bit was geometrically designed to match close to 50 Ω. At this resistance value, the GMR bit would be in line with the impedance of the interdigital reflector it would be integrated with, and it would match the impedance of the cables and network analyzer connected to the MP SAW device. At no applied field, the GMR material was in a low resistance state (the free ferromagnetic layer is magnetically coupled parallel to the pinned ferromagnetic layer). The required magnetic field for switching the resistance state of the GMR bit, the hysteresis, and the approximate signal difference between the low and high states for the GMR material used in this research are shown in Figure 3.15, a plot of $\Delta R/R_{min}$ vs. applied field, and Figure 3.14, which plots the magneto-optic Kerr effect as a function of applied field. A magnetic field with a magnitude greater than 10 Oe aligned with easy axis of the GMR bit is required to switch the resistance states. The plot of $\Delta R/R_{min}$ vs. applied field confirms the given sheet resistance values. The percent change between the sheet resistance of the low and high state of the GMR material referenced to the low state was 3.9%, which corresponds with Figure 3.15.

The GMR bits were patterned with a length of $L = 500\,\mu m$ and a width of $W = 100\,\mu m$ at ARL. With these dimensions, the low resistance state of the GMR bit comes relatively close to a 50 Ω impedance. Using equation 3.3.1, the GMR bits will have a resistance of 58.35 Ω in the parallel or low resistance state, and a resistance of 60.60 Ω in the antiparallel or high resistance state. The GMR bit was fabricated between the terminals of an interdigital reflector as shown in Figure 3.16. From the theoretical calculations performed earlier in this chapter and plotted in Figure 3.12, the 2.25 Ω change between 58.35 Ω and 60.60 Ω should result in a change in S_{11} response (normalized to the smallest response in the data set) between 2.1% for S-E devices and 1.6% for D-E devices.

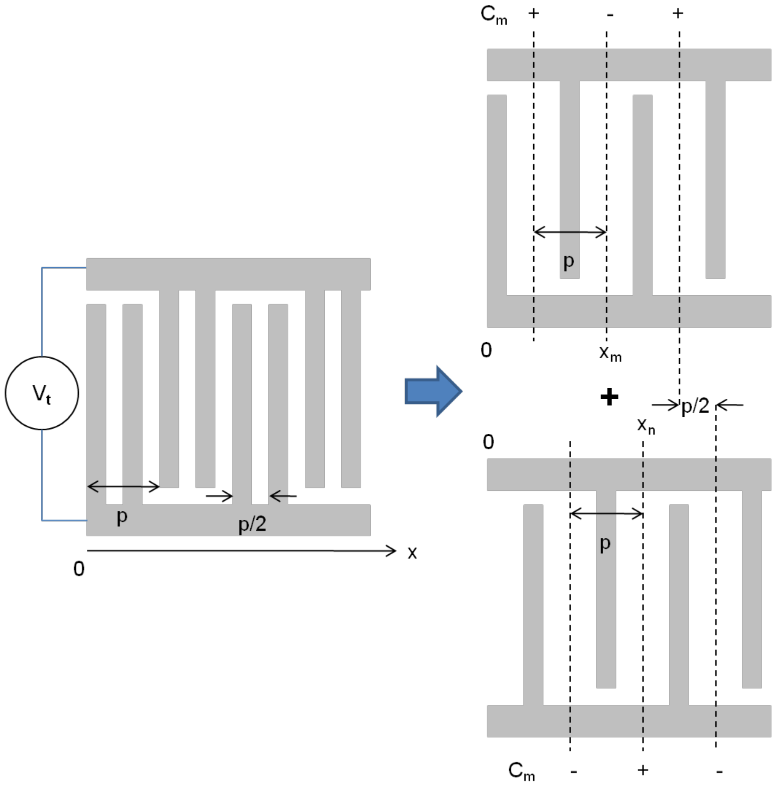

Figure 3.4: An illustration of a double-electrode IDT is shown. For the surface wave amplitude and frequency response calculations, the D-E IDT can be modeled as two S-E IDTs offset by p/2. The surface wave amplitude as a function of frequency is the summed results of the two S-E IDTs. With this method, the same analysis performed for the S-E IDT can be used to solve for the D-E IDT case.

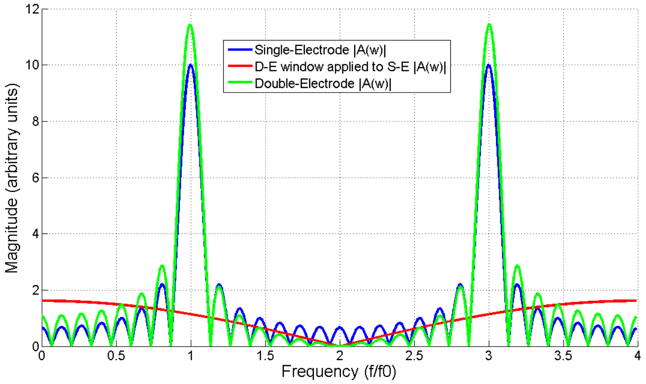

Figure 3.5: The array factor magnitudes for the S-E IDT design (blue) and the D-E IDT design (green) are plotted against frequency normalized to the center frequency (72.67 MHz). The array factor magnitude of the D-E IDT design was calculated by dividing the D-E IDT into two S-E IDTs with a positional offset of $p/2$ and then summing their wave amplitude contributions. The S-E array factor magnitude was multiplied by the D-E window function (red) to achieve the D-E array factor magnitude.

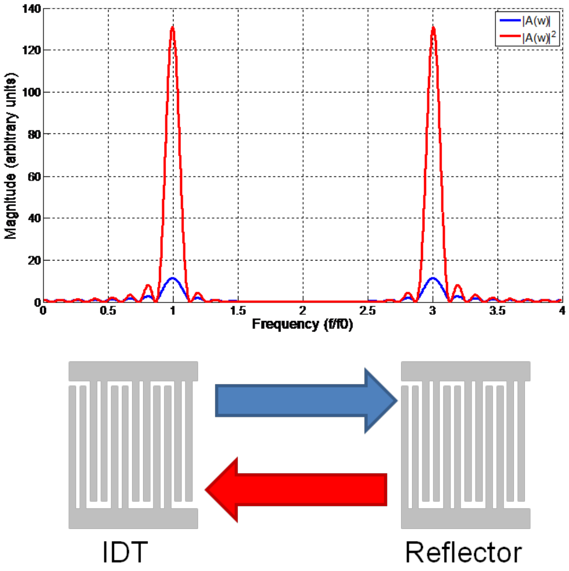

Figure 3.6: The shape of the frequency response for a double-electrode IDT is dictated by the array factor calculated with equation 3.2.12. Launched SAWs have a frequency response indicated in blue above. The frequency response at the receiving IDT after reflected waves return is the square of the array factor magnitude indicated in red. Note that the frequencies are normalized to the center frequency of the modeled IDT (72.67 MHz).

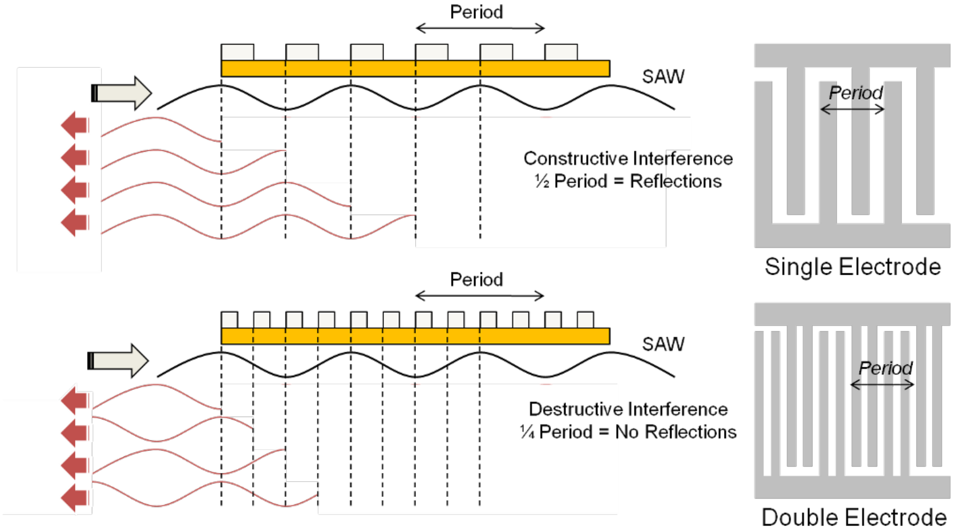

Figure 3.7: Illustration of SAW reflections from mechanical and electrical loading on a S-E reflector design and a D-E reflector design. For the S-E reflector, constructive interference of the reflected waves occur due to the $1/2$ wavelength spacing of the electrodes. For the D-E reflector, destructive interference of the reflected waves occur due to the $1/4$ wavelength spacing of the electrodes.

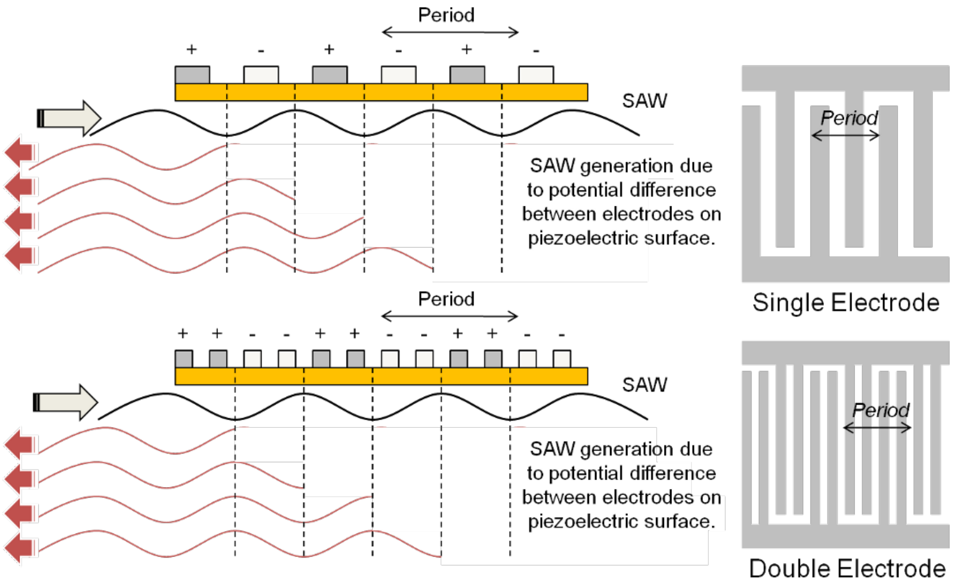

Figure 3.8: Illustration of generated SAWs in the direction of the incident waves (reflections) from regenerated waves due to strong electromechanical coupling. The S-E and D-E reflector designs both regenerate waves when there is an infinite impedance across the electrode terminals (open-circuited) due to the potential and subsequent transduction of SAWs generated from the incident surface wave.

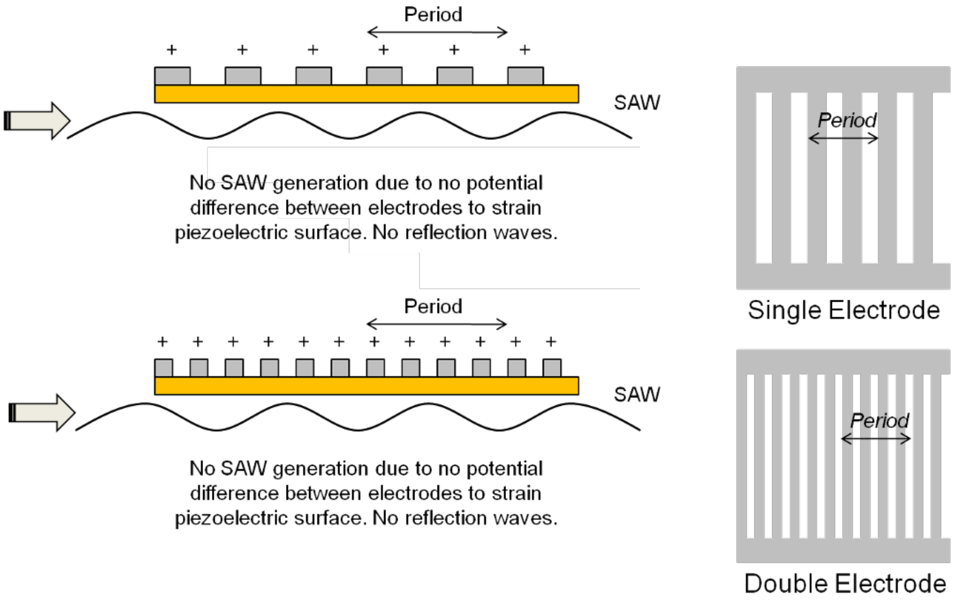

Figure 3.9: Illustration of shorted interdigital reflector structures. Surface waves are not regenerated due to the fact that no potential can be developed between the electrodes.

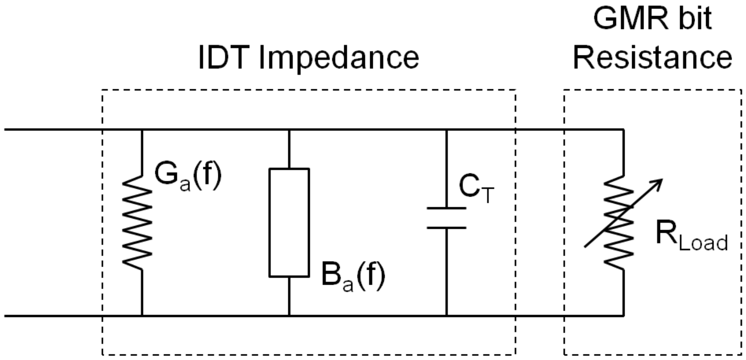

Figure 3.10: Equivalent circuit of the IDT impedance with a GMR bit resistive element. The GMR bit acts as a variable resistor load across the terminals of the IDT.

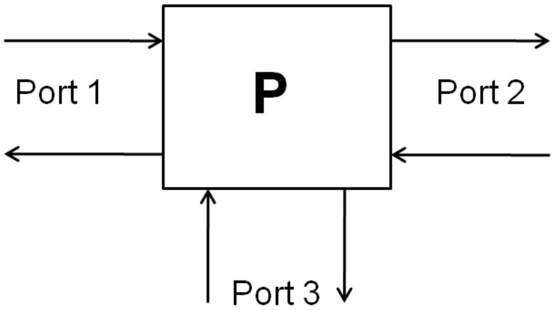

Figure 3.11: Schematic representation of the 3-port, P-matrix. Port 1 and port 2 are acoustical ports, and port 3 is the electrical port. The load impedance is placed across the terminals of port 3. The interactions between the ports are described by 9 matrix elements, which are listed in Table 3.6.

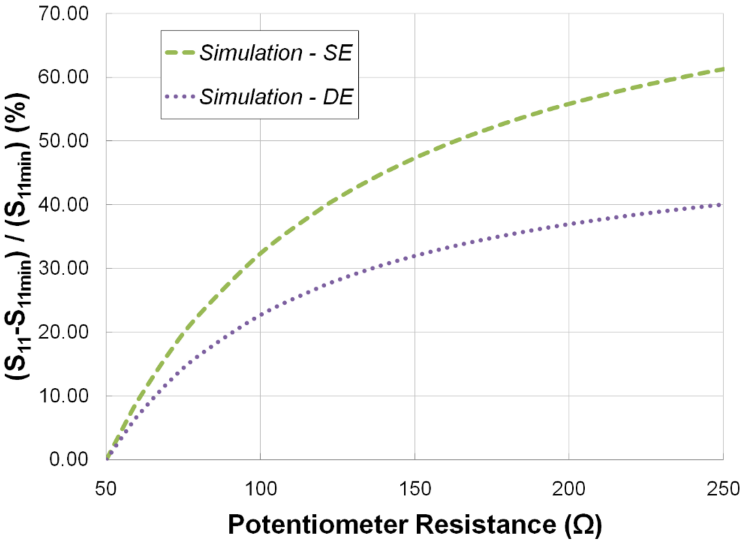

Figure 3.12: Simulated plots of the normalized S_{11} response $\left(\left(S_{11}-S_{11min}\right)/S_{11min}\right)$ as a function of resistive load across the interdigital reflector.

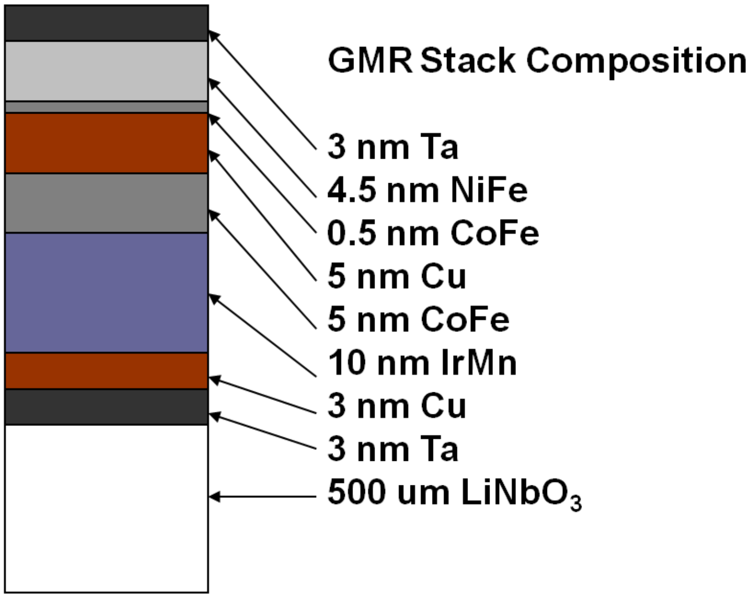

Figure 3.13: GMR thin film stack composition used for the development of MP SAW devices in this thesis.

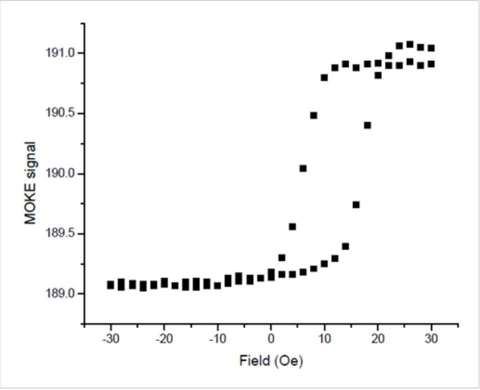

Figure 3.14: Magneto-Optical Kerr Effect (MOKE) plot characterizing the GMR thin film stack used for developing MP SAW devices.

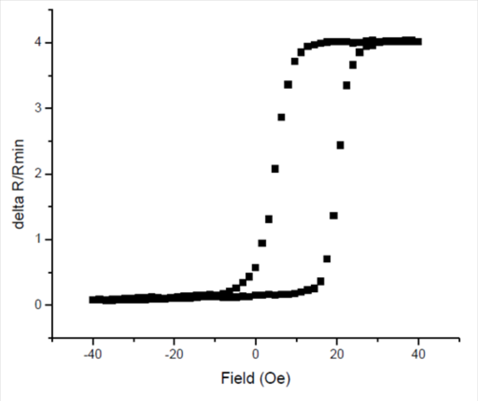

Figure 3.15: Percent change of resistance over the minimum resistance ($\Delta R/R_{min}$) with respect to applied magnetic field for the GMR thin film stack used for the development of the MP SAW devices. A 4% change of resistance was observed between the high and low resistance state of the GMR film.

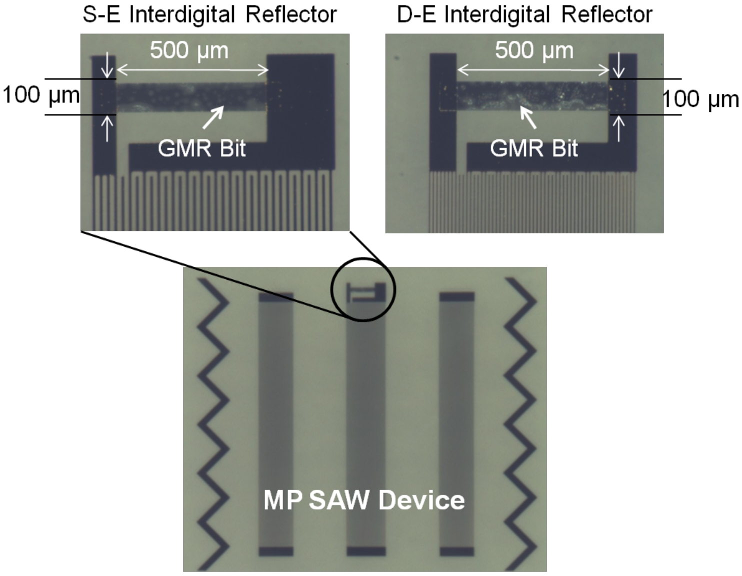

Figure 3.16: A 10x microscope images show the dimensions and location of an integrated GMR bit between the terminals of an interdigital reflector.

Chapter 4 – Fabrication and Measurement Techniques

Chapter 4 provides a description of the fabrication processes and techniques used in this research. SAW delay lines and MP SAW devices were fabricated at two facilities using different designs and fabrication processes. The cleanrooms and laboratories at Oregon State University (OSU) and the U.S. Army Research Laboratories (ARL) were used to design the devices as well as develop process flows to fabricated the devices. The fabrication process flow is detailed in this chapter as well as a description of the experimental setup used to measure the device characteristics.

4.1 Fabrication Processes

MP SAW devices are fabricated using standard semiconductor fabrication techniques for integrated circuits. Specifically, metal deposition by evaporation and sputtering, photolithographic patterning, dry etching, and lift-off techniques were used in the fabrication of the devices.

4.1.1 Material Deposition Techniques

Physical vapor deposition (PVD) techniques were used to deposit metal layers on the piezoelectric substrate for fabricating the interdigital transducers and the GMR bits. Three PVD techniques were used including thermal evaporation, electron-beam evaporation, and sputter deposition. Thermal evaporation was used at OSU to fabricate aluminum IDTs. Electron-beam evaporation was used at ARL to deposit chromium/gold IDTs. Sputter deposition was used at NVE Corporation and the National Institute of Standards and Technology to deposit the GMR thin film stacks.

Thermal and electron-beam evaporation deposit metals (typically with relatively low melting temperatures) by thermally heating and evaporating the material. The evaporated metal then recondenses on the target substrate suspended above the heated source material. For thermal evaporation, the source material is placed in direct contact with a conductive filament or boat (typically made of tungsten with the highest melting temperature of any pure metal at 3,422°C), which is heated by passing a large current through the filament. For electron-beam evaporation, a highly energetic beam of electrons is used to heat and evaporate the source material, which is typically placed in a graphite crucible (graphite has a melting temperature of 3,675°C). Both evaporation methods take place under vacuum with a pressure of $1\text{x}10^{-5}$ Torr or less. Figure 4.1 provides illustrations for thermal and electron-beam deposition. The deposition rate can be observed through the use of a quartz crystal monitor. As the quartz crystal is covered in deposited material, the resonant frequency of the crystal shifts based on the thickness of the deposited film. The deposition rate for electron-beam deposition is G (with units cm/s) when using a small point source and can be calculated using equation 4.1.1 [61]:

$$G = \frac{m}{\pi \rho r^2} \cos(\phi) \cos(\theta) \tag{4.1.1}$$

where m is the mass evaporation rate with units of g/s. ρ is the material density with units of g/cm^3. r is the distance between the source and the substrate with units of cm. ϕ is the angle measured from the normal to the plane of the source to the location of the substrate and is measured in degrees. θ is the angle measured from the normal to the plane of the substrate to the location of the source and is also measured in degrees.

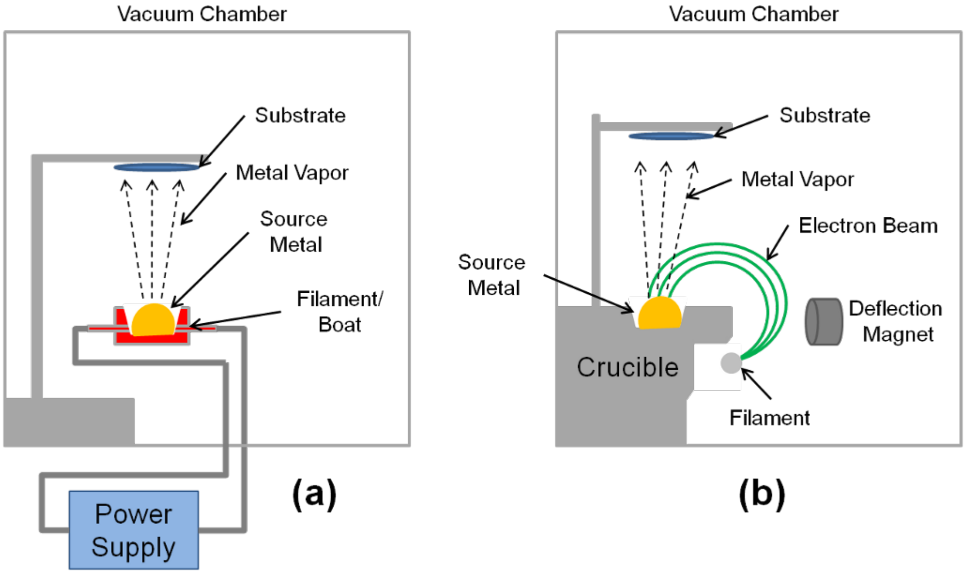

Figure 4.1: An illustration of the thermal evaporation process is shown in (a), and an illustration of the electron-beam evaporation process is shown in (b). In both cases, a source material (typically with a melting point of less than 1200°C) is heated to the point of evaporation. A substrate is placed some distance above the source and the material condenses on the substrate, depositing a thin film.

Sputtering uses highly energetic ions to strike a solid target, subsequently ejecting atoms from the target in the gas phase that then deposit on a substrate. The large ions, such as Ar^+, are typically used and generated in a plasma glow-discharge. These ions are accelerated towards a material target through the use of a large electrical potential difference between the target and the substrate. For material targets that are electrically conductive, a direct current (DC) power supply is used to create the large electrical potential used to accelerate the ions to the target, with the target itself acting as the cathode. For material targets that are electrically insulated, a radio frequency (RF) power supply is used to sustain a negative charge on the surface of the target so that positive ions continuously impinge upon the surface, ejecting atoms from the surface of the target [61, 62]. The ejected atoms deposit on the surface of the substrate and accumulate, creating a thin film. A custom sputter tool was used to deposit multiple materials in an 8-layer GMR thin film stack. This deposition process was performed at the National Institute of Standards and Technology in Boulder, CO.

4.1.2 Photolithography Techniques

Photolithography is a process that is used to create micro- and nano-scale patterns on substrates and thin films. A mask is used to transfer a pattern onto a light-sensitive, organic polymer called photoresist, which is typically deposited and spun onto the substrate or thin film that is to be patterned. There are two types of photoresist: positive and negative photoresist. When exposed to ultraviolet (UV) light, positive photoresist becomes highly soluble to certain organic solvents (developer solutions) while negative photoresist becomes increasingly insoluble. When using a mask pattern designed for a positive photoresist, an inverse image of the pattern is achieved if negative photoresist is used. A schematic of the pattern transfer differences between positive and negative resist is shown in Figure 4.2.

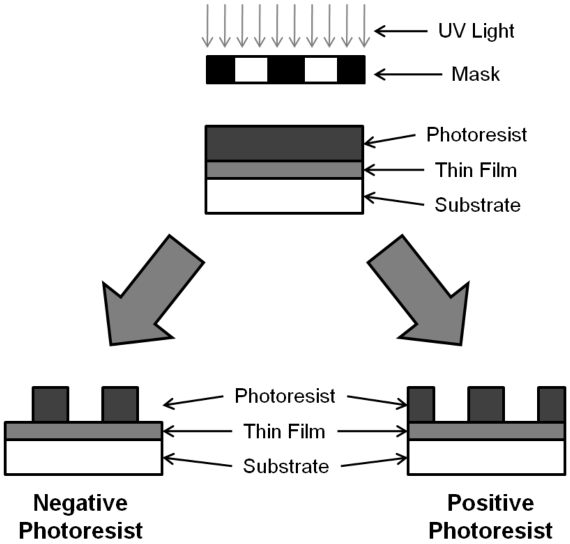

Figure 4.2: Photolithographic patterning of two types of photoresist using UV light source and a contact mask. Positive photoresist and negative photoresist create inverse patterns when the same mask is used.

Liquid photoresist is first spun onto the substrate and then lightly baked to remove solvents (ethyl lactate and ethyl pyruvate are commonly used in photoresist) and to convert the photoresist into a film. A mask is placed over the photoresist-coated substrate and then exposed to UV light. The mask pattern is transferred to the photoresist through the use of a developer solution, which washes away the more soluble photoresist (photoresist exposed to the UV light for positive resist, and photoresist not exposed to the UV light for negative resist). A deionized water rinse is typically performed to remove any developer residue. At this point, the pattern has been transferred to the photoresist. There are two typical methods for transferring the pattern in the photoresist to the underlying substrate or thin film: etching and lift-off. These two substrate/film patterning techniques will be discussed in the following sections of this thesis. After the pattern has been transferred from the photoresist into the substrate or thin film, the photoresist is then removed using solvents such as acetone or Baker PRS 3000 (brand of commercial photoresist stripper) and sometimes with the assistance of ultrasonic energy.

4.1.3 Etching Techniques

Etching is one of the two primary techniques used for film patterning once a photoresist layer is placed on top of a thin film or substrate. A typical process flow for etching is depicted in Figure 4.3. It involves the removal of the thin film or substrate in areas that are not protected by the patterned photoresist layer. There are two primary types of etching: wet etching and dry etching. Wet etching (also referred to as chemical etching) involves the use of a solution that removes the target thin film or substrate through chemical reaction. Wet etching tends to have a high selectivity due to the specificity of the etchant chemistries used, and is capable of removing one layer without affecting the layer below. Wet etching is typically used for etching across large-areas, but the isotropic nature typically limits how small the critical dimension can be. Dry etching (also referred to as physical etching or ion milling) involves the use of ion bombardment to physically dislodge atoms from a surface. Large ions such as Ar^+ are accelerated through a very large potential and collide into a substrate at high velocity. Dry etching is an anisotropic process and is able to create very high aspect ratio structures with very small critical dimensions, but lacks the selectivity of wet etching.

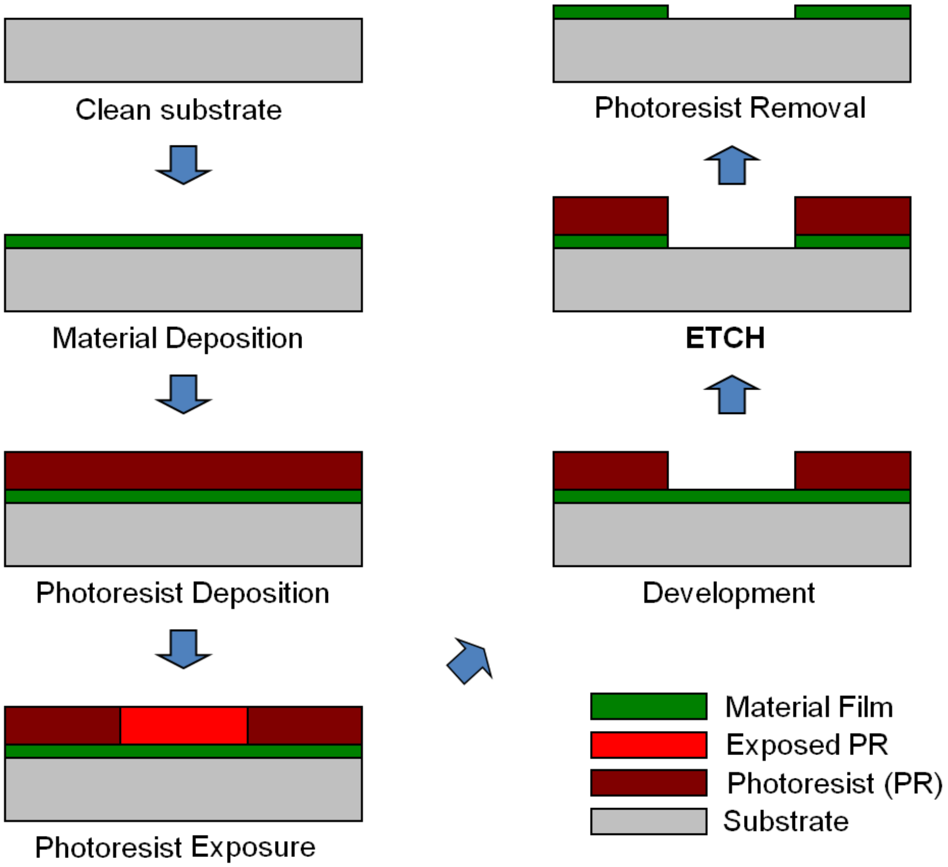

Figure 4.3: Typical process flow for an etching process.

4.1.4 Lift-Off Techniques

Lift-off processing is typically used when etching is not feasible (e.g., creating a via through a multilayer stack of dissimilar materials), and involves masking off areas on a substrate to control where a deposited material is allowed to be. Figure 4.4 details a typical process flow for the lift-off process. Photoresist is deposited, spun on, and patterned (using the photolithography process described in section 4.1.2) before the deposition of the material film to be patterned. The photoresist pattern associated with lift-off is the inverse of the pattern associated with etching. In the lift-off process, material is deposited on areas not covered in photoresist, while in the etching process, material is removed in areas not covered in photoresist. The protective photoresist mask and the unwanted deposited material are stripped off the substrate by submersing the substrate in an organic solvent such as acetone, Nano Remover PG and Baker PRS 3000. For this process to work, the photoresist masking the substrate must be at least twice as thick as the deposited material layer to allow for enough photoresist exposure to the stripping solution. Due to the fact that photoresist is put down as a masking layer before the material deposition, deposition process temperatures must be kept below the hardening temperature of the photoresist. If surpassed, the photoresist will lose its solvency and will not be removable.

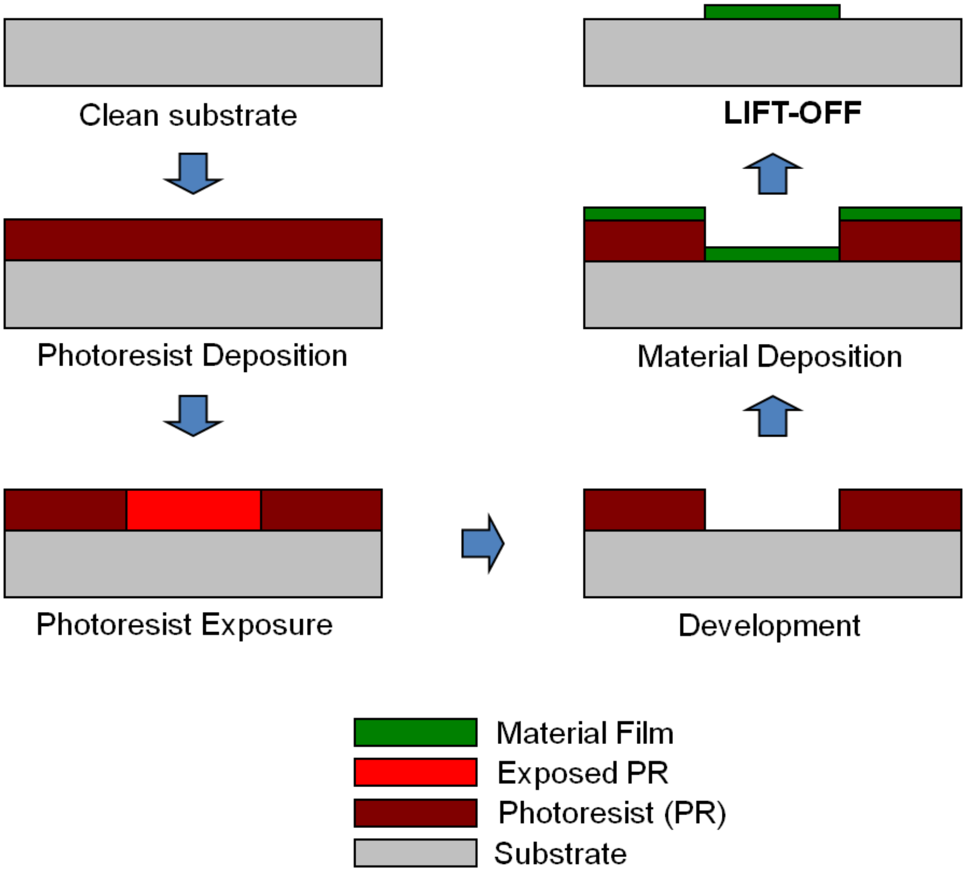

Figure 4.4: Typical process flow for lift-off.

4.2 SAW Device Process Flows

MP SAW device fabrication was attempted at two facilities with two different process flows based on the materials, equipment, and cleanroom facilities available at each location. The first attempts to produce devices were performed in the Solid State Device Laboratory at Oregon State University. Issues with processing GMR thin film stacks resulted in the need to change materials and processes. The opportunity to make use of the cleanroom, materials, and facilities at the U.S.

Army Research Laboratories allowed for a different set of fabrication processes to be attempted. With the help of the National Institute of Standards and Technology, functional MP SAW devices were produced.

4.2.1 Oregon State University Process Flow

MP SAW devices were fabricated from a 100 mm-diameter Y-Z lithium niobate wafer diced into 2.54 cm x 2.54 cm coupons. The lithium niobate wafer came with a blanket-deposited GMR thin film stack fabricated by NVE Corporation. 100 µm x 500 µm GMR bits were patterned and fabricated between the two terminals of the interdigital reflectors. The IDTs and interdigital reflectors were fabricated out of aluminum with an electrical period of 144 µm. For the single-electrode designs, the electrode and spacing widths were 36 µm each, and the aperture width was set to 1 cm. The electrode and spacing widths for the double-electrode designs were each 18 µm with the aperture width set to 1 cm. Table 3.3 provides the list of geometry parameters used for the OSU designs. Physical dimensions are defined in Figure 2.4.

4.2.1.1 Process Flow Description

MP SAW devices are two-layer devices. For the OSU-fabricated devices, the first layer is for the GMR bits patterned from the GMR film stack deposited by NVE Corporation. The second layer is for the IDTs patterned from a blanket Al deposition. Alignment between the two layers is required to ensure that the GMR bit is placed in between the terminals of the interdigital reflector between the two transmit/receive IDTs. Figure 4.5 shows the process steps taken to fabricate the devices described above.

A 2.54 cm x 2.54 cm lithium niobate substrate with a blanket NVE GMR film stack was rinsed in acetone, isopropyl alcohol and water, and then dried in preparation for patterning. The GMR bit was patterned using photolithography and dry etching. A 5 µm layer of SU-8 negative photoresist and a 700 nm adhesion pre-treatment (Omnicoat solution) were patterned using a Karl Suss MJB3 photoaligner tool and a Microposit 351 developer solution. A reactive ion etching tool was used in the Ar^+ ion milling mode to transfer the pattern into the NVE GMR blanket layer, with the 3-5 µm thick photoresist masking off desired areas. Upon completion of the dry etch, the masking photoresist was stripped off using the SU-8 stripping solvent, leaving patterned GMR bits on the lithium niobate substrate.

Aluminum IDTs were added as the second layer to provide transduction and reflector structures to the SAW device. The IDTs were photolithographically patterned using a 1.8 µm thick layer of Shipley 1818 positive photoresist and a dark field mask. Alignment marks were used to ensure that the GMR bit was placed correctly in between the terminals of the IDT reflector stucture. The photoresist was developed, leaving the exposed areas where the aluminum electrodes were to be placed. A blanket film of aluminum approximately 500 nm thick was deposited on top of the patterned GMR bits/ lithium niobate substrate, leaving alignment marks exposed on the edges of the substrate for aligning the IDT structures with the GMR bits. After the deposition, the substrate was submersed in acetone for 6 hours to dissolve the photoresist mask and remove the unwanted aluminum. An ultrasonic bath was used for 2 minutes to assist in the removal of any remaining photoresist. The device-in-process was then rinsed with acetone, isopropyl alcohol and deionized water before being dried with nitrogen gas. Figure 4.6 shows the aluminum IDT reflector structure aligned and fabricated on top of a GMR bit. After the aluminum IDTs and reflector structure were fabricated, the lithium niobate substrate was then mounted on a PCB fixture with the IDT terminals wirebonded to SMA connectors. The MP SAW device and fixture is depicted in Figure 4.7. Additional details of this process flow are provided in Appendix A.

4.2.1.2 Fabrication Results

The fabrication process flow described in Section 4.2.1.1 was the result of multiple iterations and attempts to create a viable process flow for fabricating a MP SAW device. Both wet etch patterning and dry etch patterning of NVE GMR film stack were attempted. Issues with the lack of selective etching between layers and the under-cutting of certain layers limited the effectiveness of the wet etching techniques for the GMR thin film stack. Various etch recipes were developed to etch through all 7 layers of the GMR stack without overetching any one individual layer in the stack — but none were able to consistently do so.

Dry etch problems also arose with the argon ions punching through the photoresist protective mask, and damaging the GMR material underneath, but were overcome with a change in the type of photoresist used as the protective masking layer. Originally, the thinner, softer Shipley 1818 positive photoresist with a nominal thickness of 1.8 µm was used, but it was found to be unable to stop the Ar^+ ions from penetrating the top layers of the GMR film underneath the masking photoresist. To rectify this problem, thicker and harder photoresist (SU-8 negative photoresist) was used, with a nominal thickness of 3-5 µm. This photoresist was able to better withstand the ion bombardment during the dry etch process, but removing the SU-8 photoresist required mechanical force that could damage the GMR bit. Additionally, the Ar^+ ion bombardment roughens the substrate surface, which in turn, degrades SAW propagation.

Due to the limited achievable resolution with mylar masks, IDTs, with feature sizes greater than 10 µm, were designed. The photoresist recipes developed for this process could not produce 12 µm features with any yield. Due to the number of electrodes, shorting between the two electrode terminals was a predominant flaw with all the devices fabricated with this process flow. The combination of problems with both the GMR patterning and the IDT patterning meant low yields and poor device performance. Only 2 out of 9 devices were fabricated without any major defect, and proved, in the end, to be an ineffective process flow.

4.2.2 US Army Research Laboratories Process Flow

Blank 76 mm-diameter Y-Z lithium niobate wafers were used to produce multiple SAW devices per wafer. After fabrication, the lithium niobate wafers were diced into 9 mm x 9 mm squares to separate the devices from each other. Fabrication was performed at the U.S. Army Research Laboratory facilities (Adelphi, MD) for device patterning, and at NIST (Boulder, CO) for the GMR film deposition. For the MP SAW devices, a 500 µm x 100 µm GMR bit was patterned between the interdigital reflector terminals. The interdigital reflector and two IDTs located on either side of the reflector were fabricated out of a 10 nm Cr layer (for adhesion) and a 300 nm Au layer. The electrical period of the IDT structures was 48 µm, with an aperture width of 5 mm. The single-electrode designs were fabricated with a 12 µm electrode width and spacing width. The double-electrode designs were fabricated with a 6 µm electrode width and spacing width. The parameters for the S-E and D-E designs fabricated at ARL are given in Table 3.3. Figure 4.8 provides a magnified view of a single-electrode SAW device (a) and of a double-electrode SAW device (b).

4.2.2.1 Fabrication Description

Two photolithography steps were required to fabricate the devices: one for patterning the GMR bits and one for patterning the IDTs and reflectors. Photolithography was performed using AZ5214 resist (capable of being both a positive or negative photoresist depending on the UV exposure) and a MA-6 Carl Suss photoaligner/exposure tool. The lift-off process was used for patterning the GMR bits. 76 mm-diameter lithium niobate wafers with a 2.2 µm thick film of patterned photoresist was shipped to NIST in Boulder, CO. A GMR thin film stack with a combined layer thickness of 31 nm was sputtered on in a 79.58 kA/m (1 kOe) magnetic field. The GMR stack composition is shown in Figure 2.8. The wafers were shipped back and then submersed in a heated Baker PRS 3000 bath to remove the photoresist mask and the unwanted GMR material. An acetone/isopropyl alcohol/demineralize water rinse was performed to clean the wafers, leaving only the patterned 500 µm x 100 µm GMR bits.

The second photolithography step was performed to create a photoresist mask for patterning the IDT structures. A 2.2 µm AZ5214 resist layer was aligned and exposed with a MA-6 Carl Suss photoaligner tool for lift-off. 10 nm of Cr and 300 nm of Au was blanket-deposited on top of the photoresist using e-beam deposition. The wafer was then submersed in a heated Baker PRS 3000 bath to lift off and remove the photoresist and unwanted Cr/Au metal, leaving the patterned IDTs and interdigital reflectors. The wafer was cleaned afterwards using an acetone/isopropyl alcohol/demineralized water rinse, and a 5-minute, 200W, oxygen plasma descumming process. An illustration of the process flow is depicted in Figure 4.9 and the details of this process flow are described in Appendix B. After the GMR bits and the aligned IDT structures were fabricated, the lithium niobate wafer was diced into individual SAW devices and then wirebonded into a dual in-line package (DIP) for use in a DIP socket fixture. Figure 4.10 depicts a completed SAW device fabricated with the ARL-based process flow and wirebonded into a DIP.

4.2.2.2 Fabrication Results

The process flow used at ARL overcame many of the difficulties encountered with the process flow at OSU. The GMR film stack was patterned using a lift-off process rather than an etch process, removing the issues of over-etching, layer damage from ion bombardment and damage to the lithium niobate wafer surface. The IDT structures were patterned using a glass/chrome mask with recipes that were finely tuned for lithium niobate substrates and the AZ-5214 photoresist used in photolithography. This allowed the critical dimension on the single-electrode IDT design to be reduced from 36 µm on the OSU process flow to 12 µm on the ARL process flow. The reduction in area allowed for additional devices to be made on the same wafer surface area (the smaller dimensions also made the SAW devices compatible with the DIPs available at ARL), and increased the operating frequency of the devices. Due to better-developed lithography and lift-off processes, the devices fabricated on the ARL process flow fit on a 9 mm x 9 mm coupon (compared to the 12 mm x 20 mm coupon needed for devices fabricated with the OSU process flow) with a calculated center frequency of 72.67 MHz (using equation 2.2.8). Yield for single-electrode devices approached 80%, while yield for double-electrode devices were approximately 40%. Nearly all damaged devices were caused by shorting issues between the two terminals of the IDT structures.

4.3 Measurement Techniques and Characterization

Reflection scattering parameters (S_{11}) were measured from the MP SAW devices to determine the change in response as a function of the GMR bit resistance load across the interdigital reflector. All measurements were performed on ARL-fabricated devices due to the number of functional devices available for measurement. An applied magnetic field along the easy axis of the GMR bit was used to switch the resistance state of the GMR bit. An experimental setup was constructed to measure the reflection response of an MP SAW device as a magnetic field range was swept.

4.3.1 Experimental Setup

The experimental setup used to conduct frequency-domain reflection measurements is pictured as a block diagram in Figure 4.11. The SAW device-under-test (DUT) was placed in a DIP socket fixture that connects the IDT terminals to an Agilent E5071C network analyzer via SMA connectors. The fixture and the DUT was placed inside a set Helmholtz coils of 0.5 mm-thick x 12.7 mm-wide copper strips with 70 turns per coil and an inner diameter of 12.7 cm. The Helmholtz coils were used to generate a magnetic field powered by a Keithley 2440 power supply. The magnetic field strength of the solenoid was monitored by a Lakeshore 450 gaussmeter. The Agilent E5071C network analyzer, Keithley 2440 power supply, and the Lakeshore 450 gaussmeter were all controlled by a computer running National Instrument's LabVIEW software. Figure 4.12 provides a screenshot of the graphical user interface for the program, and the block diagrams of the program are provided in Appendix C.

4.3.2 Measurements

The S_{11} parameter was measured for the SAW devices to determine the magnitude of the reflection responses with respect to the SAW frequency. S-parameters describe how RF signals propagate through a multi-port network. Typically, S-parameters are presented as complex (amplitude and phase) one- and two-port parameters that make use of traveling waves to describe the scattering of the wave at each port (reflection and transmission). An Agilent E5071C network analyzer was used to take the measurements. Multiple settings were taken into consideration when configuring the network analyzer. Some of the most cricitical settings that can be controlled by the user of the network analyzer include: start and stop frequency, intermediate frequency bandwidth, averaging, smoothing, time gating, data points, calibration correction, and data formats.

- The start and stop frequencies specify the frequency range for which the devices are measured and swept at. Typically, the frequency range is centered around the calculated center frequency of the SAW device being measured.
- The intermediate frequency (IF) bandwidth adjusts the frequency resolution on the network analyzer, with a narrower IF bandwidth enabling smaller signals to be seen (improved ability to extract signal components that are close together in frequency) reducing noise levels while decreasing the scan

rate.

- Trace-to-trace averaging is used to reduce noise in the data by taking the same measurement multiple times. Averaging defined by the network analyzer equally weights the contributions for each trace sweep and increases the overall accuracy of the measurement. Averaging was used for the majority of the measurements taken. Typically, six (6) samples were taken at each data point and averaged together in attempts to remove error caused by thermal drift.

- Smoothing (box-car or adjacent-point averaging) is performed by averaging neighboring data points together from the same trace sweep, and is used to reduce noise in a measurement. Smoothing reduces the accuracy and distorts the overall measurement in exchange.

- Time gating is used to remove signal contributions from reflections, transmissions and noise during periods of time that are not of interest. This is useful for the the measurements performed in this research since the propagation times for the acoustic waves between the IDTs and the interdigital reflectors are well-known. For the experiments performed, the gated time period was centered around the time it took for an acoustic wave to make a round trip between the center of the transmitting IDT and the center of the reflector.

- Data points refer to the number of individual measurements taken over the span of the frequency range defined by the start and stop frequencies. Plots with higher resolution require more data points to be taken.

- Calibration correction enables the response of cables, connectors, and fixtures to be eliminated from the measurement, so that the signal can be attributed to the DUT only. An open-circuited, short-circuited and a throughput calibration DIP were made to perform a SOT (short, open, thru) calibration on the Agilent E5071C network analyzer.
- S-parameters can be viewed in different formats or different components. The reflection S-parameter, S_{11}, was measured in a linear magnitude format with arbitrary units.

Specific values of the network analzyer parameters are included in Chapter 5 for each set of experiments.

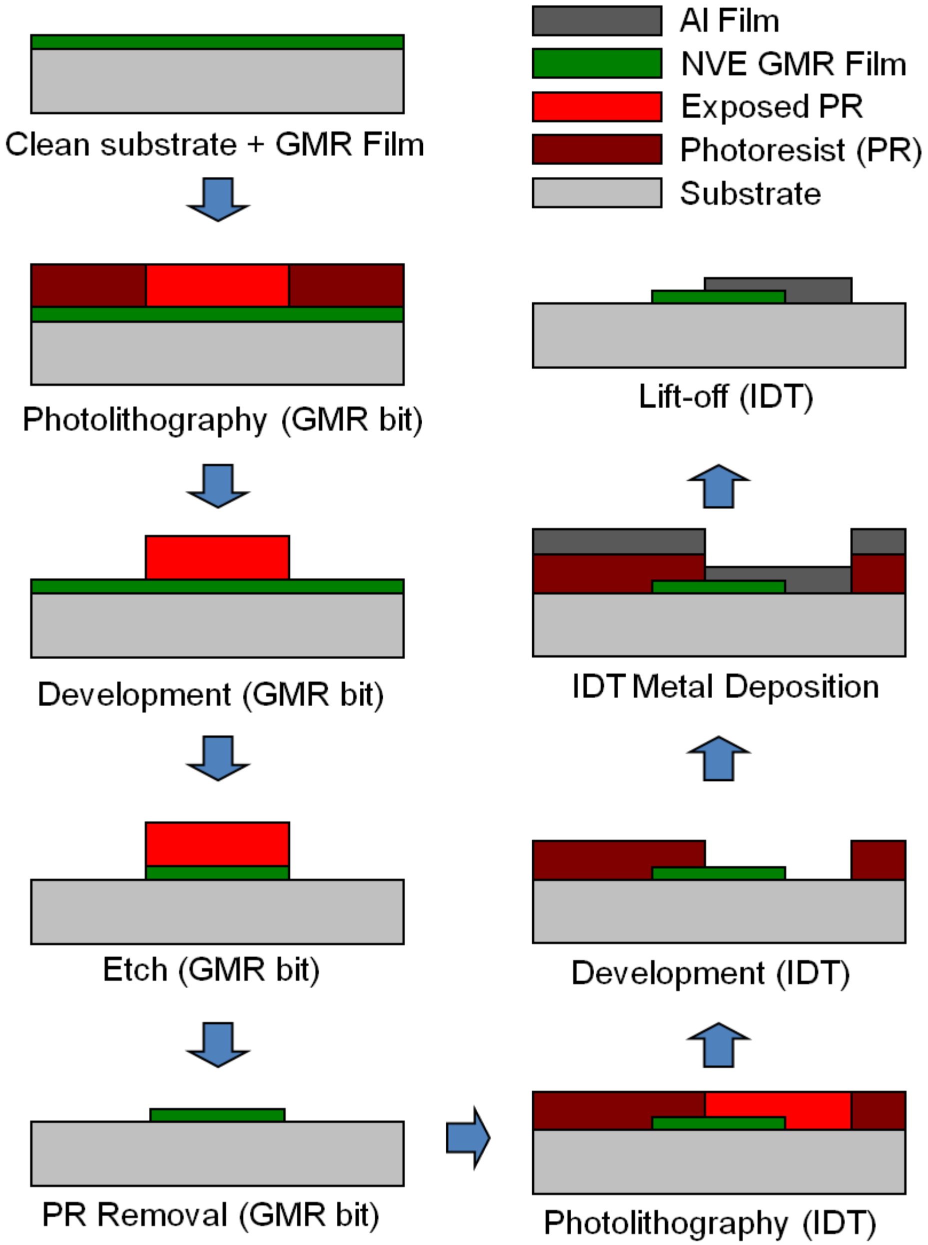

Figure 4.5: Process flow diagram used to fabricated MP SAW devices at Oregon State University.

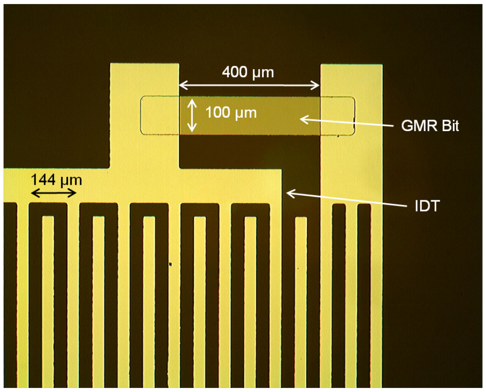

Figure 4.6: A fabricated GMR bit aligned between the two terminals of an interdigital reflector on a MP SAW device is shown at 5x magnification on an optical microscope.

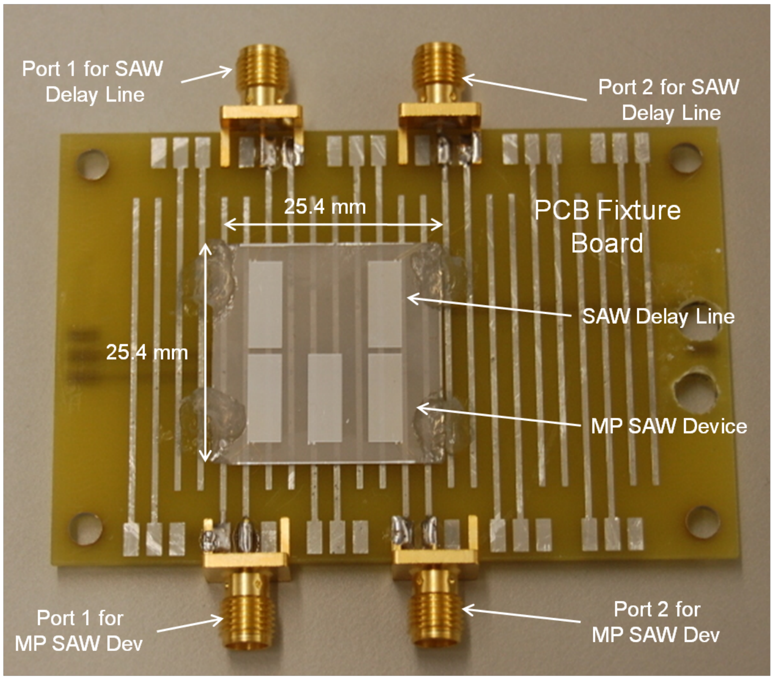

Figure 4.7: Image of two SAW devices on one substrate (reference SAW delay line on top, and an MP SAW device on the bottom) glued into a PCB fixture, with the terminals of the IDTs wirebonded to SMA connectors.

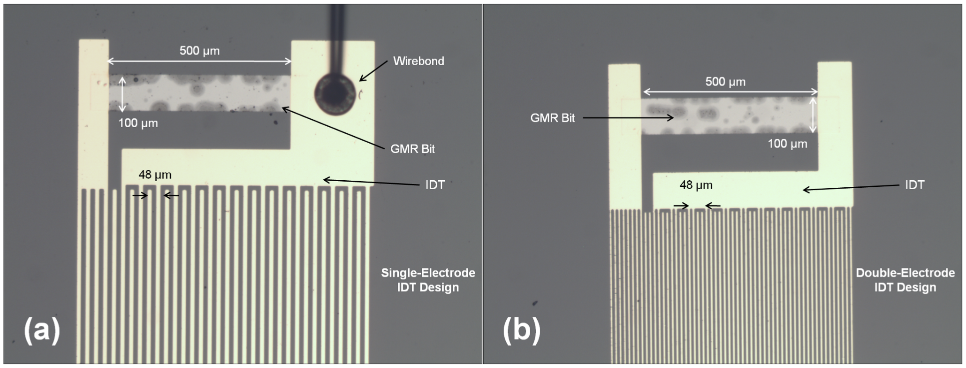

Figure 4.8: (a) GMR bit on a single-electrode MP SAW device fabricated with the ARL process (5x magnification). (b) GMR bit on a double-electrode MP SAW device fabricated owiththe ARL process (5x magnification).

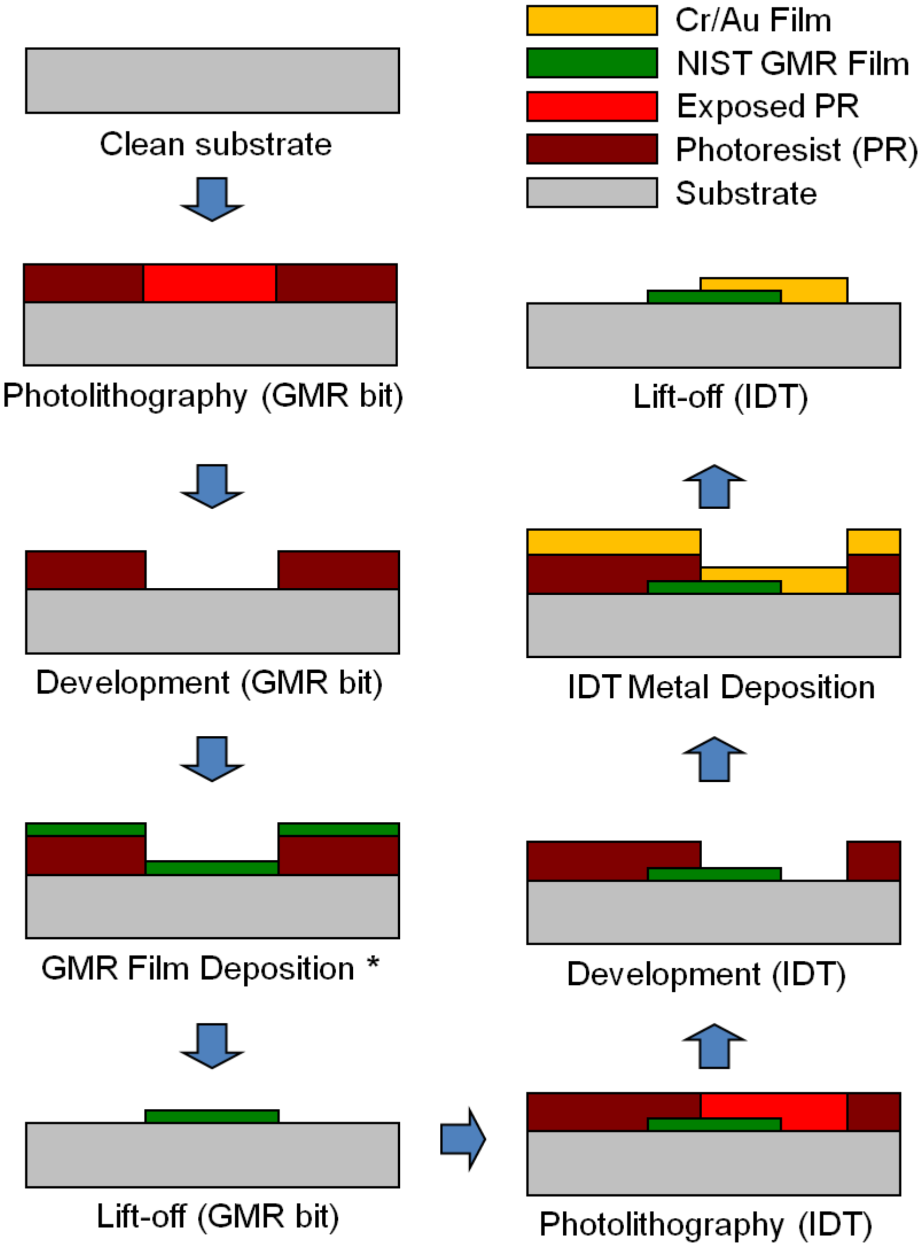

Figure 4.9: Illustration of the process flow used to fabricate MP SAW devices at the U.S. Army Research Laboratories. * GMR Film Deposition was performed by sputter deposition at the National Institute of Standards and Technology, Boulder, CO.

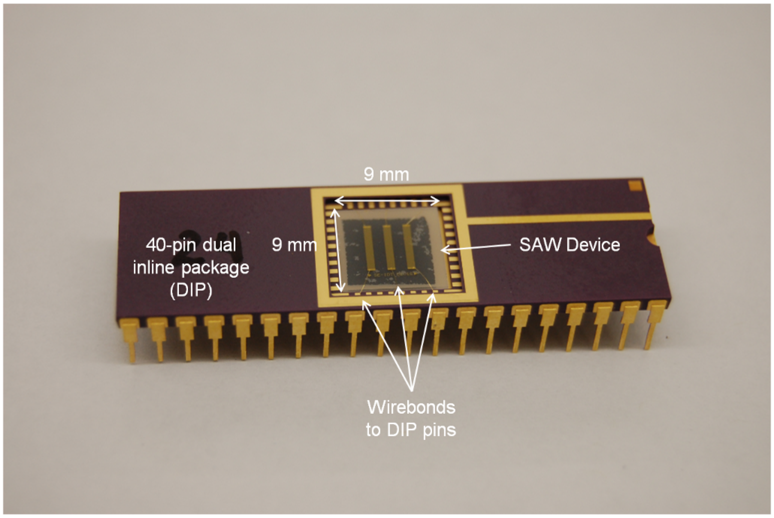

Figure 4.10: An example of an ARL-fabricated MP SAW device that has been wirebonded into a dual-inline package.

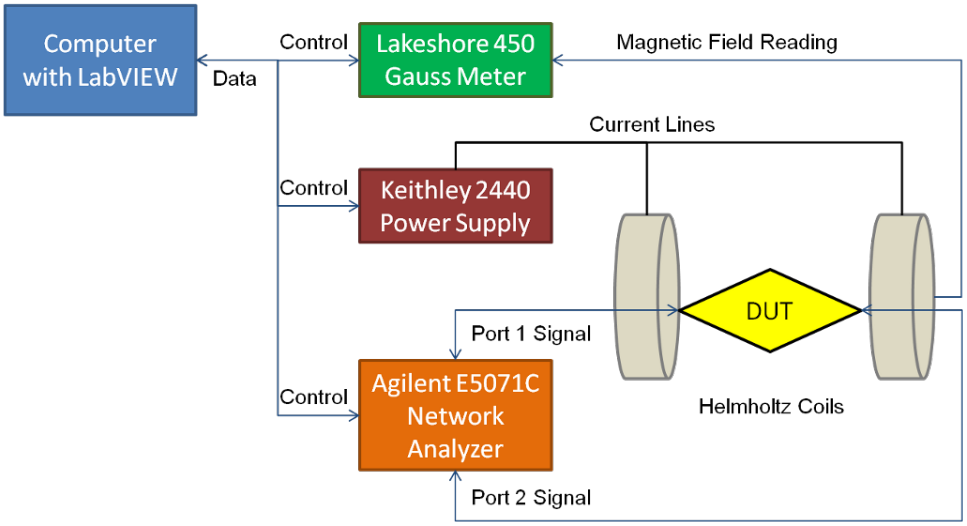

Figure 4.11: Block diagram of the experimental setup used to measure reflection S-parameters. The setup allows a varying magnetic field to be affected across the MP SAW device under test, and the entire system is controlled via a LabVIEW program on a GPIB-connected computer system. The field is controlled by changing the current in the solenoid.

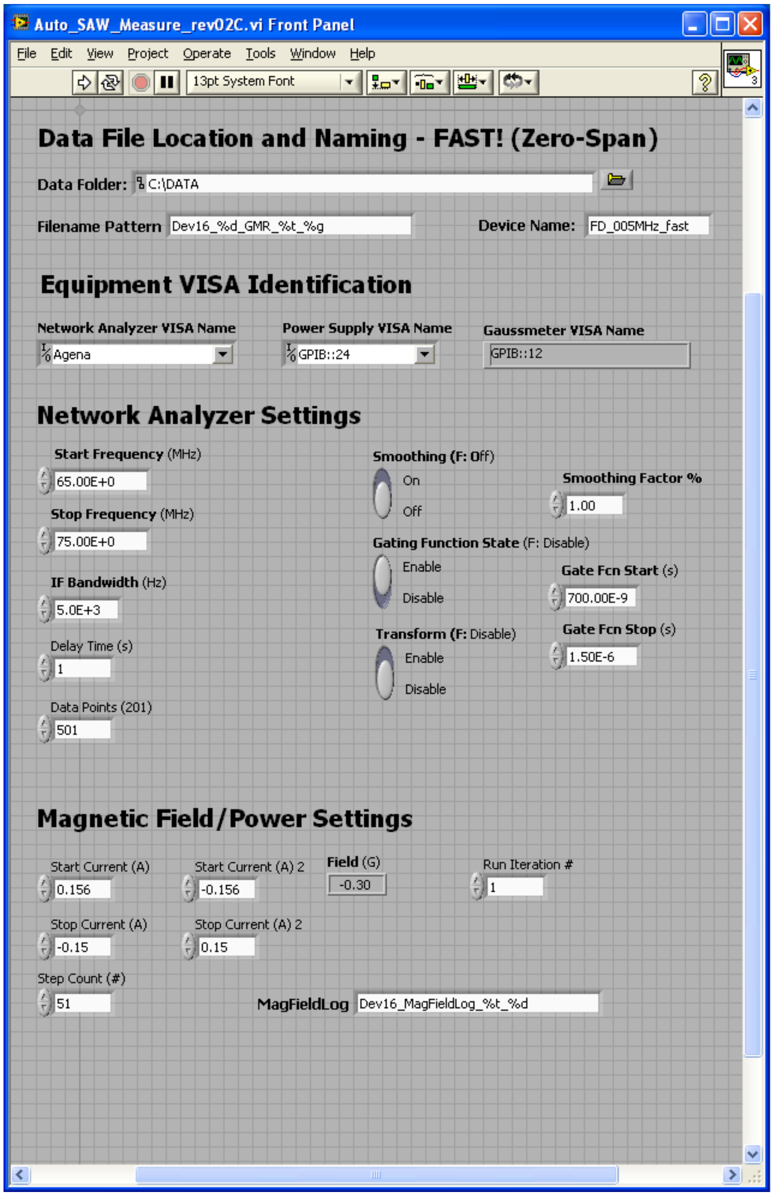

Data File Location and Naming - FAST! (Zero-Span)

Data Folder: C:\DATA

Filename Pattern: Dev16_%d_GMR_%t_%g

Device Name: FD_005MHz_fast

Equipment VISA Identification

Network Analyzer VISA Name: Agena

Power Supply VISA Name: GPIB::24

Gaussmeter VISA Name: GPIB::12

Network Analyzer Settings

Start Frequency (MHz): 65.00E+0

Stop Frequency (MHz): 75.00E+0

IF Bandwidth (Hz): 5.0E+3

Delay Time (s): 1

Data Points (201): 501

Smoothing (F: Off): On / Off

Smoothing Factor %: 1.00

Gating Function State (F: Disable): Enable / Disable

Gate Fcn Start (s): 700.00E-9

Transform (F: Disable): Enable / Disable

Gate Fcn Stop (s): 1.50E-6

Magnetic Field/Power Settings

Start Current (A): 0.156

Start Current (A) 2: -0.156

Field (G): -0.30

Run Iteration #: 1

Stop Current (A): -0.15

Stop Current (A) 2: 0.15

Step Count (#): 51

MagFieldLog: Dev16_MagFieldLog_%t_%d

Figure 4.12: Graphical user interface for the LabVIEW program that automates measurements.

Chapter 5 – Results and Discussion

Chapter 5 discusses four sets of experiments performed to provide proof-of-concept results of a GMR element across the terminals of an IDT reflector changing the reflection response of the SAW device. Measurements were taken using the experimental setup described in Section 4.3.

5.1 SAW Device Response with respect to Reflector Design

The reflection parameters (S_{11}) were measured from four different reflector designs shown in Figure 5.1. An open and shorted single-electrode (referred to as S-E from this point forward) reflector, shown in Figure 5.1 (a) and (b) respectively, were placed in S-E SAW delay lines. An open and shorted double-electrode (referred to as D-E from this point forward) reflector, shown in Figure 5.1 (c) and (d) respectively, were placed in D-E SAW delay lines. All four reflector designs were centered in the 3 mm cavity of the SAW delay lines. The dimensions of the single-electrode reflector structures and IDTs match the values given in the ARL SE column of Table 3.3. The D-E reflectors and IDTs were based on dimensions given in the ARL DE column of Table 3.3. The the two open reflector designs simulate the ideal high resistance state between the IDT terminals and provide insight into the maximum reflection response to be expected. The two shorted reflector designs represent the ideal low resistance state between IDT terminals and give the minimum reflection response output that can be expected. In addition to the four reflector designs, a set of S-E delay lines with no reflectors was measured as a control. No D-E delay lines with no reflector were available for measurement due to fabrication issues.

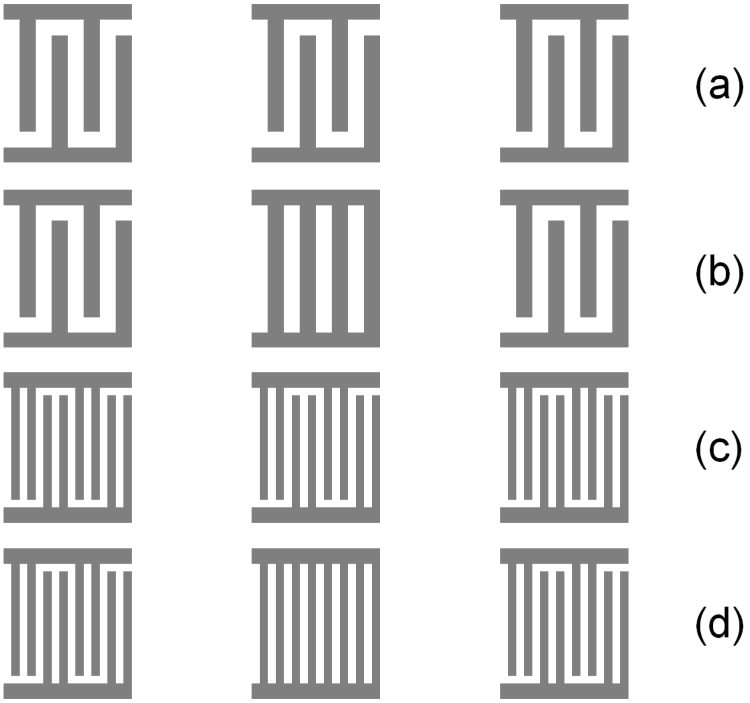

Figure 5.1: Illustrations of the four reflector device designs are shown, including (a) a single-electrode open reflector, (b) a single-electrode shorted reflector (c) a double-electrode open reflector, and (d) a double-electrode shorted reflector. The reflector structure is centered between two IDTs, allowing for both reflection and transmission measurements to be taken.

Reflection measurements were taken with an Agilent E5071C network analyzer. The network analyzer settings are detailed in Table 5.1. The four SAW device designs and the SAW delay lines were fabricated with an electrical period of 48 µm and a calculated center frequency of 72.67 MHz. The center frequency for each fabricated typically does not match perfectly with the calculated value. Potential reasons for deviations on the order of 0-2 MHz include variations in the device dimensions and distortion in the single-electrode designs due to multiple acoustic reflections within the IDTs [32]. Measurements were taken over a frequency range of 67 MHz and 74 MHz to determine the precise center frequency for each device. The linear magnitude of the reflections were reviewed, possessing units of mU, which are arbitrary units normalized to the power level internally specified by the network analyzer.

Network Analyzer Settings	**Value**
S-Parameters	S_{11}
Frequency Range	65 MHz - 75 MHz
IF Bandwidth	1 kHz
Averaging	OFF (1 sample)
Smoothing	OFF (0%)
Time Gating	700 ns - 1500 ns
Data Points	1601
Time Domain Transform	OFF
Calibration Correction	ON

Table 5.1: Network analyzer settings used for measuring the devices illustrated in Figure 5.1. Screen captures and the locations of these settings on the Agilent E5071C network analyzer can be found in Appendix D.

Five open S-E reflector SAW devices, two shorted S-E reflector devices, one open D-E reflector device, two shorted D-E reflector devices, and three S-E delay lines with no reflectors were measured. The center frequency and the magnitude of the S_{11} parameter for each device measured are displayed in Table 5.2. The center frequency, S_{11} magnitude at the center frequency, and the standard deviation at the center frequency of the averaged plot are provided in Table 5.3.

Device ID	Design *	Center Frequency (MHz)	S11 Magnitude (mU)
DEV 04	SE Open	71.89	196.40
DEV 05	SE Open	72.15	163.84
DEV 24	SE Open	71.66	207.99
DEV 25	SE Open	71.62	178.47
DEV 27	SE Open	71.84	181.56
DEV 28	SE Short	70.82	121.18
DEV 38	SE Short	70.12	69.35
DEV 35	DE Open	71.25	158.34
DEV 37	DE Short	72.53	10.39
DEV 40	DE Short	72.46	9.34

Table 5.2: Device measurements including the measured center frequency of each device, and the S_{11} magnitude at the center frequency. * Design Legend: SE Open = Single-Electrode Open Reflector Device; SE Short = Single-Electrode Shorted Reflector Device; DE Open = Double-Electrode Open Reflector Device; DE Short = Double-Electrode Shorted Reflector Device

The shorted S-E and D-E reflector SAW devices should have minimal electrical reflections compared to the open reflector devices. All S_{11} responses for the measured SAW devices are plotted in Figure 5.2. The difference in magnitude between the shorted S-E reflector device with the largest reflection response and the open S-E reflector device with the smallest reflection response is less than either the magnitude variation in either sample set and less than the two standard deviations in the case of the shorted S-E reflector device sample set. While there is evidence that the open S-E reflector structures in general, possess a higher reflection magnitude, no firm conclusions can be made from the data provided. For the D-E reflector devices a relatively large change in response exists between

Design *	SE Open	SE Short	DE Open	DE Short
Number of devices measured	5	2	1	2
Center Frequency (f_c) (MHz)	71.7875	70.4875	71.2500	72.5250
f_cVariation (MHz)	0.53125	0.69375	N/A	0.07500
S_{11} Magnitude @ f_c (mU)	184.27	86.55	158.34	9.86
S_{11} Variation @ f_c (mU)	44.15	51.83	N/A	1.05
S_{11} Standard Deviation @ f_c (mU)	18.10	37.37	N/A	0.75

Table 5.3: Averaged center frequency and S_{11} magnitude data for each of the four reflector designs. Data was averaged for devices with the same design at each data point collected along the frequency range detailed in Table 5.1. It should be noted that f_c variation and S_{11} variation refers to the difference between the highest and lowest values in the sample set. * Refer to Table 5.2 for the Design Legend.

the magntitudes of the open D-E reflector device and the shorted D-E reflector device with the largest center frequency amplitude, and can be defined as $\left(S_{11}open - S_{11}shorted\right)/S_{11}shorted \approx 1,400\%$. In this case though, not enough devices were produced to come up with a standard deviation for the open D-E reflector design.

Comparing the S-E reflector design results and the D-E reflector design results, the S-E reflector devices had greater reflection magnitudes, but could not statistically confirmed. The difference between the smallest open S-E reflector device S_{11} magnitude at the center frequency and the open D-E reflector device was 5.5 mU, which is less than the both the standard deviation and the S_{11} variation associated with the open S-E reflector device sample set. The difference between S_{11} response at the center frequency for the shorted S-E reflector device with the smallest magnitude and the shorted D-E device with the largest magnitude was 168.1 mU, or $\left(S_{11}SE_{shorted} - S_{11}DE_{shorted}\right)/S_{11}DE_{shorted} \approx 1,600\%$. It should be noted that

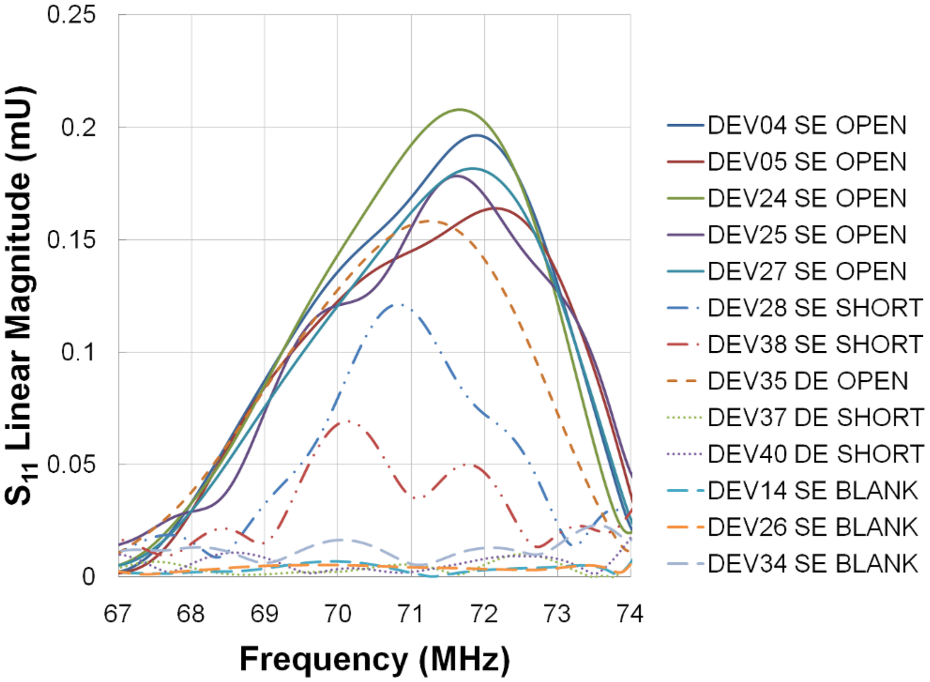

Figure 5.2: The S_{11} linear magnitude is plotted over a 7 MHz frequency range around the calculated center frequency of all measured devices.

the reflection responses from the shorted shorted D-E reflector devices were very similar to the S-E control devices with no reflector structure. This provides evidence that the shorted D-E reflectors act ideally, providing almost no reflections. The S-E reflector devices possessed larger S_{11} magnitudes when compared to their D-E reflector counterparts. This is due to the additional mechanical reflections that occur in the S-E reflectors, that contribute to the S_{11} reflections as described in Chapter 2 and Chapter 3. This additional reflection contribution could also explain why the shorted S-E reflector devices differed in S_{11} response from the shorted D-E reflector devices, which had a response similar to the control devices with no reflector present.

From the data compiled, the variation in the amplitude exhibited in each set of devices revealed that while there is indications that the open reflector designs have higher reflection magnitudes compared to the shorted reflector designs, larger sample sets are required to be able to statistically confirm this. What can be concluded from this experiment is the fact that device-to-device variation makes it difficult to compare one device directly to another, since the peak amplitude values vary (up to ~24% for open S-E reflector devices, computed using $S_{11}variation/S_{11}magnitude$ with data from Table 5.3), as well as the center frequency within the same design.

5.2 SAW Device Response with respect to Discrete Resistances

A potentiometer was used to simulate the resistance values of the GMR bit in its low and high state for the three devices measured around the calculated resistance of the GMR bit by itself without contacts, wirebonds, or fixturing. The purpose of this experiment set was to determine the viability of using a GMR bit to change the S_{11} reflection response of a SAW device depending on the resistance state of the GMR bit. A 0 Ω-to-1 $k\Omega$ potentiometer was placed between the terminals of the interdigital reflector on both a D-E and S-E SAW device as shown in Figure 5.3. The SAW devices were fabricated using the process at ARL and the dimensions of the devices are provided in Table 3.3 under the ARL SE and ARL DE columns. The S-E and D-E devices were comprised of a SAW delay line with an interdigital reflector (possessing the same design as the delay line) centered in the 3 mm cavity.

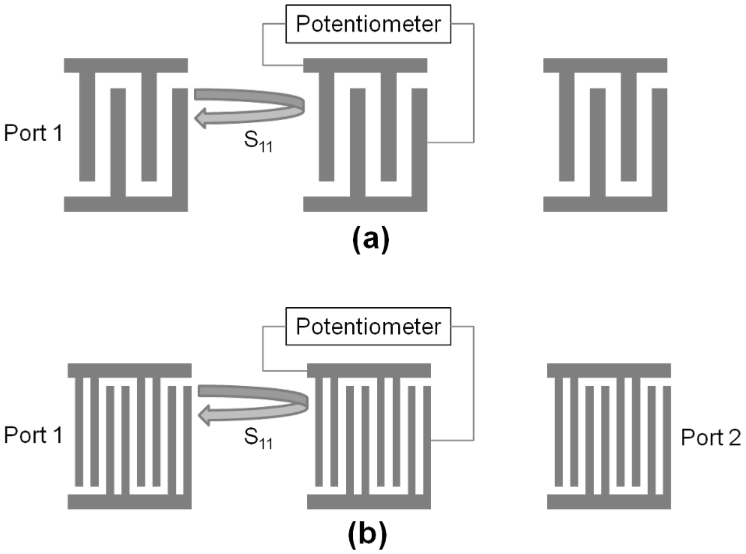

Figure 5.3: Illustration of SAW device configurations used in this set of experiments. (a) represents an open single-electrode reflector SAW device with a potentiometer between the terminals of the interdigital reflector. (b) represents the double-electrode equivalent to (a). The network analyzer port definitions are provided as well.

The calculated resistances of the GMR bits were based on the measured sheet resistance of the thin film stack, the fabricated dimensions of the bits, and the $\Delta R/R_{min}$ plot with respect to applied magnetic field along the easy axis. The calculated resistance of a 100 µm x 500 µm GMR bit is 58.35 Ω for the low resistance state and 60.60 Ω for the high resistance state. The sheet resistance, GMR bit dimensions, and the $\Delta R/R_{min}$ value were taken from Chapter 3 of this thesis. Three of the single-electrode devices had wirebonds added across the GMR bit terminals to directly measure the resistance change of the GMR bit. Table 5.4 provides the results of the measurements taken by applying a 0.1 V potential across the GMR bit and measuring current. With the resistances of the wirebonds and contacts pads included, resistance values were between 125 Ω and 170 Ω, and the changes in resistance were between 2.72 Ω and 3.36 Ω.

Device ID	High R State (Ω)	Low$R$ State (Ω)	ΔR (Ω)	$\frac{\Delta R}{R_{min}}$ (%)
DEV08	128.54	125.31	3.22	2.6
DEV13	168.92	165.56	3.36	2.0
DEV16	140.85	138.12	2.72	2.0
Calculated	58.35	60.60	2.25	3.9

Table 5.4: Measured GMR resistance results from 3 single-electrode MP SAW devices. Additional wirebonds were added to provide access to the GMR bits. The calculated resistances of the GMR bit based on the measurement data provided by the GMR thin film stack manufacturer (NIST) is also provided. Contact pad and wirebond resistances could potentially account for the differences along with variations in fabrication.

S_{11} measurements were taken from two SAW devices at their center frequencies. A single-electrode open reflector SAW device (DEV24) and a double-electrode open reflector SAW device (DEV35) were placed in a fixture (depicted in Figure 5.4) that provided electrical contact between the terminals of a potentiometer and the reflector terminals. The measurement settings used are the same as described in Table 5.1.

From theory, an increase in resistance between the two terminals of the interdigital reflector should result in an increase in S_{11} reflection magnitude returned. Figure 5.5 plots the S_{11} response at the center frequencies of the two SAW devices as well as the simulation results based on the designs of the two SAW devices tested. The simulations are detailed in Chapter 3. The data reveals that the reflection response does increase as resistance is increased between the interdigital

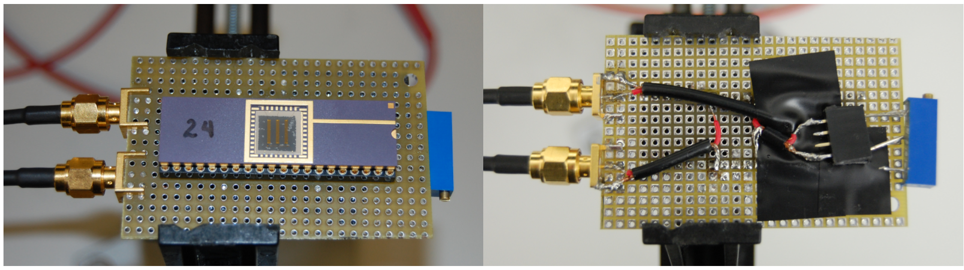

Figure 5.4: Images of the fixture used to take S-parameter measurements with a potentiometer between the reflector terminals. The reflector terminals were wirebonded to package pins, which could be accessed through the use of a DIP socket. The left picture presents the topside of the fixture while the picture on the right shows the backside of the fixture.

reflector terminals, but does so in more of a linear fashion than the simulations predicted. There is also a substantial difference in the change of the S_{11} response vs. resistance between the simulations and the actual data. The simulations predicted nearly double the amount of resistance change. The difference, while substantial, could potentially be attributed to the imperfect impedance matching of the actual devices, while the simulations assume no other impedance or parasitic contributions. Additional impedances from wirebonds, imperfect contacts, unmatched elements in the measurement setup add additional reflections that could have reduced the relative change in reflection response. Linear and logarithmic curve fittings were performed on the devices with the results provided in Table 5.5.

The data appears to have a relatively linear response between 50Ω and 170Ω where the 3 measured GMR bits and the calculated resistance values lie. The slope in this resistor range for Device 24 (S-E) was approximately 0.23%/Ω while the slope for Device 35 (D-E) was approximately 0.19%. From what can be seen from

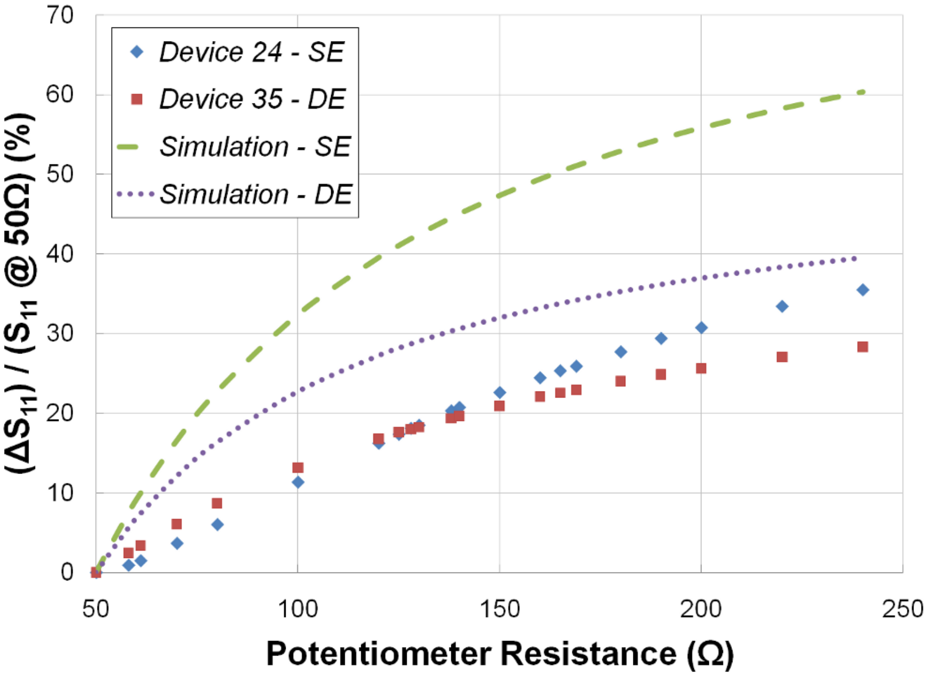

Figure 5.5: The S_{11} linear magnitude was taken at the center frequency for 21 resistances using a potentiometer. The plot normalizes the S_{11} linear magnitude to the center frequency response at 50Ω. Measurements were taken on a single-electrode SAW device (Device 24 SE) and a double-electrode SAW device (Device 35 DE).

the reflection response change as a function of potentiometer resistance it can be estimated that for the three MP SAW devices with GMR bit switching detailed in Table 5.4, a change in S_{11} response can be predicted between 0.38% and 0.77%.

Device/Simulation	Linear Fit Eqn.	Logarithmic Fit Eqn.
Device 24 (S-E)	$0.202x - 9.05$	$24.06\,ln\,(x) - 97.7$
Device 35 (D-E)	$0.152x - 3.52$	$18.64\,ln\,(x) - 72.8$
S-E Simulation	$0.312x - 3.44$	$38.92\,ln\,(x) - 148.8$
D-E Simulation	$0.200x - 0.85$	$25.19\,ln\,(x) - 95.1$

Table 5.5: Linear and logarithmic curve fitting was performed on the results from Device 24 (S-E) and Device 35 (D-E). The equations of those lines of best fit are presented along with the equations associated with the simulations performed for the S-E and D-E reflector SAW devices.

5.3 MP SAW Device Response as a function of Applied Magnetic Fields

All prior experiments were used to confirm the possibility of using a GMR bit to change the reflection response (S_{11} parameter) of an interdigital reflector structure. MP SAW devices were fabricated at ARL based on the design parameters outlined in Table 3.3 (ARL SE and ARL DE columns) using the process described in Chapter 4 and Appendix B. Unlike previous work pertaining to programmable SAW devices [15, 16, 17], the resistive element in this work is integrated, meaning that the resistive switching element is fabricated directly into the rest of the SAW device as an integral part, and uses magnetic field to switch the state of the memory element (in this case, a GMR bit). An illustration of the device is provided in Figure 5.6.

The interdigital reflector with the GMR bit act as a single-bit memory element. The single-electrode interdigital reflector with integrated GMR bit can be placed in a high or low reflection state. Correspondingly, the S_{11} signal is higher or lower.

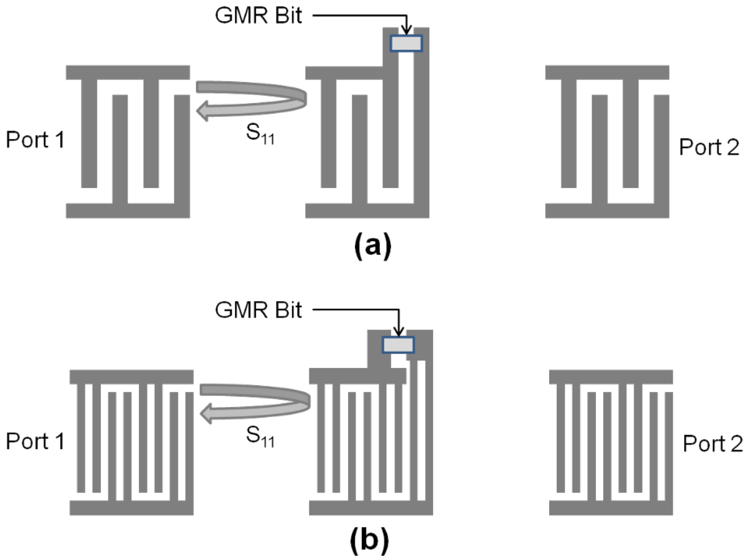

Figure 5.6: Illustration of SAW device configurations used in this set of experiments. (a) represents a single-electrode MP SAW device with an integrated GMR bit between the terminals of the interdigital reflector. (b) represents the double-electrode equivalent to (a).

The previous experiment using a discrete potentiometer in place of a GMR bit has shown that a 0.4% to 0.8% change in the S_{11} reflection response can be seen with only a 2Ω to 3Ω change in resistance (for the same resistance range as the GMR bits). Calculated and measured resistances of the GMR bits are provided in Table 5.4.

Five (5) S-E MP SAW devices and three (3) D-E MP SAW devices were measured along with control SAW devices without a GMR bit (1 S-E and 1 D-E SAW device). The control devices were used to ensure that any changes in the MP SAW device reflection response could be attributed to the change in resistance of the GMR bit and not to other environmental/mechanical factors. The setup, shown in

Figure 4.11, was used to measure the devices. The MP SAW devices were placed in an applied magnetic field aligned with the easy axis of the GMR bit, which is defined as the energetically favorable direction of magnetization. In this case, the easy axis of the GMR bit is parallel to the long dimension (the 500 µm length) due to the shape anisotropy and the magnetization direction of the pinning layer in the GMR thin film stack.

S_{11}measurements were taken while an applied magnetic field was swept between 1520 A/m (19 Oe) and -3130 A/m (-39 Oe). This applied field range was selected based on the known required field strength to switch the resistance state of the GMR bits (between 796 A/m (-10 Oe) and 1194 A/m (-15 Oe)). The swept applied field was centered around -796 A/m (-10 Oe) with approximately 2387 A/m (30 Oe) swept in both directions from this center point. The setup used to produce the magnetic field can produce a maximum field of approximately 7950 A/m (100 Oe). The measurement settings used are detailed in Table 5.6. S_{11} measurements were taken over a 10 MHz frequency range. A marker mode was used to determine the center frequency and extract the magnitude at that frequency. This was done each time the magnetic field was stepped. Figure 5.7 shows the S_{11} response normalized to each device's minimum S_{11} value as a function of the applied magnetic field, swept from a negative field to a positive field and back to the starting negative field.

From Figure 5.7, a change in the resistance state of the GMR bits can be observed between -800 A/m (~-10 Oe) and -1600 A/m (~-20 Oe). Hysteresis was present in all devices, which is to be expected, due to the presence of hysteresis in

ENA Settings	**Value**
S-Parameters	S_{11}
Frequency Scan Range	65 MHz - 75 MHz
IF Bandwidth	5 kHz
Averaging	ON (6 samples)
Smoothing	OFF (0%)
Time Gating	700 ns - 1500 ns
Data Points	122
Data Format	Linear magnitude
Marker Mode	Maximum (@ f_0)

Magnetic Field Settings	Value
Magnetic Field Range	1520A/m to -3130A/m
# of Field Steps	61 per direction
Field Sweep Direction	positive to negative to positive

Table 5.6: Network analyzer settings and magnetic field settings for MP SAW device and control SAW device measurements.

the GMR thin film as shown in Figures 3.14 and 3.15. The change in S_{11} response, hysteresis, and magnetic field strength required to change the GMR resistance varied from device to device and the numerical results are compiled in Table 5.7. The S-E and D-E control devices (open reflector SAW devices with no GMR bit) show that the change in S_{11} response is indeed due to the resistance change of the GMR bit rather than environmental or mechanical factors. The 8 MP SAW devices showed a change in S_{11} response between 0.27% and 0.90%, which was within expectations. Table 5.8 provides the averages and variation within the sample set measured.

The data supports the predicted percent change in S_{11} response based on the resistance change expected from the GMR bits (2 Ω to 3 Ω change with a base resistance value between 50 Ω and 170 Ω). From the data collected collected in the

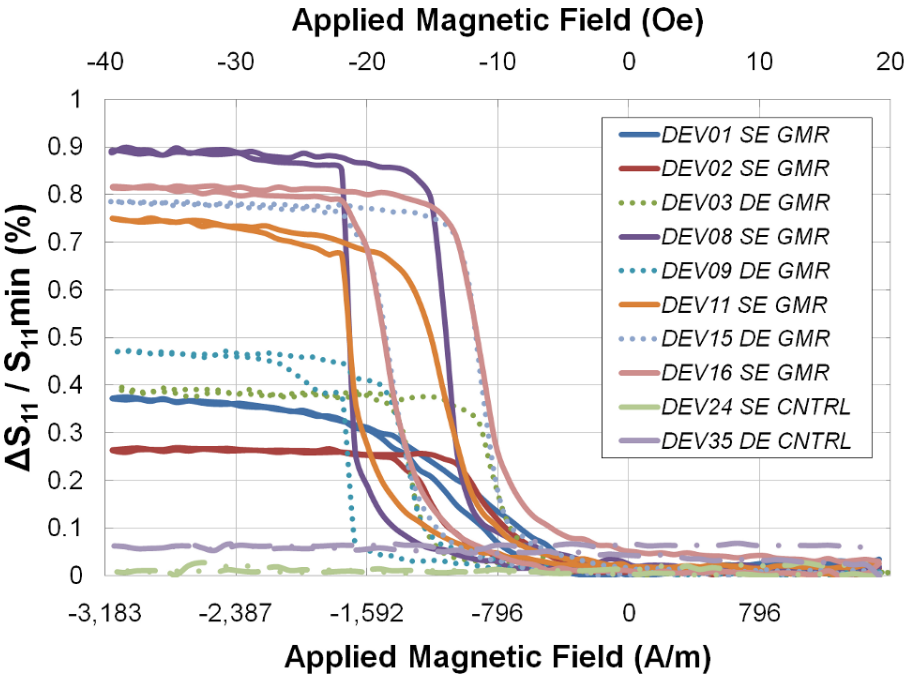

Figure 5.7: $\Delta S_{11}/S_{11}min$ as a function of applied magnetic field for a 8 MP SAW devices and 2 control SAW devices (open reflector SAW devices without GMR bits). 5 S-E and 3 D-E MP SAW devices were measured along with 1 S-E and 1 D-E control device used to confirm that the resistance change of the GMR bits was causing the change in signal response.

previous experiment, the predicted percent change in S_{11} signal for each device was between 0.38% and 0.77%. The actual percent change in S_{11} signal for the devices measured had a wider range of values from 0.27% to 0.90%. Even so, the data presents proof-of-concept results, confirming that an integrated GMR bit can be used as a memory storage element for SAW RFID devices. Although the change is small, under a 1% change in the S_{11} response between the high and low resistance state of the GMR bit load on the interdigital reflector, several improvements can

Device ID	Design *	% S_{11} Change	Switching Fields	Hysteresis
DEV01	SE GMR	0.37%	-1040 : -890 A/m	~150 A/m
DEV02	SE GMR	0.27%	-1200 : -890 A/m	~310 A/m
DEV03	DE GMR	0.40%	-1300 : -830 A/m	~470 A/m
DEV08	SE GMR	0.90%	-1660 : -1100 A/m	~560 A/m
DEV09	DE GMR	0.47%	-1660 : -1350 A/m	~310 A/m
DEV11	SE GMR	0.75%	-1665 : -1125 A/m	~540 A/m
DEV15	DE GMR	0.79%	-1440 : -895 A/m	~545 A/m
DEV16	SE GMR	0.82%	-1440 : -890 A/m	~550 A/m
DEV24	SE Open	0.03%	no switching occurs	none
DEV35	DE Open	0.07%	no switching occurs	none

Table 5.7: Compiled results from MP SAW device measurements, which includes % S_{11} change($\Delta S_{11}/S_{11}min$) normalized to the relative minimum response for the device being measured, the midpoints of the applied magnetic field strength range required to switch the resistance state of the GMR bit (first value for first sweep (+ → -), and second value for return sweep (- → +)), and hysteresis range about the midpoints of the magnetic field strength required to flip the GMR bit. * Design Legend: SE GMR = Single-Electrode MP SAW Device; DE GMR = Double-Electrode MP SAW Device; SE Open = Single-Electrode Open Reflector Device; DE Open = Double-Electrode Open Reflector Device

be made to increase the signal difference between the two states, which will be discussed in Chapter 6. Between the S-E and D-E MP SAW device results, no trends could be picked out that distinguished one set of devices from the other. Both sets of devices had high variability in all parameters reviewed, which is shown in Table 5.8.

The variation in the magnetic field strength required to change the magnetization direction of the free layer in the GMR bit could potentially be attributed to the imperfect parallel alignment of the GMR bit easy axis with the direction of the applied magnetic field. If the GMR bit's easy axis was placed a few degrees

Design	SE GMR	DE GMR
# of devices measured	5	3
Average % S_{11} change	0.62%	0.55%
% S_{11} change Std. Dev.	0.28%	0.21%
% S_{11} change Variation	0.63%	0.39%
Average Switching Field (1)	-1401 A/m	-1467 A/m
Switching Field (1) Std. Dev.	278 A/m	181 A/m
Switching Field (1) Variation	410 A/m	360 A/m
Average Switching Field (2)	-979 A/m	-1025 A/m
Switching Field (2) Std. Dev.	122 A/m	283 A/m
Switching Field (2) Variation	235 A/m	520 A/m
Average Hysteresis	-804 A/m	-867 A/m
Hysteresis Std. Dev.	170 A/m	226 A/m
Hysteresis Variation	382 A/m	430 A/m

Table 5.8: The averages, standard deviations, and variation range are provided for the % S_{11} change, midpoints of the required switching field strength for the (1) [+ to -] and (2) [- to +] field sweeps (i.e. the field strength value that is required to change the GMR bit resistance to halfway in between the low and high resistance state), and the hysteresis of the S-E and D-E GMR MP SAW devices. Variation refers to the difference between the highest and lowest values in the sample set. * Refer to Table 5.7 for the Design Legend.

off parallel with the applied magnetic field, the magnitude of the field strength applied parallel to the easy axis of the bit would be reduced, requiring a stronger field to produce the same results as the case involving perfect alignment of the applied field and the GMR bit easy axis. An experiment to determine how the alignment of the GMR bit easy axis and hard axis with the applied magnetic field affects the S_{11} response of an MP SAW device was performed. This experiment will be detailed in the next section.

The variation in the percent change in the S_{11} response can probably be attributed to the resistance variation of the GMR bit. Both the base resistance when the GMR bit is in the low resistance state, and the amount of change in resistance when the GMR bit switches to its high resistance state vary from bit to bit, which is shown in Table 5.4. Geometry variation, damage to the thin film during processing, and differences in the annealing of the GMR bits could explain the S_{11} response variation between devices.

5.4 MP SAW Device Response with respect to GMR Bit Orientation

S_{11} measurements were taken on two MP SAW devices which were placed in an applied magnetic field with the GMR bit oriented in two different ways. Each device was measured with the GMR bit's easy axis oriented parallel to the applied magnetic field (as performed in the previous experiment), and again with the GMR bit's easy axis oriented perpendicular to the applied magnetic field (also referred to as the hard axis of the GMR bit). This was done to gain a qualitative understanding of how the magnetic field orientation with respect to the GMR bit affects the reflection response of an MP SAW device. It would be expected that the S_{11} response will only change as a function of applied magnetic field along the easy axis due to the magnetic alignment of the pinning layer. Along the hard axis of the GMR bit, minimal change in the S_{11} response should occur since the magnetization of the pinned magnetic layer and the free magnetic layer will never be parallel along that axis. It should be noted that the applied magnetic field used, while strong enough to change the magnetization of the free magnetic layer in the GMR film, will not be strong enough to change the magnetization of the pinned magnetic layer. The field range used is specfied in the next paragraph. One S-E MP SAW device (DEV16) and one D-E MP SAW device (DEV15) were measured in this experiment. An illustration of the device orientations to be measured in the field is provided in Figure 5.8.

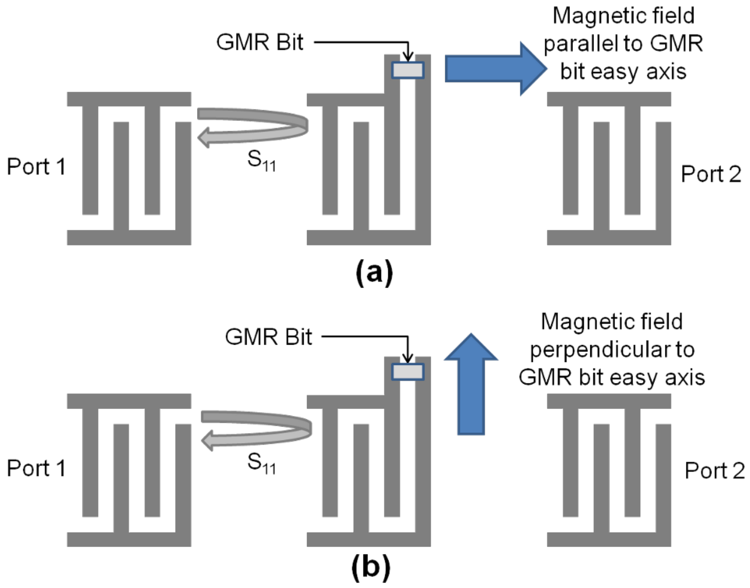

Figure 5.8: Illustration of the two magnetic field orientations applied to the two SAW devices. (a) shows the applied magnetic field parallel to the easy axis of the GMR bit while (b) shows the applied magnetic field perpendicular to the easy axis (parallel to the hard axis of the GMR bit). A S-E MP SAW device and a D-E MP SAW device were measured in this experiment.

The measurements were taken using the setup shown in Figure 4.11. The applied magnetic field was stepped from 1520 A/m (20 Oe) to -3130 A/m (-38 Oe) and back to 1520 A/m (20 Oe). The magnetic field was stepped every 77.5 A/m (~1 Oe). The network analyzer settings used are provided in Table 5.9. Figure 5.9 provides a plot of the normalized S_{11} response from a S-E MP SAW device

(DEV16) and a D-E MP SAW device (DEV15) with the magnetic field aligned along both the easy axis and hard axis of the GMR bits.

ENA Settings	**Value**
S-Parameters	S_{11}
Frequency Scan Range	65 MHz - 75 MHz
IF Bandwidth	5 kHz
Averaging	ON (6 samples)
Smoothing	OFF (0%)
Time Gating	700 ns - 1500 ns
Data Points	122
Data Format	Linear magnitude
Marker Mode	Maximum (@ f_0)

Magnetic Field Settings	Value
Magnetic Field Range	1520A/m to -3130A/m
# of Field Steps	61 per direction
Field Sweep Direction	positive to negative to positive

Table 5.9: Network analyzer settings and magnetic field settings for MP SAW device measurements with varying GMR bit orientations with respect to the applied magnetic field.

The data confirms the notion that the pinned layer's magnetization is parallel to the easy axis, so regardless of the applied magnetic field magnitude and sign along the hard axis of the GMR bit, minimal change in the reflection response should occur.

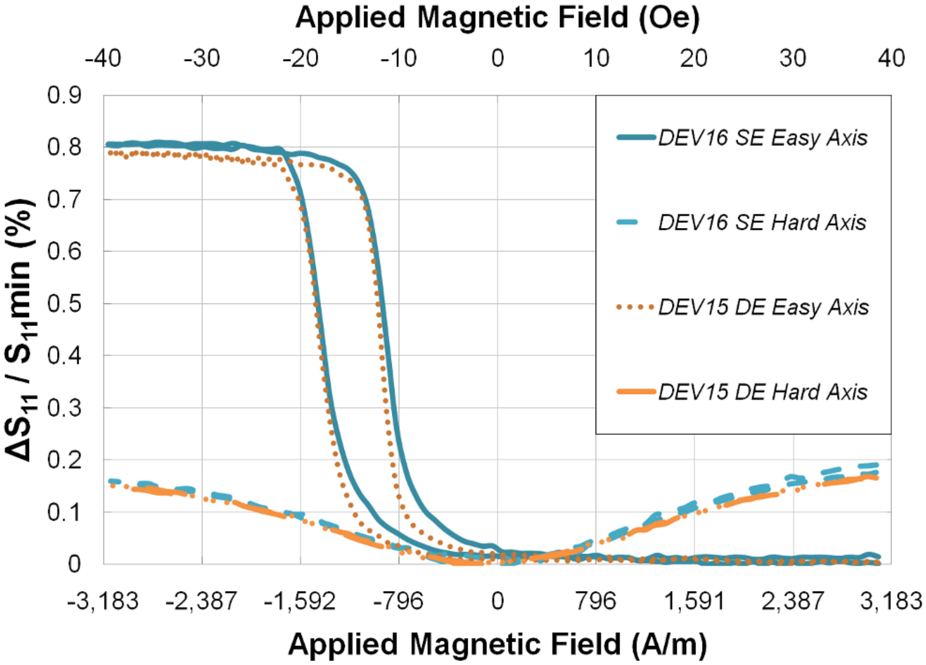

Figure 5.9: Plot of the normalized S_{11} response ($\Delta S_{11}/S_{11}min$) as a function of applied magnetic field when the MP SAW devices are oriented in the applied magnetic field parallel to the easy axis and parallel to the hard axis of the GMR bit. 2 MP SAW devices (DEV24, S-E and DEV35, D-E) were measured.

Chapter 6 – Conclusions

The purpose of this thesis and research was to design and fabricate a proof-of-concept for a magnetically-programmable surface acoustic wave device that demonstrated the use of an integrated giant magnetoresistive bit as a memory element. An MP SAW device was fabricated and the reflection response was experimentally shown to change with the GMR resistance state. While prior work performed by Reindl [15] and Fu [16] demonstrated the ability to program the reflection response of SAW devices, the work performed for this thesis was unique for its use of an integrated, magnetically-tuned impedance loading element - the GMR bit.

6.1 Summary

Eight different types of SAW devices were designed, fabricated, and characterized based on two different IDT designs. A single-electrode and double-electrode IDT design (shown in Figure 2.5 (a) and (b) respectively) were used as the basis for a SAW delay line, a SAW device with an open-circuited reflector (Figure 5.1, (a) and (c)), a SAW device with a short-circuited reflector (Figure 5.1 (b) and (d)), and an MP SAW device (Figure 5.6). Results from the four experiments performed show that a MP SAW device with an integrated GMR bit is capable of acting as a memory element based on the fluctuating reflection response from a change in

GMR bit resistance.

Results from the first experiment provides information on the ideal reflection response differential between an interdigital reflector with an infinite load impedance and one with no load impedance. While not conclusive, evidence that the change in reflection response between an ideal interdigital reflector impedance load of 0 Ω and ∞ Ω, defined as $\frac{S_{11open}-S_{11shorted}}{S_{11shorted}}$, could be 1,400% or greater was shown for the SAW devices with open- and short-circuited reflectors based on the double-electrode IDT design. The reflection response difference between the open- and short-circuited SAW devices based on the single-electrode IDT design was more modest, with ~112% change. Although more devices need to be measured to validate the results, a figure for the maximum reflection response change for an interdigital reflector was established.

In the second experiment, data was collected from SAW devices with a load-tunable reflector (in the form of a discrete potentiometer placed across the terminals of an open-circuited interdigital reflector) to determine the reflection response change to be expected from the fabricated GMR bits. The change in reflection response as a function of load resistance was simulated and then experimentally determined. The simulations predicted a logarithmic change in reflection response as a function of load resistance, while the experimental data followed more closely with a linear curve. The experimental results using a potentiometer in place of GMR bit suggests that a 0.23%/Ω change should be expected for SAW devices with an S-E IDT design, and a 0.19%/Ω change should be expected for SAW devices with a D-E IDT design.

The third experiment confirms the viability of using integrated GMR bits in SAW devices to magnetically program the reflection response. Eight MP SAW devices were measured in a magnetic field swept from 1520 A/m to -3130 A/m. All MP SAW devices exhibited a change in reflection response when a critical field strength was reached to change the magnetization of the free layer in the GMR bit. The change in the reflection responses of the devices ranged from 0.27% to 0.90%. Considering that the GMR bits have a 1 Ω to 3 Ω resistance change between the low and high states, the results agree with the predicted reflection response changes in the second experiment.

The fourth experiment compared the reflection response change of MP SAW devices when the magnetic field was swept along the direction of the GMR bit easy axis and hard axis. For the MP SAW devices measured, the change in reflection response with the field applied along the easy axis was ~0.8% between -1400 A/m and -400 A/m (the magnetic field range where the GMR bit change resistance states), matching the results from the previous experiment. The change in reflection response when the field was applied along the hard axis was less than 0.1% between -1400 A/m and -400 A/m. The results show that only the magnetic field component along the easy axis of the GMR bit contributes towards rotating the free layer's magnetization by 180°, parallel to the pinned layer's magnetization direction.

6.2 Recommendations for Future Work

The research performed in this thesis provides a starting point for MP SAW device development. To be able to use these devices for RFID applications, the difference in reflection response between the low resistance state and the high resistance state of the interdigital reflector load must be improved, multiple interdigital reflectors with magnetically-tunable loads will be needed on one device to provide more than one bit of memory, and additional components such as antennas and proper packaging will need to be designed for use in wireless RFID applications.

6.2.1 Improving Reflection Response

The reflection response change between the high and low resistance states can be improved through better impedance matching of the reflector and IDT structures. The load impedance across the interdigital reflector, as well as additional impedances from the wirebonds, packaging and contact pads change the calculated IDT impedance substantially. Future device work should take these impedances into account through the use of tunable impedance elements (e.g., tunable capacitors or inductors), or redesigning the IDT structures. Better, more controlled impedance matching used to minimize reflections at the low resistance state will improve the reflection response dynamic range.

The reflection response difference between the high and low resistance states can be improved by using a tunable load with a larger difference between the high and low resistance states. The GMR bits used in this research had a high-to-low state resistance difference between 1 Ω to 3 Ω, with a $\Delta R/R_{min}$ of ~3-4%. GMR bits made out of thin film stacks with a higher $\Delta R/R_{min}$ value would improve the performance of the MP SAW device. A discrete TMR bit with a $\Delta R/R_{min}$ of ~25% has given a reflection response change of ~9% compared to 0.9% change seen with the integrated NIST-fabricated GMR bit.

6.2.2 Adding more Memory Elements

For an MP SAW device to be useful as an RFID tag, multiple bits will need to be available for creating unique identification codes. This research has shown the possibility of using an integrated GMR bit load on an interdigital reflector as a memory element for RFID applications, but the effects of aligning multiple reflector structures in a row has not been explored. Issues such as propagation loss and signal distortion between reflectors will need to be examined to determine the feasibility of using an MP SAW device an RFID tag.

6.2.3 Antenna Development

To use MP SAW devices in wireless RFID applications, an antenna will need to be designed to match the impedance of the transmitting IDT while also accepting the appropriate RF signal. Since the interrogation signal provides both the energy and the modulated data to the MP SAW device, it is crucial that the antenna also be designed with a high absorption efficiency at the desired RF frequency. A higher absorption efficiency results in a longer interrogation range.

Bibliography

[1] H. Engan, "Surface acoustic wave multielectrode transducers," *IEEE Transactions on Sonics and Ultrasonics*, vol. 22, pp. 395–401, Nov. 1975.

[2] P. Blythe, "RFID for road tolling, Road-Use pricing and vehicle access control," in *IEE Colloquium on RFID Technology*, (London, UK), pp. 8/1–8/16, Oct. 1999.

[3] V. Chawla and D. S. Ha, "An overview of passive RFID," *IEEE Communications Magazine*, vol. 45, pp. 11–17, Sept. 2007.

[4] S. Lahiri, *RFID Sourcebook.* Upper Saddle River, NJ: IBM Press, 1st ed., 2006.

[5] J. Landt, "The history of RFID," *IEEE Potentials*, vol. 24, pp. 8–11, Oct. 2005.

[6] S. Preradovic and N. C. Karmakar, "RFID transponders," in *International Conference on Electrical and Computer Engineering, 2006. ICECE '06*, vol. 1, (Dhaka, Bangladesh), pp. 96–99, Dec. 2006.

[7] G. Benelli, S. Parrino, and A. Pozzebon, "Possible configurations and geometries of long range HF RFID antenna gates," in *6th International Symposium on Wireless Communication Systems, 2009. Proceedings.*, vol. 1, (Tuscany, Italy), pp. 46–50, Sept. 2009.

[8] M. E. Bazakos, Y. Ma, and A. H. Johnson, "Fast access control technology solutions (FACTS)," in *IEEE Conference on Advanced Video and Signal Based Surveillance, 2005. Conference Proceedings*, vol. 1, (Como, Italy), pp. 312–317, Sept. 2005.

[9] A. Fennani and H. Hamam, "An optimized RFID-based academic library," in *Second International Conference on Sensor Technologies and Applications, 2008, Conference Proceedings*, vol. 1, (Cap Esterel, France), pp. 44–48, Aug. 2008.

[10] R. Morales-Salcedo, H. Ogata, and Y. Yano, “Towards a new digital library infrastructure with RFID for mobile e-learning,” in *IEEE International Workshop on Wireless and Mobile Technologies in Education, 2005. Workshop Proceedings*, (Tokushima, Japan), pp. 1–3, Nov. 2005.

[11] H. Lin, W. Lo, and C. Chiang, “Using RFID in supply chain management for customer service,” in *IEEE International Conference on Systems, Man and Cybernetics, 2006, Conference Proceedings*, vol. 2, (Taipei, Taiwan), pp. 1377–1381, Oct. 2006.

[12] D. Yue, X. Wu, and J. Bai, “RFID application framework for pharmaceutical supply chain,” in *IEEE International Conference on Service Operations, Logistics, and Informatics, 2008 Proceedings*, vol. 1, (Beijing, China), pp. 1125–1130, Oct. 2008.

[13] Y. B. Thakare, S. S. Musale, and S. R. Ganorkar, “A technological review of RFID & applications,” vol. 1, (Mumbai, India), pp. 65–70, 2008.

[14] S. C. Bono, M. Green, A. Stubblefield, A. Juels, A. D. Rubin, and M. Szydlo, “Security analysis of a cryptographically-enabled RFID device,” in *14th Usenix Security Symposium Conference Proceedings*, vol. 1, (Baltimore, MD), pp. 1–16, Aug. 2005.

[15] L. Reindl and W. Ruile, “Programmable reflectors for SAW-ID-Tags,” in *IEEE 1993 Ultrasonics Symposium Proceedings*, vol. 1, (Baltimore, MD), pp. 125–130, Nov. 1993.

[16] Q. Fu, H. Stab, and W. Fischer, “Investigation of single-finger interdigital transducer as programmable reflector,” in *IEEE 2004 Ultrasonics Symposium Proceedings*, vol. 3, (Montreal, Quebec), pp. 2000–2003, Aug. 2004.

[17] Q. Fu, H. Stab, and W. Fischer, “Wireless passive SAW sensors using single-electrode-type IDT structures as programmable reflectors,” *Sensors and Actuators A: Physical*, vol. 122, pp. 203–208, Aug. 2005.

[18] J. Bamfield, “Key findings from the global retail theft barometer 2009,” Briefing 2009, Nottingham Centre for Retail Research, Nottingham, UK, 2010.

[19] K. Michael and L. McCathie, “The pros and cons of RFID in supply chain management,” in *International Conference on Mobile Business, 2005 Proceedings*, vol. 1, (Sydney, Australia), pp. 623–629, July 2005.

[20] B. Drafts, "Acoustic wave technology sensors," *IEEE Transactions on Microwave Theory and Techniques*, vol. 49, pp. 795–802, Apr. 2001.

[21] G. McHale, F. Martin, and M. I. Newton, "Mass sensitivity of acoustic wave devices from group and phase velocity measurements," *Journal of Applied Physics*, vol. 92, pp. 3368–3373, Sept. 2002.

[22] A. Pohl, "A review of wireless SAW sensors," *IEEE Transactions on Ultrasonics, Ferroelectrics, and Frequency Control*, vol. 47, pp. 317–332, Mar. 2000.

[23] V. P. Plessky, "Review on SAW RFID tags," in *IEEE International Frequency Control Symposium, 2009 Joint with the 22nd European Frequency and Time Forum Proceedings*, vol. 1, (Besancon, France), pp. 14–23, Apr. 2009.

[24] L. Reindl, "Unwired SAW sensors systems," in *Proceedings of the European Microwave Association*, vol. 3, (Munich, Germany), pp. 110–119, European Microwave Association, June 2007.

[25] D. S. Ballantine, R. M. White, S. J. Martin, A. J. Ricco, E. T. Zellers, G. C. Frye, and H. Wohltjen, *Acoustic Wave Sensors: Theory, Design, and Physicco-Chemical Applications.* Applications of Modern Acoustics, San Diego, CA: Academic Press Inc., 1 ed., 1997.

[26] D. P. Morgan, *Surface-Wave Devices for Signal Processing.* No. 19 in Studies in Electrical and Electronic Engineering, New York, NY: Elsevier Science Publishing, paperback ed., 1991.

[27] C. Campbell, *Surface Acoustic Wave Devices and Their Signal Processing Applications.* San Diego, CA: Academic Press, Inc., 1 ed., 1989.

[28] S. Datta, *Surface Acoustic Wave Devices.* Edgewood Cliffs, New Jersey: Prentice-Hall, 1 ed., 1986.

[29] C. C. W. Ruppel, L. Reindl, and R. Weigel, "SAW devices and their wireless communications applications," *IEEE Microwave Magazine*, vol. 3, pp. 65–71, June 2002.

[30] R. M. White and F. W. Voltmer, "Direct piezoelectric coupling to surface elastic waves," *Applied Physics Letters*, vol. 7, pp. 314–316, Dec. 1965.

[31] D. P. Morgan, "History of SAW devices," vol. 1, (Pasadena, CA), pp. 439–460, May 1998.

[32] T. W. Bristol, W. R. Jones, P. B. Snow, and W. R. Smith, "Applications of double electrodes in acoustic surface wave device design," *IEEE 1972 Ultrasonics Symposium Proceedings*, vol. 1, pp. 343–345, 1972.

[33] H. Engan, "High-frequency operation of surface-acoustic-wave multielectrode transducers," *Electronics Letters*, vol. 10, pp. 395–396, Sept. 1974.

[34] W. R. Smith, H. M. Gerard, J. H. Collins, T. M. Reeder, and H. J. Shaw, "Analysis of interdigital surface wave transducers by use of an equivalent circuit model," *IEEE Transactions on Microwave Theory and Techniques*, vol. 17, pp. 856–864, Nov. 1969.

[35] A. J. Ricco and S. J. Martin, "Multiple-frequency surface acoustic wave devices as sensors," in *IEEE Solid-State Sensor and Actuator Workshop, 1990 4th Technical Digest*, vol. 1, (Hilton Head Island, SC), pp. 5–8, June 1990.

[36] G. A. Coquin and H. F. Tiersten, "Analysis of the excitation and detection of piezoelectric surface waves in quartz by means of surface electrodes," *Journal of the Acoustical Society of America*, vol. 41, pp. 921–939, Apr. 1967.

[37] S. G. Joshi and R. M. White, "Excitation and detection of surface elastic waves in piezoelectric crystals," *Journal of the Acoustical Society of America*, vol. 46, pp. 17–27, July 1969.

[38] H. Skeie, "Mechanical and electrical reflections in interdigital transducers," in *IEEE 1972 Ultrasonics Symposium Proceedings*, vol. 1, (Boston, MA), pp. 408–412, 1972.

[39] W. R. Smith, "Experimental distinction between crossed-field and in-line three-port circuit models for interdigital transducers," *IEEE Transactions on Microwave Theory and Techniques*, vol. 22, pp. 960–964, Nov. 1974.

[40] R. H. Tancrell and M. G. Holland, "Acoustic surface wave filters," *Proceedings of the IEEE*, vol. 59, pp. 393–409, Mar. 1971.

[41] C. S. Hartmann, D. T. Bell, and R. C. Rosenfeld, "Impulse model design of acoustic surface-wave filters," *IEEE Transactions on Microwave Theory and Techniques*, vol. 21, pp. 162–175, Apr. 1973.

[42] R. Pallas-Areny and J. G. Webster, *Sensors and Signal Conditioning.* New York, NY: John Wiley & Sons, Inc., 2nd ed., 2001.

[43] U. Wolff, F. L. Dickert, G. K. Fischerauer, W. Greibl, and C. C. W. Ruppel, "SAW sensors for harsh environments," *IEEE Sensors Journal*, vol. 1, pp. 4–13, June 2001.

[44] L. Reindl, T. Ostertag, W. Ruile, H. Scherr, C. Ruppel, and F. Schmidt, "Wireless remote identification and sensing with SAW devices," in *Proceedings SENSOR '97*, vol. 1, (Numberg, Germany), pp. 161–166, SENSOR, 1997.

[45] G. Scholl, F. Schmidt, T. Ostertag, L. Reindl, H. Scherr, and U. Wolff, "Wireless passive SAW sensor systems for industrial and domestic applications," in *1998 IEEE Frequency Control Symposium Proceedings*, vol. 1, (Pasadena, CA), pp. 595–601, May 1998.

[46] M. N. Baibich, J. M. Broto, A. Fert, F. N. V. Dau, and F. Petroff, "Giant magnetoresistance of (001)Fe/(001)Cr magnetic superlattices," *Physical Review Letters*, vol. 61, pp. 2472–2475, Nov. 1988.

[47] J. Inoue and S. Maekawa, "Theory of magnetoresistance in multilayers," *IEEE Translation Journal on Magnetics in Japan*, vol. 8, pp. 370–380, June 1993.

[48] M. Ross, "GMR: an attractive resistance," *Europhysics News*, vol. 28, pp. 114–118, Sept. 1997.

[49] G. Binasch, P. Grunberg, F. Saurenbach, and W. Zinn, "Enhanced magnetoresistance in layered magnetic structures with antiferromagnetic interlayer exchange," *Physical Review B*, vol. 39, pp. 4828–4830, Mar. 1989.

[50] R. L. White, "Giant magnetoresistance: A primer," *IEEE Transactions on Magnetics*, vol. 28, pp. 2482–2487, Sept. 1992.

[51] E. Y. Tsymbal and D. G. Pettifor, "Perspectives of giant magnetoresistance," in *Solid State Physics*, vol. 56, pp. 113–237, San Diego, CA: Academic Press, Inc., 1st ed., 2001.

[52] M. A. Ruderman and C. Kittel, "Indirect exchange coupling of nuclear magnetic moments by conduction electrons," *Physical Review*, vol. 96, pp. 99–102, Oct. 1954.

[53] T. Kasuya, "A theory of metallic ferro- and antiferromagnetism on zener's model," *Progress of Theoretical Physics*, vol. 16, pp. 45–57, July 1956.

[54] K. Yosida, "Magnetic properties of Cu-Mn alloys," *Physical Review*, vol. 106, pp. 893–898, June 1957.

[55] J. Dai and J. Tang, "Direct measurement of the dependence of granular giant magnetoresistance on the relative orientation of magnetic granules," *Applied Physics Letters*, vol. 76, pp. 3968–3970, June 2000.

[56] H. Matthews, ed., *Surface Wave Filters: Design, Construction, and Use.* New York: John Wiley & Sons, Inc., 1 ed., 1977.

[57] H. Skeie, "Electrical and mechanical loading of a piezoelectric surface supporting surface waves," *Journal of the Acoustical Society of America*, vol. 48, pp. 1098–1109, Nov. 1970.

[58] W. R. Smith, "Minimizing multiple transit echoes in surface wave devices," in *IEEE 1973 Ultrasonics Symposium Proceedings*, vol. 1, (Monterey, CA), pp. 410–413, Nov. 1973.

[59] K. Hanma and B. J. Hunsinger, "A triple transit suppression technique," in *IEEE 1976 Ultrasonics Symposium Proceedings*, vol. 1, (Annapolis, MD), pp. 328–331, 1976.

[60] G. Tobolka, "Mixed matrix representation of SAW transducers," *IEEE Transactions on Sonics and Ultrasonics*, vol. 26, pp. 426–427, Nov. 1979.

[61] R. C. Jaeger, *Introduction to Microelectronic Fabrication*, vol. 5 of *Modular Series on Solid State Devices.* Upper Saddle River, NJ: Prentice-Hall, 2nd ed., 2002.

[62] S. Wolf and R. N. Tauber, "Aluminum thin films and physical vapor deposition in ULSI," in *Silicon Processing for the VLSI Era*, vol. 1, pp. 434–487, Sunset Beach, CA: Lattice Press, 2nd ed., 2000.

APPENDICES

Appendix A – OSU Fabrication Process Details

Process Step	**Description and Details**
Substrate Start	Substrate - 25.4 mm x 25.4 mm Y-Z lithium niobate substrates
	Pre-deposited Films - NVE Corp GMR thin film stack
Substrate Clean	Solvents - Acetone, isopropyl alcohol, deionized water rinse
	Drying - Nitrogen gas blow dry, 5 min dehydration @ 125°C
Photoresist Deposit	Pretreatment - Omnicoat (adhesion treatment)
	Spin Speed - 3,000 RPM
	Spin Time - 30 s
	Soft Bake Temperature - 200°C
	Soft Bake Time - 120 s
	Photoresist Type - SU-8 (negative photoresist)
	Spin Speed - 3,000 RPM
	Spin Time - 30 s
	Soft Bake 1 Temperature - 65°C
	Soft Bake 1 Time - 60 s
	Soft Bake 2 Temperature - 95°C
	Soft Bake 2 Time - 120 s

Process Step	**Description and Details**
Photolithography	Alignment/Exposure Tool - Karl Suss MJB3 Aligner
	Mask - GMR bit mask (GMR bit patterning)
	Exposure Time - 15 s
Development	Developer Solution - SU-8 Developer
	Development Temperature - 25°C
	Development Time - 180 s
	Development Agitation - Yes (manually agitated by hand)
Device Clean	Solvents - Isopropyl alcohol rinse
	Drying - Nitrogen gas blow dry
Dry Etch	Etch Tool - PlasmaLabs Reactive Ion Etcher (milling mode)
	Plasma Clean Pressure - 190 mTorr
	Plasma Clean Gases - Oxygen @ 35 sccm
	Plasma Clean RF Power - 100 W
	Plasma Clean Time - 30 s
	Ion Milling Pressure - 10 mTorr
	Ion Milling Gases - Ar @ 25 sccm
	Ion Milling RF Power - 150 W
	Ion Milling Voltage - 531V to 558V
	Ion Milling Time - 90 min
Photoresist Removal	PR Stripping Solution Type - Nano PG Remover
	PR Stripping Solution Temperature - 80°C
	PR Stripping Solution Time - 40 min

Process Step	Description and Details
Device Clean	Solvents - Acetone, isopropyl alcohol, deionized water rinse
	Drying - Nitrogen gas blow dry
Photoresist Deposit	Photoresist Type - Shipley 1818
	Spin Speed - 4,000 RPM
	Spin Time - 30 s
	Soft Bake Temperature - 85°C
	Soft Bake Time - 60 s
Photolithography	Alignment/Exposure Tool - Karl Suss MJB3 Aligner
	Mask - IDT mask (interdigital transducer patterning)
	Exposure Time - 5 s
Development	Developer Solution - 4:1, deionized water:Microposit 351
	Development Temperature - 25°C
	Development Time - 75 s
	Development Agitation - Yes (manually agitated by hand)
Device Clean	Solvents - Deionized water
	Drying - Nitrogen gas blow dry
Metal Deposition	Deposition Method - Thermal Evaporation
	Deposition Tool - Polaron Tabletop Thermal Evaporator
	Material Type - Aluminum
	Deposition Pressure - $3.5x10^{-5}$ mbar
	Deposition Time - ~5 min
	Deposited Film Thickness - 350 nm +/- 10 nm

Process Step	**Description and Details**
Lift-Off	Solution - Baker PRS-3000 (Photoresist stripper)
	Solution Temperature - 75°C
	Immersion Time - 4 hours
	Post Treatment - Agitation and manual metal removal
Device Clean	Solvents - Acetone, isopropyl alcohol, deionized water rinse
	Drying - Nitrogen gas blow dry
Inspection	Visual inspection performed with optical microscope

Appendix B – ARL Fabrication Process Details

Process Step	**Description and Details**
Wafer Start	3” lithium niobate wafers
Clean	Solution - Acetone/isopropyl alcohol/deionized water rinse
	Drying - Nitrogen gas blow dry
Ashing	Tool - Metroline M4L Plasma Asher
	Recipe - 5 minute descum recipe (200 W oxygen plasma)
Photoresist Deposit	Photoresist Type - AZ 5214 (positive/reverse image resist)
	Photoresist Quantity - 10 mL
	Spin Speed - 2000 RPM
	Spin Time - 40 s
	Soft Bake Temperature - 110°C
	Soft Bake Time - 60 s
Photolithography	Aligner/Exposure Tool - Karl Suss MA6 Aligner (New)
	Mask - GMR bit light field mask (GMR bit patterning)
	Contact Type - Hard
	Alignment Gap - 40 µm
	Exposure Time - 1.1 s to 1.0 s
	Power/Channel - 320-350 W / Channel 1

Process Step	**Description and Details**
Reverse Image Bake	Soft Bake Temperature - 120°C
	Soft Bake Time - 60 s
Photolithography	Aligner/Exposure Tool - Karl Suss MA6 Aligner (New)
	Mask - None (Glass Blank)
	Contact Type - Flood-E (Flood Exposure)
	Alignment Gap - 40 µm
	Exposure Time - 25 s
	Power/Channel - 320-350 W / Channel 1
Development	Developer Solution - AZ 300 MIF developer
	Development Temperature - 25°C
	Development Time - 45 s to 60 s
	Development Agitation - Yes (manually agitated by hand)
Clean	Solution - Deionized water rinse
	Drying - Nitrogen gas blow dry
Ashing	Tool - Metroline M4L Plasma Asher
	Recipe - 5 minute descum recipe (200 W oxygen plasma)
GMR Deposition	Deposition Tool/Type - NIST custom sputtering system
	*Samples at this point were outsourced to NIST
	Wafers returned with a deposited GMR film stack.

Process Step	**Description and Details**
Lift-Off	Solution - Baker PRS-3000 (Photoresist stripper)
	Temperature - 75°C
	Time - 2 hr to 4 hr
	Agitation - Yes (manual agitation by hand)
Clean	Solution - Deionized water rinse
	Drying - Nitrogen gas blow dry
Ashing	Tool - Metroline M4L Plasma Asher
	Recipe - 5 minute descum recipe (200 W oxygen plasma)
	Ashing Time - 5 min
Photoresist Deposit	Photoresist Type - AZ 5214 (positive/reverse image resist)
	Photoresist Quantity - 10 mL
	Spin Speed - 2000 RPM
	Spin Time - 40 s
	Soft Bake Temperature - 110°C
	Soft Bake Time - 60 s
Photolithography	Aligner/Exposure Tool - Karl Suss MA6 Aligner (New)
	Mask - IDT light field mask (IDT Patterning)
	Contact Type - Hard
	Alignment Gap - 40 µm
	Exposure Time - 1.1 s to 1.0 s
	Power/Channel - 320-350 W / Channel 1
Reverse Image Bake	Soft Bake Temperature - 120°C
	Soft Bake Time - 60 s

Process Step	**Description and Details**
Photolithography	Aligner/Exposure Tool - Karl Suss MA6 Aligner (New)
	Mask - None (Glass Blank)
	Contact Type - Flood-E (Flood Exposure)
	Alignment Gap - 40 µm
	Exposure Time - 25 s
	Power/Channel - 320-350 W / Channel 1
Development	Developer Solution - AZ 300 MIF developer
	Development Temperature - 25°C
	Development Time - 45 s to 60 s
	Development Agitation - Yes (manually agitated by hand)
Clean	Solution - Deionized water rinse
	Drying - Nitrogen gas blow dry
Ashing	Tool - Metroline M4L Plasma Asher
	Recipe - 5 minute descum recipe (200 W oxygen plasma)
Metal Deposition	Deposition Method - Electron beam evaporation
	Deposition Tool - CHA E-beam Evaporator
	Base Pressure - 1x10^{-6} torr to 4x10^{-7} torr
	Base Temperature - 25°C
	Metal 1 - Ti
	Power Level for Metal 1 - 40% to 50%
	Deposition Rate for Metal 1 - 0.1 nm/s to 0.2 nm/s
	Final Thickness of Metal 1 - 10 nm

Process Step	**Description and Details**
Metal Deposition	Metal 2 - Au
	Power Level for Metal 2 - 40% to 70%
	Deposition Rate for Metal 2 - 0.2 nm/s to 0.4nm/s
	Final Thickness of Metal 2 - 300 nm
	Time Under Vacuum - 3 to 12 hours
Lift-Off	Solution - Baker PRS-3000 (Photoresist stripper)
	Temperature - 75°C
	Time - 2 hr to 4 hr
	Agitation - Yes (manual agitation by hand)
Clean	Solution - Deionized water rinse
	Drying - Nitrogen gas blow dry
Ashing	Tool - Metroline M4L Plasma Asher
	Recipe - 5 minute descum recipe (200 W oxygen plasma)
	Ashing Time - 5 min
Inspection	Visual inspection performed with optical microscope

Appendix C – LabVIEW Block Diagrams

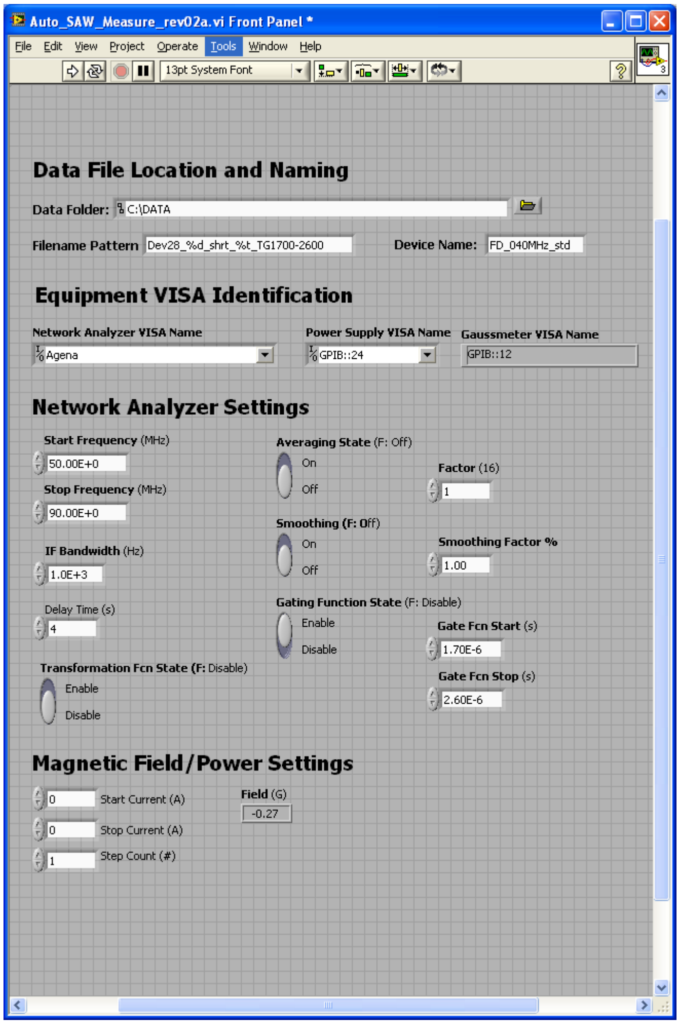

Data File Location and Naming

Data Folder: C:\DATA

Filename Pattern Dev28_%d_shrt_%t_TG1700-2600

Device Name: FD_040MHz_std

Equipment VISA Identification

Network Analyzer VISA Name Agena

Power Supply VISA Name GPIB::24

Gaussmeter VISA Name GPIB::12

Network Analyzer Settings

Start Frequency (MHz) 50.00E+0

Stop Frequency (MHz) 90.00E+0

IF Bandwidth (Hz) 1.0E+3

Delay Time (s) 4

Transformation Fcn State (F: Disable) Enable / Disable

Averaging State (F: Off) On / Off

Factor (16) 1

Smoothing (F: Off) On / Off

Smoothing Factor % 1.00

Gating Function State (F: Disable) Enable / Disable

Gate Fcn Start (s) 1.70E-6

Gate Fcn Stop (s) 2.60E-6

Magnetic Field/Power Settings

Start Current (A) 0

Stop Current (A) 0

Step Count (#) 1

Field (G) -0.27

LabVIEW program user interface that measures S-parameters as a function of frequency

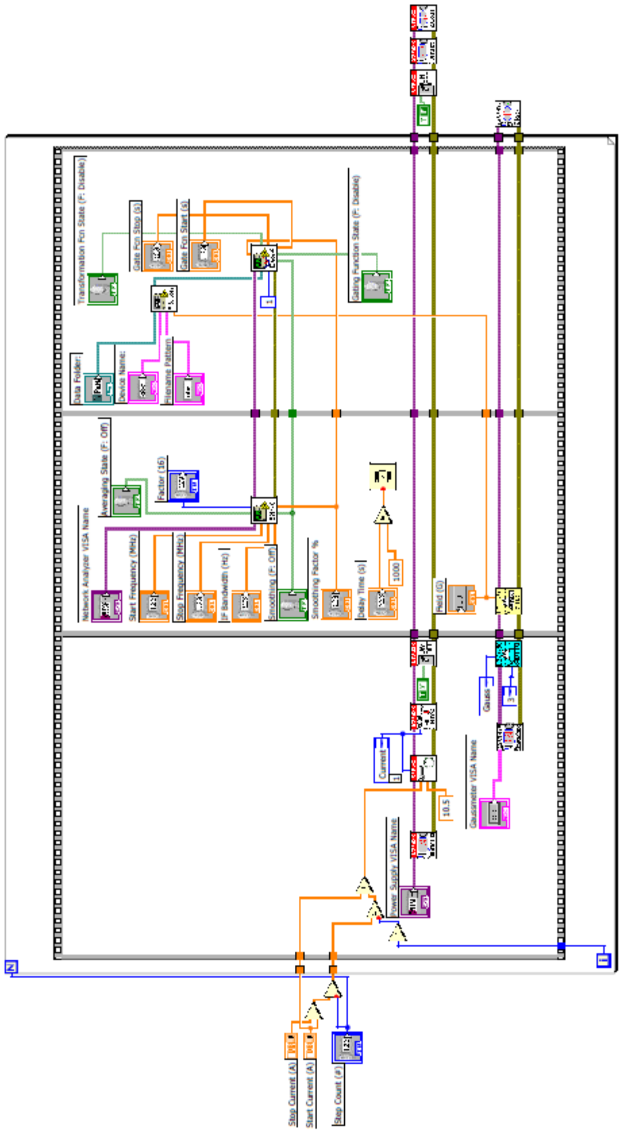

LabVIEW program block diagram that measures S-parameters as a function of frequency

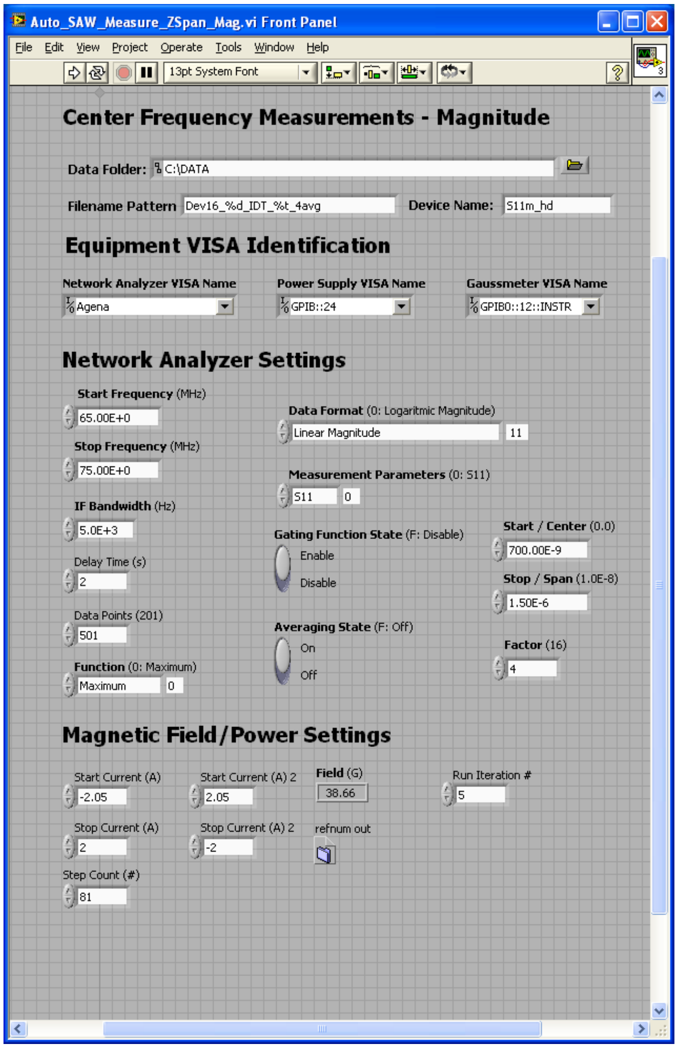

Center Frequency Measurements - Magnitude

Data Folder: C:\DATA

Filename Pattern: Dev16_%d_IDT_%t_4avg

Device Name: S11m_hd

Equipment VISA Identification

Network Analyzer VISA Name: Agena

Power Supply VISA Name: GPIB::24

Gaussmeter VISA Name: GPIB0::12::INSTR

Network Analyzer Settings

Start Frequency (MHz): 65.00E+0

Stop Frequency (MHz): 75.00E+0

IF Bandwidth (Hz): 5.0E+3

Delay Time (s): 2

Data Points (201): 501

Function (0: Maximum): Maximum 0

Data Format (0: Logaritmic Magnitude): Linear Magnitude 11

Measurement Parameters (0: S11): S11 0

Gating Function State (F: Disable): Enable / Disable

Averaging State (F: Off): On / Off

Start / Center (0.0): 700.00E-9

Stop / Span (1.0E-8): 1.50E-6

Factor (16): 4

Magnetic Field/Power Settings

Start Current (A): -2.05

Stop Current (A): 2

Step Count (#): 81

Start Current (A) 2: 2.05

Stop Current (A) 2: -2

Field (G): 38.66

refnum out

Run Iteration #: 5

LabVIEW program user interface that measures S-parameter magnitude as a function of applied magnetic field

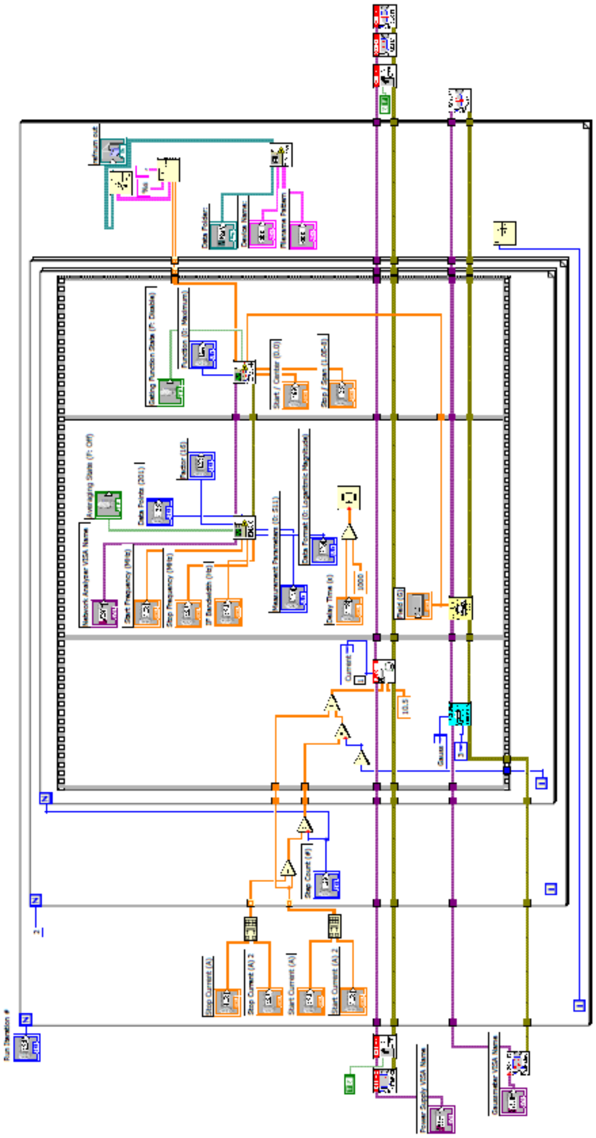

LabVIEW program block diagram that measures S-parameter magnitude as a function of applied magnetic field

Appendix D – Network Analyzer Settings

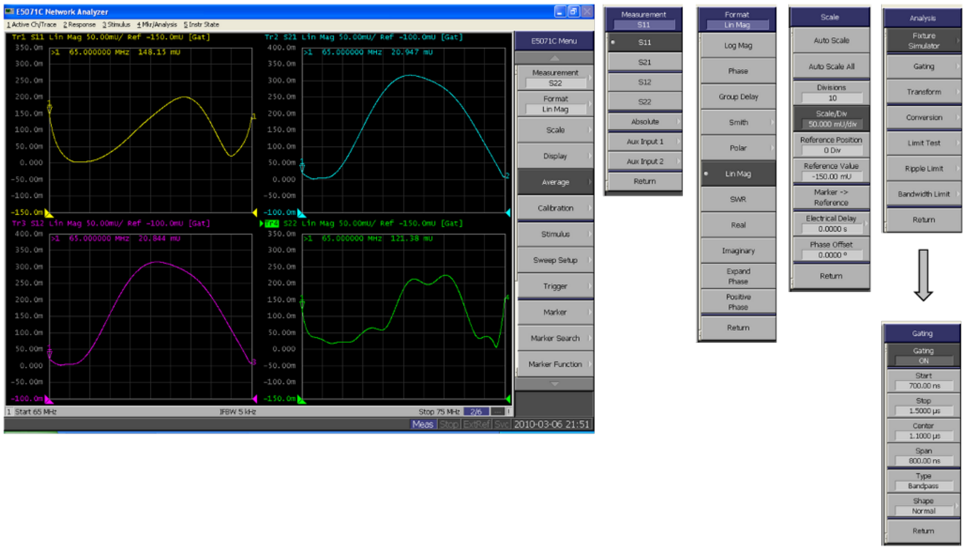

Tr1 S11 Lin Mag 50.00mU/ Ref -150.0mU [Gat]
>1 65.000000 MHz 148.15 mU

Tr2 S21 Lin Mag 50.00mU/ Ref -100.0mU [Gat]
>1 65.000000 MHz 20.947 mU

Tr3 S12 Lin Mag 50.00mU/ Ref -100.0mU [Gat]
>1 65.000000 MHz 20.844 mU

Tr4 S22 Lin Mag 50.00mU/ Ref -150.0mU [Gat]
>1 65.000000 MHz 121.38 mU

1 Start 65 MHz IFBW 5 kHz Stop 75 MHz 2/6

Meas Stop ExtRef Svc 2010-03-06 21:51

Measurement S22

Format Lin Mag

Measurement S11

Format Lin Mag

Divisions 10

Scale/Div 50.000 mU/div

Reference Position 0 Div

Reference Value -150.00 mU

Electrical Delay 0.0000 s

Phase Offset 0.0000 °

Gating ON

Start 700.00 ns

Stop 1.5000 µs

Center 1.1000 µs

Span 800.00 ns

Type Bandpass

Shape Normal

Main menu of the ENA 5071C network analyzer with the Measurement, Format, Scale, Analysis, and Gating menus expanded

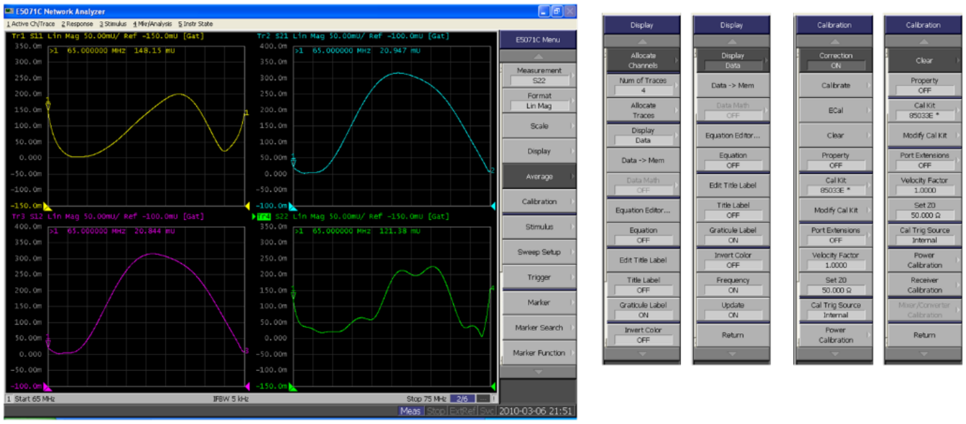

Main menu of the ENA 5071C network analyzer with the Display and Calibration menus expanded

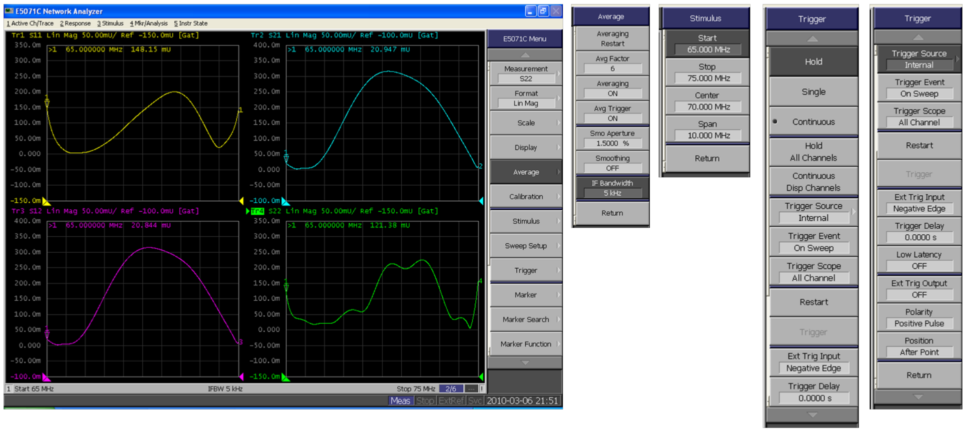

Main menu of the ENA 5071C network analyzer with Average, Stimulus and Trigger menus expanded

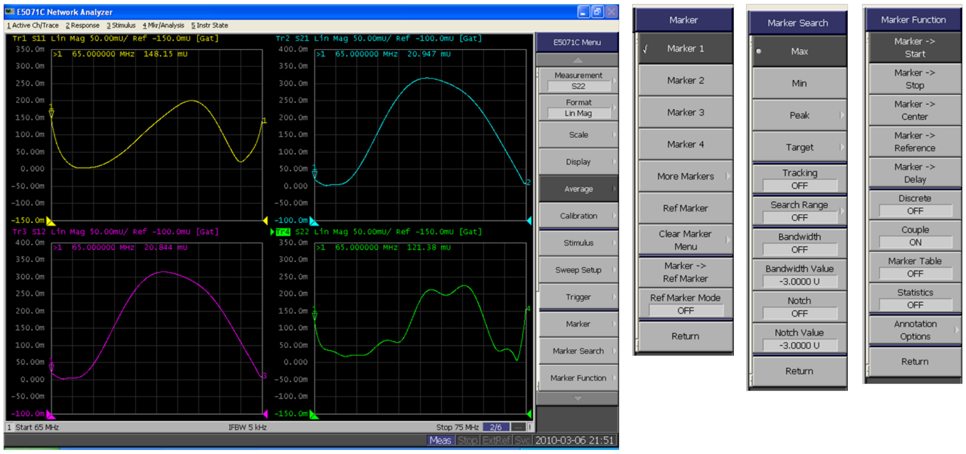

Main menu of the ENA 5071C network analyzer with the Marker, Marker Search and Marker Function menus expanded

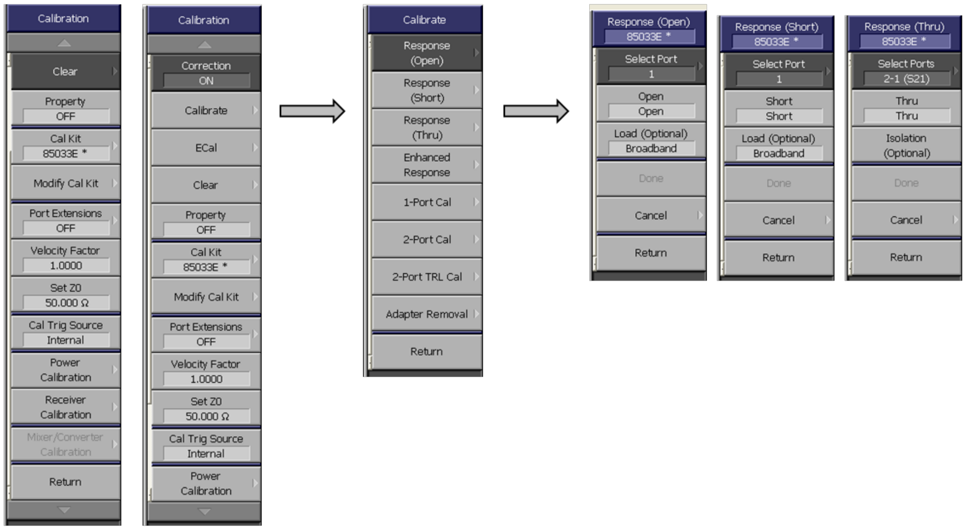

Calibration menu of the ENA 5071C network analyzer with the Calibrate menu expanded and showing Open, Short, and Thru Response menus